

INFORMATION TO USERS

This manuscript has been reproduced from the microfilm master. UMI films the text directly from the original or copy submitted. Thus, some thesis and dissertation copies are in typewriter face, while others may be from any type of computer printer.

The quality of this reproduction is dependent upon the quality of the copy submitted. Broken or indistinct print, colored or poor quality illustrations and photographs, print bleedthrough, substandard margins, and improper alignment can adversely affect reproduction.

In the unlikely event that the author did not send UMI a complete manuscript and there are missing pages, these will be noted. Also, if unauthorized copyright material had to be removed, a note will indicate the deletion.

Oversize materials (e.g., maps, drawings, charts) are reproduced by sectioning the original, beginning at the upper left-hand corner and continuing from left to right in equal sections with small overlaps.

Photographs included in the original manuscript have been reproduced xerographically in this copy. Higher quality 6" x 9" black and white photographic prints are available for any photographs or illustrations appearing in this copy for an additional charge. Contact UMI directly to order.

**ProQuest Information and Learning
300 North Zeeb Road, Ann Arbor, MI 48106-1346 USA
800-521-0600**

UMI[®]

University of Alberta

Modelling the Dynamics of Abyssal Equator-Crossing Currents

by

Paul F. Choboter



A thesis submitted to the Faculty of Graduate Studies and Research in partial fulfillment of the requirements for the degree of **Doctor of Philosophy**

in

Applied Mathematics

Department of Mathematical and Statistical Sciences

Edmonton, Alberta

Spring 2002



**National Library
of Canada**

**Acquisitions and
Bibliographic Services**

**395 Wellington Street
Ottawa ON K1A 0N4
Canada**

**Bibliothèque nationale
du Canada**

**Acquisitions et
services bibliographiques**

**395, rue Wellington
Ottawa ON K1A 0N4
Canada**

Your file Votre référence

Our file Notre référence

The author has granted a non-exclusive licence allowing the National Library of Canada to reproduce, loan, distribute or sell copies of this thesis in microform, paper or electronic formats.

L'auteur a accordé une licence non exclusive permettant à la Bibliothèque nationale du Canada de reproduire, prêter, distribuer ou vendre des copies de cette thèse sous la forme de microfiche/film, de reproduction sur papier ou sur format électronique.

The author retains ownership of the copyright in this thesis. Neither the thesis nor substantial extracts from it may be printed or otherwise reproduced without the author's permission.

L'auteur conserve la propriété du droit d'auteur qui protège cette thèse. Ni la thèse ni des extraits substantiels de celle-ci ne doivent être imprimés ou autrement reproduits sans son autorisation.

0-612-68544-6

Canada

University of Alberta

Library Release Form

Name of Author: Paul Franklin Choboter

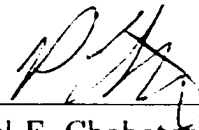
Title of Thesis: Modelling the Dynamics of Abyssal Equator-Crossing Currents

Degree: Doctor of Philosophy

Year this Degree Granted: 2002

Permission is hereby granted to the University of Alberta Library to reproduce single copies of this thesis and to lend or sell such copies for private, scholarly or scientific research purposes only.

The author reserves all other publication and other rights in association with the copyright in the thesis, and except as herein before provided, neither the thesis nor any substantial portion thereof may be printed or otherwise reproduced in any material form whatever without the author's prior written permission.



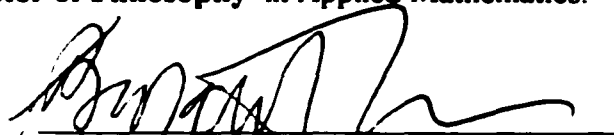
Paul F. Choboter
Dept. of Mathematical Sciences
University of Alberta
Edmonton, Alberta, Canada
T6G 2G1

Date: Jan 14/2002

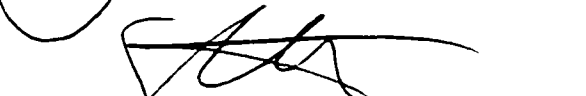
UNIVERSITY OF ALBERTA

Faculty of Graduate Studies and Research

The undersigned certify that they have read, and recommend to the Faculty of Graduate Studies and Research for acceptance, a thesis entitled **Modelling the Dynamics of Abyssal Equator-Crossing Currents** submitted by **Paul F. Choboter** in partial fulfillment of the requirements for the degree of **Doctor of Philosophy** in Applied Mathematics.



Dr. T. Bryant Moodie (Chair)



Dr. Gordon E. Swaters (Supervisor)



Dr. Bruce R. Sutherland



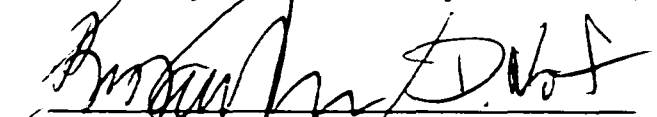
Dr. John C. Bowman



Dr. Andrew Bush (Earth & Atmospheric Sci)



Dr. Paul Myers (Earth & Atmospheric Sciences)



Dr. Doron Nof (Florida State University, Reader)

January 4, 2002

Abstract

The dynamical balance within abyssal equator-crossing flows is examined by studying simplified models of the flow in the equatorial region in the context of one- and two-layer shallow-water theory.

It is first demonstrated that, under reasonable assumptions, the shallow-water model is an appropriate model with which to study equatorial dynamics.

A simple model is then presented for one-layer cross-equatorial flow, where geostrophy is replaced at the equator by frictional flow down the pressure gradient. This model is compared via numerical simulations with the one-layer reduced gravity shallow-water model, first over idealized bottom topography, then over realistic equatorial Atlantic Ocean bottom topography. It is found that the frictional geostrophic model predicts certain aspects of the flow well, but neglects fluid inertia, which does affect the dynamics significantly.

Numerical simulations of the shallow-water equations over realistic Atlantic Ocean topography are described that show good agreement with the observed velocity fields of abyssal Antarctic Bottom Water as it crosses the equator. In particular, the observed southern-intensified flow within the equatorial channel at 36°W is reproduced. Additionally, our time-dependent simulations show that the large time variability observed in equatorial-crossing Antarctic Bottom Water can be reproduced by inducing relatively small temporal fluctuations in the current well before it reaches the equator.

The effects of baroclinicity are investigated by deriving a two-layer model of these

currents. We first calculate the theoretical speed of a steadily-travelling, dense eddy on a slope, taking into account the effects of upper-layer pressure variations and bottom friction, where the height field of the eddy is assumed to have compact support and the f -plane approximation is assumed to apply. We then derive a two-layer model of cross-equatorial flow. The model is uniformly valid in the sense that it reduces, at leading order, to the appropriate equatorial model when expressed in equatorial scales, and to the correct mid-latitude model when in mid-latitude scales. The lower layer resembles the shallow-water equations, and the upper layer is similar to the Charney balance equations. The form of the model implies the two layers are partially decoupled at the equator.

Acknowledgements

I would like to acknowledge funding received from the Natural Sciences and Engineering Research Council (NSERC) in the form of their PGS B scholarship, and from the Killam Foundation in the form of the Izaak Walton Killam Memorial Scholarship.

This research has been discussed with several notable scientists, who have provided helpful suggestions, including Gary Glatzmeier, Bill Smyth, Ted Shepherd, Tony Maxworthy, John Allen and Roger Samelson. My thanks go out to them. Thank-you to Mindy Hall, who not only kindly agreed to let me reproduce a figure from her paper, but volunteered to send me the figure in postscript format!

Thanks to my fellow graduate students with whom I have spent many enjoyable hours discussing various parts of this research, including Mateusz Reszka, Patrick Montgomery and Kathleen Dohan. Matt, in particular, has spent a great deal of time with me discussing research, and his ideas and insights were most helpful. Thanks.

Thank-you to the following proofreaders: Paul Shelley, who read the manuscript with amazing speed and attention to detail; Kathleen Dohan, who read the thesis with an eye for fundamental fluid dynamics issues; and Matt Reszka, who made very many helpful suggestions after reading the thesis. The thesis has been significantly improved as a result of their comments.

Some fellow students helped with my teaching duties while I presented this material in California, Italy and Oregon. They are Connell McClusky, Moses Waitaha, Kathleen Dohan, Mateusz Reszka, Mehdi Sangani-Manfared, and Morris Flynn. Many thanks!

Thanks to the members of my thesis committee who have provided helpful feedback on this research all the way along, in particular Bruce Sutherland and Andrew Bush.

Many thanks to Gordon Swaters, who has been an outstanding supervisor. His insight is amazing, and his enthusiasm is infectious. It has been an honour and a pleasure to learn the pursuit of science from Gordon.

Finally, thanks to my wife, Denise, for her encouragement, support, patience and love. Without her, this thesis would not have ever been written.

Contents

1	Introduction	1
2	Governing equations and preliminary results	13
2.1	Applicability of shallow-water theory	13
2.2	Shallow-water theory	19
2.2.1	Inviscid model	19
2.2.2	Frictional effects	22
2.3	Equatorial waves	25
2.3.1	Review of barotropic wave theory	25
2.3.2	Two-layer waves	28
3	One-layer model	36
3.1	Frictional geostrophic model	37
3.2	Numerical methods	42
3.3	Parameter values and observations	46
3.4	Flow over idealized topography	49
3.5	Flow over realistic topography	58
3.5.1	Numerical scheme	61
3.5.2	Steady-state results	62
3.5.3	Time-dependent flow	68
4	Two-layer model	78
4.1	Modified Nof analysis	79
4.2	Generic nondimensionalization	83
4.3	Mid-latitude model: Equatorial Swaters-Flierl	85
4.3.1	Derivation of the vorticity equation	88
4.3.2	Divergence equation derivation	90
4.3.3	Mid-latitude model	91
4.3.4	ESF model simulations	94
4.4	Equatorial model	102
4.4.1	Equatorial model derivation	103
4.4.2	Boundary-forced $\psi = O(1)$ model	104
4.4.3	Lower-layer-forced $\psi = O(s)$ model	106

4.4.4	Waves in the lower-layer-forced model	108
4.5	Uniformly valid model	110
4.5.1	Model summary	111
4.5.2	Adjustment of dependent variables	113
4.5.3	Adjustment of length, velocity and time scales	116
4.6	Summary	119
5	Conclusions	121
5.1	Summary	121
5.2	Future directions	126
	References	127

List of Tables

3.1	Lines across which the flux is calculated in the simulations.	64
4.1	Length, velocity and time scales.	117

List of Figures

2.1	The dispersion diagram for equatorial waves.	29
3.1	The Arakawa C-grid.	44
3.2	Coriolis parameter variation with latitude.	50
3.3	The results of a shallow-water simulation, $Ro = 0.02$	52
3.4	The results of an FG model simulation, $r = 0.02$	53
3.5	Centre of mass motion.	54
3.6	Motion after splitting.	56
3.7	Amount of fluid in each hemisphere after splitting.	57
3.8	Bottom topography of the equatorial Atlantic.	59
3.9	Bottom topography before and after smoothing.	60
3.10	Height field at steady state, shallow-water model.	62
3.11	Height field at steady state, FG model.	63
3.12	Flux across equator as a function of inflow position.	65
3.13	Velocity fields in the equatorial basin for realistic and very shallow inflow.	67
3.14	Percentage flux across equator as a function of damping parameter.	68
3.15	Time-dependent flux as measured by HMW.	69
3.16	Time-dependent flux as predicted by shallow-water theory.	71
3.17	Time-dependent flux as predicted by FG model.	73
3.18	Time-dependent flux as predicted by shallow-water theory, inflow position of $x_c = 1.15$	74
3.19	Amplitude of time-dependent fluxes versus amplitude of time-dependent inflow condition, shallow-water simulations.	75
4.1	The geometry of the problem.	85
4.2	Two-layer model simulation with $f = 1$, $h_B = y$	96
4.3	Two-layer FG model simulation over idealized channel.	97
4.4	Two-layer model simulation over idealized channel, lower layer is shallow-water.	98
4.5	Two-layer model simulation, eastward eddy.	99
4.6	Two-layer model simulation over idealized channel, lower layer is shallow-water, periodic conditions.	100

4.7	Two-layer model simulation over idealized channel, lower layer is shallow-water, inflow current.	101
-----	--	-----

Chapter 1

Introduction

The earth's oceans and atmosphere form a complex coupled fluid system. While atmospheric dynamics alone, to a first approximation, govern the daily weather we experience, oceanic dynamics cannot be neglected in studying the long-term behaviour of the climate. The oceans are known to transport a significant amount of heat from the equatorial regions to the polar regions (Trenberth and Caron 2001). It is therefore important to develop an understanding of the ocean currents that transport this heat around the planet.

The thermohaline circulation is the global-scale ocean circulation driven by density differences arising from temperature and salinity variations. In the Atlantic, the deepest part of the thermohaline circulation consists of Antarctic Bottom Water (AABW), which originates in the Weddell Sea near Antarctica. In this location, particularly cold and fresh water sinks to the bottom of the ocean and flows northward

along the sloping ocean floor in the western Atlantic Ocean. While part of this flow remains in the Southern Hemisphere and ultimately mixes upward into shallower waters (Ledwell *et al.* 2000), part of the flow has been observed to cross the equator into the Northern Hemisphere (see DeMadron and Weatherly 1994; Friedrichs and Hall 1993). This current, therefore, acts as a conduit for heat, salt and nutrients to be transported global-scale distances.

Unlike atmospheric flows, oceanic currents that exist at depth are difficult to observe, and indeed, observations are notably sparse. For example, the path of AABW in the southern Atlantic Ocean is disputed in the literature, since more than one path is consistent with existing observations (DeMadron and Weatherly 1994; Speer and Zenk 1993; Sandoval and Weatherly 2001). A study of ocean dynamics is thus essential not only to understand why and how some currents flow, but in certain cases, to help determine where the currents flow.

Like many mesoscale and large-scale flows in the atmosphere and ocean, these abyssal flows are observed to be geostrophically balanced at mid-latitudes and polar regions. That is, the pressure gradient forces approximately balance the Coriolis effect, giving rise to a more or less steady flow. Indeed, many models of motion on these scales are derived by assuming the leading order velocity fields are geostrophic (e.g. Karsten and Swaters 1999). However, geostrophy must necessarily break down in the vicinity of the equator, since the Coriolis parameter $f = 2\Omega \sin \theta$, where $\Omega = 2\pi$ radians/day is the Earth's angular velocity and θ is the latitude, vanishes at the

equator, and therefore so does the Coriolis effect. The question, therefore, is as follows: If these flows are geostrophically balanced away from the equator, what balance, if any, exists at the equator? An equally important question to resolve is how the geostrophic balance is re-established after a current traverses the equator. This thesis, in part, addresses these questions, with an emphasis on the former.

Potential vorticity, defined as $q = (f + \zeta)/h$ in the shallow-water approximation, where $\zeta = \hat{e}_3 \cdot \nabla \times \mathbf{u}$ is the vertical (or radially outward, if considering motion on the surface of a sphere) component of the relative vorticity and h is the thickness of the fluid layer, is exactly conserved following the flow if frictional and diabatic effects are neglected. However, away from the equator in either hemisphere, the flow is often observed to be relatively quiescent so that $|f| \gg |\zeta|$ and thus $q \approx f/h$. Therefore, since the Coriolis parameter changes sign over the path of the fluid, these equator-crossing abyssal flows cannot conserve potential vorticity. This violation of potential vorticity conservation in cross-equatorial flows and the breakdown of geostrophy at the equator constitute two significant challenges in modelling these flows.

Previous research has focused on two processes to explain potential vorticity modification: nonlinearity and friction. Potential vorticity modification in equator-crossing currents where the nonlinear terms were not negligible was addressed by Edwards and Pedlosky (1998a, 1998b). They modelled the equatorial ocean using a nonlinear one-layer shallow-water model with $f = \beta y$, assuming a flat bottom topography, and horizontal friction. They forced fluid across the equator in numerical

simulations by specifying a localized mass source in the Northern Hemisphere and a distributed mass sink in the Southern Hemisphere. Eddies developed in the current as it approached the equator, particularly for the more strongly forced runs. An analysis of the vorticity flux showed that, in general, the eddy field transports vorticity to the western boundary, where friction dissipates the vorticity. They concluded that for cross-equatorial flow to occur, the eddy field must work in conjunction with the dissipative side-layer to modify the vorticity.

In a companion paper, Edwards and Pedlosky (1998b) described a linear stability analysis of a steady meridional current, using the f -plane approximation. The dependence of the instabilities on the Coriolis parameter f , and thereby the dependence on latitude, was investigated. The instability was found to be greater at lower latitudes and at higher current velocities, which was consistent with what they observed in their numerical simulations. They argued that the instability is essentially an inviscid shear instability, so that, although friction is necessary for potential vorticity modification, it does not play a role in the production of the eddies that transport the potential vorticity to the side boundary.

Kawase, Rothstein, and Springer (1992) numerically integrated the three dimensional equations of motion (specifically, the Boussinesq, hydrostatic, incompressible fluid equations in spherical coordinates) over a domain centred on the equator. Although they included complicated dynamics, they neglected bottom topography and the geometry of the side boundaries. Their numerical investigation focussed on a

southern flowing deep western boundary current as it approached the equator. During the initial spin-up stages, the current turned eastward along the equator, but in the steady-state ocean, the current crossed the equator along the western boundary.

Note that Edwards and Pedlosky (1998a, 1998b) and Kawase *et al.* (1992) all neglected variable bottom topography. Their studies therefore apply to deep currents, but not necessarily the abyssal flows that are strongly affected by topography. The role of variable topography is an important aspect of the dynamics not previously examined and an issue we address in this thesis.

Antarctic Bottom Water is an abyssal current that is strongly affected by topography. It flows northward along the floor of the Atlantic Ocean, within a basin that lies between North and South America and the mid-Atlantic ridge. It is observed to flow northward along the western flank of the ocean basin (i.e. closest to South America) as it approaches the equator, but flows along the eastern flank of the ocean basin (i.e. next to the mid-Atlantic ridge) after crossing the equator. Nof and Olson (1993) proposed that simple geostrophy requires that the current can cross the equator only if it switches sides of the basin as it crosses. To support this, they studied the phenomenon using two steady, inviscid, reduced-gravity models: a $1\frac{1}{2}$ layer model¹ in a parabolic meridional channel, and a $2\frac{1}{2}$ layer model with flat topography, where the current has constant potential vorticity. Their analytic solutions showed that the equator was successfully crossed and that the bottom current did switch sides of the

¹An $n + \frac{1}{2}$ layer model is a model with n dynamically active layers coupled to a relatively thick inactive layer.

channel. Johnson (1993) has also studied a steady, inviscid, reduced-gravity model with a constant potential vorticity flow, but with a linear bottom topography, and found that changes in the width and height of the current allowed it to cross the equator.

Borisov and Nof (1998) suggested that deep currents may cross the equator in the form of eddies and so studied the dynamics of eddies approaching the equator in a parabolic meridional channel. They first studied the dynamics of solid, frictionless, noninteracting particles in the channel and obtained statistics about how likely a given particle is to cross the equator given its initial position and velocity. They then employed a one-layer reduced-gravity shallow-water model and performed numerical experiments on eddies approaching the equator. How much of the eddy crossed the equator was found to depend on the geometry of the channel and the initial speed and direction of the eddy. The presence of friction altered the potential vorticity of the eddy to allow some of the fluid to cross the equator, but how much of the fluid crossed was found to be dependent more on the geometry than on the magnitude of the friction present.

Nof and Borisov (1998) performed numerical simulations of abyssal currents approaching the equator on a meridional channel, with bottom topography varying parabolically in the zonal direction, using a reduced-gravity shallow-water model. They found that the shallow-water simulations compared more favourably with the dynamics of the solid particles as studied by Borisov and Nof (1998) than with the

analytic solution of Nof and Olson (1993). Nof and Borisov (1998) therefore concluded that the equator-crossing process is an inertial one in which the geometry of the bottom topography plays a crucial role. (Note that similar conclusions were made by Rodwell and Hoskins (2001) about the atmospheric equator-crossing flow associated with the summer monsoon.) The differences between the analytic solutions, in which potential vorticity is conserved, and the shallow-water simulations led them to conclude that the potential vorticity is modified by friction as the current proceeds, allowing the flow to proceed along the path prescribed by the bottom topography.

The movement of abyssal waters in the equatorial ocean has also been studied by Stephens and Marshall (2000), who performed numerical simulations of a simplified model over realistic oceanic bathymetry. In this model, the full shallow-water conservation of mass equation is retained (with a small sink term representing the effects of upwelling), but the momentum equations are replaced by a planetary geostrophic formulation with the addition of friction in the form of Rayleigh damping terms linear in velocity. The steady-state flow was found to be broadly consistent with observations.

Thus, in summary, recent research into these flows has focussed either on studying the full dynamics of the flow over idealized topography or on examining the steady-state flow over realistic equatorial topography as predicted by a simplified model. An omission in the literature is the performance of numerical simulations of one-layer reduced-gravity shallow-water equations over realistic topography. We have performed simulations of this nature and we discuss them in this thesis. These

simulations are compared to the simulations of a simplified model in order to assess what aspects of these flows are successfully described by the simple model and to what degree nonlinearity and time dependence are important in these flows.

The dynamics of cross-equatorial flows have been shown to involve frictional effects, the effects of bottom topography, and inertial effects. One aspect of the dynamics that has received little attention is how these currents dynamically couple with the overlying fluid. This may be addressed by studying a two-layer model of the flow. If we are to study a two-layer equatorial model, it is desirable for that model to reduce to the appropriate geostrophically balanced model in the mid-latitude limit. Karsten and Swaters (1999) derived and classified all the possible frontal geostrophic models derivable from two-layer shallow-water theory, and found that the appropriate one for the case in which the lower layer is shallow and the bottom topography plays an important dynamical role is the model derived by Swaters and Flierl (1991).

The Swaters and Flierl (1991) model captures the baroclinic, subinertial dynamics of a thin lower layer flowing over bottom topography coupled to a thick upper layer. The model is derived from two-layer shallow-water theory by an asymptotic expansion in terms of a parameter that plays the role of the Rossby number of the flow (Swaters 1991; Swaters and Flierl 1991). The resulting dynamics may be thought of as being modelled by planetary geostrophy in the lower layer and quasi-geostrophy in the upper layer, with a coupling between the pressure fields of the two layers. Planetary geostrophy is a model of the flow where the evolution of the thickness of the layer is

governed by the conservation of mass, with the velocity assumed to be given by the geostrophic relations, whereas in quasi-geostrophic flow, the evolution equation is the vorticity equation, with the velocity again assumed to be geostrophic.

However the model of Swaters and Flierl (1991) cannot be used near the equator because it was derived under the f -plane approximation. That is, dynamics arising from the meridional variation of the Coriolis parameter are neglected. This is a reasonable approximation at mid-latitudes and on small enough length scales, but not if the domain includes the equator. One of the goals of this work is to investigate to what extent the Swaters and Flierl (1991) model may be extended to the equator. In other words, can a model be developed that captures the dynamics of these equator-crossing currents and that simplifies, in the mid-latitude limit, to the Swaters and Flierl (1991) model?

We will show that such a model can, in fact, be derived, provided that the geostrophic balance relation is generalized to a relation describing well-defined velocities in the $f \rightarrow 0$ limit. We will employ two such generalizations, each valid only for its respective layer. While neither relation is individually new, they have not, to our knowledge, previously been written down *together* to form a coupled two-layer model applicable at the equator.

The shallow-water equations are used as the starting point for our theory in this thesis, and so in Chapter 2 we present general results about the application of shallow-water theory to the equatorial region. We first address the applicability

of the shallow-water equations as a model of equatorial dynamics by expanding the three-dimensional Navier-Stokes equations in an asymptotic expansion, where the small parameters are the ratio of the horizontal length scale of the motion to the Earth's radius and the ratio of the vertical to horizontal length scales. It is shown that the horizontal component of the Coriolis effect and Earth curvature effects may be neglected as long as the horizontal length scale of motion is of sufficiently large magnitude.

In Chapter 2, we also present the shallow-water equations of motion, and state some of their conservation properties. Equatorial wave theory is reviewed, and it is shown that in a two-layer system where the layers have unequal depths, the waves contained in the model can be related to the waves contained in the one-layer model, with appropriate scaling factors. These waves are relevant in the context of the model we derive in Chapter 4.

In Chapter 3, a simple model is presented for one-layer cross-equatorial flow, where geostrophy is replaced at the equator by frictional flow down the pressure gradient. This model is compared via numerical simulations to the one-layer reduced-gravity shallow-water model, first over idealized bottom topography, then over realistic equatorial Atlantic Ocean bottom topography. We find from the idealized topography simulations that the simplified model predicts qualitatively correct fluid paths and reproduces well the theoretical along-slope speed of a dense, compactly-supported eddy on a slope. However, the simplified model is unreliable with respect to certain

aspects of the flow where the momentum of the fluid plays a role, since fluid inertia is neglected in the model.

Our simulations over realistic topography are intended to simulate Antarctic Bottom Water flow northward in the southern Atlantic Ocean, so we introduce a mass source of dense fluid at the southern edge of our numerical domain, and observe it as it flows northward. We perform two experiments: steady inflow conditions with an analysis of the steady-state conditions, and time-varying inflow conditions to simulate the annual signal seen in observational studies. Our comparison of the simplified model to the shallow-water model confirms the results of our idealized topography simulations. Additionally, our comparison of the shallow-water model results to observations shows qualitative agreement with the observed velocity field. Our time-dependent simulations show that the relatively large time variability observed in the cross-equatorial current can be reproduced, and furthermore, is reproduced by a relatively small amplitude in time-variability of the Antarctic Bottom Water current as it approaches the equator. We believe the good agreement between observations and the predictions of one-layer reduced-gravity shallow-water equations is strong evidence that certain aspects of these flows can be well understood from the standpoint of inertial, reduced-gravity dynamics.

In Chapter 4, we investigate the degree to which baroclinicity may also be important in the dynamics of these currents by deriving a two-layer model of equatorial flow. We first motivate the need for an upper layer by deriving the theoretical speed

of a dense, compactly-supported eddy on a slope on an f -plane, where the effects of pressure variations in the upper layer and the (parameterized) effects of friction are taken into account. We then derive a two-layer model of cross-equatorial flow where the lower layer may be taken to be either of the one-layer models studied in Chapter 3, and the upper layer uses a generalization to geostrophy that is similar to the Charney balance equations (Gent and McWilliams 1983). In the limit of motion far from the equator, this two-layer model reduces to the Swaters and Flierl (1991) model, which is the appropriate geostrophically balanced model describing the motion of a relatively thin lower layer interacting with topography.

To focus on the two-layer dynamics in the limit of motion right on the equator, we describe in Chapter 4 the equations of motion re-scaled using a standard equatorial \mathcal{J} -plane scaling, and a two-layer model is derived in the context of that scaling. By comparing this model, which is valid for equatorial scales, to the previously derived model, which is valid for mid-latitude scales, a leading-order uniformly valid “meta-model” is derived. This meta-model reduces, when expressed in mid-latitude scales or equatorial scales, to the mid-latitude or equatorial model, respectively.

The conclusions of our research and related future research projects to be pursued are discussed in Chapter 5.

Chapter 2

Governing equations and preliminary results

2.1 Applicability of shallow-water theory

To begin with, we address the question of the applicability of shallow-water theory to the equatorial region. We do so by following Karsten and Swaters (1999), who perform an asymptotic expansion of the fully three-dimensional Navier-Stokes equations in spherical coordinates to determine the relative importance of the various terms in the equations of motion. Our analysis differs from theirs in that, while they assume *a priori* that the flow is geostrophically balanced, we do not.

We shall assume frictionless flow and a single layer of homogeneous density for this analysis. We fully anticipate including friction in our model, but this analysis

is intended only to evaluate the validity of neglecting terms such as nonhydrostatic terms, the horizontal component of the Coriolis effect, and Earth curvature terms, so we neglect friction for now.

The governing equations for a single homogeneous layer of fluid flowing over the surface of the Earth may be expressed in spherical coordinates as follows (Cushman-Roisin 1994; Karsten and Swaters 1999):

$$\begin{aligned}
\frac{du^*}{dt^*} + \frac{u^*w^*}{r^*} - \tan\theta \frac{u^*v^*}{r^*} - 2\Omega \sin\theta v^* + 2\Omega \cos\theta w^* &= -\frac{1}{\rho r^* \cos\theta} \frac{\partial p^*}{\partial \phi}, \\
\frac{dv^*}{dt^*} + \frac{v^*w^*}{r^*} + \tan\theta \frac{u^{*2}}{r^*} + 2\Omega \sin\theta u^* &= -\frac{1}{\rho r^*} \frac{\partial p^*}{\partial \theta}, \\
\frac{dw^*}{dt^*} - \frac{u^{*2} + v^{*2}}{r^*} - 2\Omega \cos\theta u^* &= -\frac{1}{\rho} \frac{\partial p^*}{\partial r^*} - g, \\
\frac{\partial w^*}{\partial r^*} + 2\frac{w^*}{r^*} + \frac{1}{r^* \cos\theta} \frac{\partial}{\partial \theta}(v^* \cos\theta) + \frac{1}{r^* \cos\theta} \frac{\partial u^*}{\partial \phi} &= 0.
\end{aligned} \tag{2.1}$$

where

$$\frac{d}{dt^*} \equiv \frac{\partial}{\partial t^*} + \frac{u^*}{r^* \cos\theta} \frac{\partial}{\partial \phi} + \frac{v^*}{r^*} \frac{\partial}{\partial \theta} + w^* \frac{\partial}{\partial r^*}$$

is the material derivative, r^* is the radial distance from the Earth's centre, θ is the latitude, ϕ is the longitude, t^* is time, p^* is the pressure, and u^* , v^* , and w^* are the velocities in the eastward, northward and radial directions, respectively. An asterisk denotes a dimensional variable. The dimensional parameters Ω , g , and ρ are the angular velocity of the Earth, the gravitational acceleration, and the constant density, respectively.

One may convert these equations from spherical coordinates (r^*, ϕ, θ) to a local cartesian coordinate system (x^*, y^*, z^*) by expanding about a central latitude $\theta = \theta_0$

and the planetary radius $r^* = r_0$. Then, by writing the pressure as the sum of its hydrostatic and dynamic parts,

$$p^* = -\rho g z^* + \rho \tilde{p}^*(x^*, y^*, z^*), \quad (2.2)$$

and introducing the generic nondimensionalizations

$$(x^*, y^*) = L(x, y), \quad z^* = Hz, \quad (u^*, v^*) = U(u, v),$$

$$w^* = Ww, \quad t^* = Tt, \quad \tilde{p}^* = P\tilde{p},$$

the equations of motion may be written as follows:

$$\begin{aligned} \frac{du}{dt} + \lambda \alpha \xi u w - \xi \tan \theta_0 u v - \left(\frac{1}{\epsilon} + \frac{\epsilon_\beta}{\epsilon} y \right) v + \lambda \alpha \left(\frac{\cot \theta_0}{\epsilon} - \frac{\xi}{\epsilon} y \right) w \\ = -(1 + \gamma y - \lambda \xi z) \frac{1}{F^2} \frac{\partial \tilde{p}}{\partial x} + O(\xi^2), \\ \frac{dv}{dt} + \lambda \alpha \xi v w + \xi \tan \theta_0 u^2 + \left(\frac{1}{\epsilon} + \frac{\epsilon_\beta}{\epsilon} y \right) u = -(1 - \lambda \xi z) \frac{1}{F^2} \frac{\partial \tilde{p}}{\partial y} + O(\xi^2), \\ \alpha \lambda^2 \frac{dw}{dt} - \lambda \xi (u^2 + v^2) - \lambda \alpha \left(\frac{\cot \theta_0}{\epsilon} - \frac{\xi}{\epsilon} y \right) u = -\frac{1}{F^2} \frac{\partial \tilde{p}}{\partial z} + O(\xi^2), \\ \alpha \frac{\partial w}{\partial z} + 2\lambda \alpha \xi w + (1 - \lambda \xi z) \left(\frac{\partial v}{\partial y} - \gamma v \right) + (1 - \lambda \xi z)(1 + \gamma y) \frac{\partial u}{\partial x} + O(\xi^2) = 0, \\ \text{where } \frac{d}{dt} \equiv \frac{\epsilon_T}{\epsilon} \frac{\partial}{\partial t} + (1 - \lambda \xi z) \left[(1 + \gamma y) u \frac{\partial}{\partial x} + v \frac{\partial}{\partial y} \right] + \alpha w \frac{\partial}{\partial z}. \end{aligned} \quad (2.3)$$

In writing the above equations, we have introduced the variable $\xi \equiv L/r_0 \ll 1$ and the following nondimensional parameters:

$$\begin{aligned} \lambda = \frac{H}{L}, \quad F = \frac{U}{\sqrt{P}}, \quad \gamma = \xi \tan \theta_0, \quad \alpha = \frac{WL}{UH}, \\ \epsilon = \frac{U}{f_0 L}, \quad \epsilon_T = \frac{1}{f_0 T}, \quad \epsilon_\beta = \xi \cot \theta_0. \end{aligned}$$

As described in Karsten and Swaters (1999), the parameters λ , F , γ , α , ϵ , ϵ_T and ϵ_β are, respectively, the aspect ratio of the motion, the Froude number, a metric term (measuring Earth curvature effects), a measure of the relative importance of the vertical gradient of the vertical velocity to the horizontal divergence of the horizontal velocity, the Rossby number, the temporal Rossby number, and the planetary Rossby number (ratio of the planetary vorticity gradient to the planetary vorticity itself).

We may check the applicability of the shallow-water model at the equator by taking the limit as $\theta_0 \rightarrow 0$ in the governing equations. Since $|\epsilon| \rightarrow \infty$ in that limit, we first rewrite the terms proportional to $\cot \theta_0 / \epsilon$ for a clearer interpretation. With the standard definitions of the two forms of the beta parameter (see Pedlosky 1987, §6.2)

$$\mathcal{J}_0 \equiv \frac{2\Omega}{r_0} \cos \theta_0,$$

and

$$\mathcal{J} \equiv \frac{\mathcal{J}_0 L^2}{U} = \xi \frac{2\Omega L \cos \theta_0}{U},$$

we find

$$\frac{\cot \theta_0}{\epsilon} = \frac{\mathcal{J}}{\xi}, \quad \text{and} \quad \frac{\epsilon_\beta}{\epsilon} = \mathcal{J}.$$

Substituting these into the equations of motion and taking the limit as $\theta_0 \rightarrow 0$. (so that $|\epsilon| \rightarrow \infty$ and $\gamma \rightarrow 0$ as well) we find the leading order governing equatorial equations take the form

$$\begin{aligned}
\frac{du}{dt} + \lambda\alpha\xi uw - \beta yv + \beta\alpha\frac{\lambda}{\xi}w &= -\frac{1 - \lambda\xi z}{F^2}\frac{\partial\bar{p}}{\partial x} + O(\xi^2, \xi\lambda), \\
\frac{dv}{dt} + \lambda\alpha\xi vw + \beta yu &= -\frac{1 - \lambda\xi z}{F^2}\frac{\partial\bar{p}}{\partial y} + O(\xi^2), \\
\alpha\lambda^2\frac{dw}{dt} - \lambda\xi(u^2 + v^2) - \beta\frac{\lambda}{\xi}u &= -\frac{1}{F^2}\frac{\partial\bar{p}}{\partial z} + O(\xi^2, \xi\lambda), \\
\alpha\frac{\partial w}{\partial z} + 2\lambda\alpha\xi w + (1 - \lambda\xi z)\left(\frac{\partial u}{\partial x} + \frac{\partial v}{\partial y}\right) + O(\xi^2) &= 0, \\
\frac{d}{dt} \equiv \frac{\epsilon_T}{\epsilon}\frac{\partial}{\partial t} + (1 - \lambda\xi z)\left[u\frac{\partial}{\partial x} + v\frac{\partial}{\partial y}\right] + \alpha w\frac{\partial}{\partial z}.
\end{aligned} \tag{2.4}$$

We are discussing flows for which $\xi = L/r_0 \ll 1$, i.e. the length scale of motion is much smaller than the radius of the Earth. Let us also assume the aspect ratio $\lambda = H/L$ is a small parameter, which is true for most geophysical flows. Then, by the conservation of mass equation, we have that $\alpha \leq O(1)$. Thus, the governing equations reduce to

$$\begin{aligned}
\frac{du}{dt} - \beta yv + \beta\alpha\frac{\lambda}{\xi}w &= -\frac{1}{F^2}\frac{\partial\bar{p}}{\partial x} + O(\xi^2, \xi\lambda), \\
\frac{dv}{dt} + \beta yu &= -\frac{1}{F^2}\frac{\partial\bar{p}}{\partial y} + O(\xi^2, \xi\lambda), \\
-\beta\frac{\lambda}{\xi}u &= -\frac{1}{F^2}\frac{\partial\bar{p}}{\partial z} + O(\xi^2, \xi\lambda), \\
\alpha\frac{\partial w}{\partial z} + \frac{\partial u}{\partial x} + \frac{\partial v}{\partial y} + O(\xi^2, \xi\lambda) &= 0, \\
\frac{d}{dt} \equiv \frac{\epsilon_T}{\epsilon}\frac{\partial}{\partial t} + u\frac{\partial}{\partial x} + v\frac{\partial}{\partial y} + \alpha w\frac{\partial}{\partial z}.
\end{aligned} \tag{2.5}$$

When do these equations reduce to the shallow-water equations? In the shallow-water model, the dependent variables do not vary with height z . If it were true that $\lambda/\xi \ll 1$, then $\partial\bar{p}/\partial z$ would be zero to leading order. Since \bar{p} would be independent of z , the velocity components would remain independent of z if initially so. Thus,

if $\lambda/\xi \ll 1$, then the above equations reduce to the (equatorial beta plane) shallow-water equations.

What is the significance of $\lambda/\xi \ll 1$? The terms containing λ/ξ represent the horizontal component of the Coriolis force and contribute to the breakdown of the nonhydrostatic assumption. In terms of more basic scaling factors,

$$\frac{\lambda}{\xi} = \frac{H/L}{L/r_0} = \frac{Hr_0}{L^2},$$

so that our first result is as follows:

Theorem 1 *For constant-density flow near the equator with horizontal scales much smaller than the radius of the Earth and aspect ratio much less than unity, shallow-water theory will be applicable as long as*

$$\frac{Hr_0}{L^2} \ll 1.$$

The larger the horizontal length scale, the better this requirement will be satisfied. For $H = 5$ km, we require $L \gg 180$ km. The current itself is of considerably smaller vertical extent, on the order of $H = 0.5$ km (Hall, McCartney, and Whitehead 1997), which means that the requirement is instead $L \gg 60$ km. Observations of Antarctic Bottom Water as it approaches the equator suggest that the current has a width of approximately $L = 200$ km (Sandoval and Weatherly 2001).

We note that the above result is not completely new, since de Verdière and Schopp (1994) showed that if $L < (Hr_0)^{1/2}$, then equatorial dynamics must include the horizontal component of the Coriolis effect. However, the above analysis does establish

that, under the mentioned assumptions, this effect is the *only* effect that one needs to add when considering equatorial dynamics. e.g. Earth curvature effects need not be considered.

2.2 Shallow-water theory

The equations of motion may be cast into various forms, some of which have advantages over others when attempting to integrate the equations numerically. We state some of the more useful forms here, and state the conserved quantities. The notation here closely follows that of Arakawa and Lamb (1981) and Arakawa and Hsu (1990).

2.2.1 Inviscid model

The inviscid shallow-water equations can be written in the form

$$\frac{\partial \mathbf{v}}{\partial t} + \mathbf{v} \cdot \nabla \mathbf{v} + f \mathbf{k} \times \mathbf{v} = -g \nabla (h + h_B). \quad (2.6)$$

$$\frac{\partial h}{\partial t} + \nabla \cdot (h \mathbf{v}) = 0. \quad (2.7)$$

where \mathbf{v} is the horizontal velocity, \mathbf{k} is the vertical unit vector, f is the Coriolis parameter, h is the thickness of the fluid, and h_B is the height of the bottom topography (assumed independent of time) above an arbitrary reference level. The first equation expresses conservation of momentum, and the second expresses conservation of mass.

These equations may be rewritten in the equivalent form

$$\frac{\partial \mathbf{v}}{\partial t} + q \mathbf{k} \times (h \mathbf{v}) + \nabla (K + \Phi) = \mathbf{0}. \quad (2.8)$$

$$\frac{\partial h}{\partial t} + \nabla \cdot (h\mathbf{v}) = 0, \quad (2.9)$$

where $q = (\zeta + f)/h$ is the potential vorticity, $\zeta = \mathbf{k} \cdot \nabla \times \mathbf{v}$ is the relative vorticity, $K = \mathbf{v} \cdot \mathbf{v}/2$, and $\Phi = g(h + h_B)$. K and Φ are related to the kinetic and potential energy of the fluid, respectively. More specific comments on the physical interpretation of K and Φ will be made below.

Taking the inner product of $h\mathbf{v}$ and (2.8) and using (2.9) gives

$$\frac{\partial}{\partial t} (hK) + \nabla \cdot (h\mathbf{v}K) + h\mathbf{v} \cdot \nabla \Phi = 0,$$

while multiplying (2.9) by Φ produces

$$\frac{\partial}{\partial t} \left(\frac{1}{2}gh^2 + gh h_B \right) + \nabla \cdot (h\mathbf{v}\Phi) - h\mathbf{v} \cdot \nabla \Phi = 0.$$

Adding the previous two equations yields the statement of conservation of total energy of the system

$$\frac{\partial}{\partial t} \left(hK + \frac{1}{2}gh^2 + gh h_B \right) + \nabla \cdot [h\mathbf{v}(K + \Phi)] = 0. \quad (2.10)$$

where we may now interpret hK as the (local) kinetic energy of the fluid, $\frac{1}{2}gh^2 + gh h_B$ as the potential energy, $h\mathbf{v}K$ as the kinetic energy flux, and $h\mathbf{v}\Phi$ as the potential energy flux. Note that, while the kinetic energy flux is velocity multiplied by kinetic energy, the potential energy flux is not simply the product of velocity and potential energy.

The potential vorticity equation is derived by first taking the vertical component of the curl of (2.8) to form the (absolute) vorticity equation.

$$\frac{\partial \zeta_A}{\partial t} + \nabla \cdot (\zeta_A \mathbf{v}) = 0. \quad (2.11)$$

where $\zeta_A = \zeta + f$ is the absolute vorticity. Then, by using the conservation of mass (2.9) to eliminate $\nabla \cdot \mathbf{v}$ from the vorticity equation, the potential vorticity equation may be written as follows:

$$\frac{\partial q}{\partial t} + \mathbf{v} \cdot \nabla q = 0. \quad (2.12)$$

Potential vorticity is thus conserved following the motion, that is, it is advected in space like a material tracer. The total absolute vorticity in the domain is conserved, but it may accumulate or disperse locally, much like the surface height of the fluid.

Equations (2.7) and (2.12) may be used to confirm the following conservation law: For an arbitrary differentiable function $F(x)$,

$$\frac{\partial}{\partial t} (hF(q)) + \nabla \cdot (h\mathbf{v}F(q)) = 0, \quad (2.13)$$

thus, $hF(q)$ is a conserved quantity (Yavneh and McWilliams 1994; Ren and Shepherd 1997). Note that the height (mass) of the fluid and the absolute vorticity are governed by identical equations of motion. Therefore, it is also true that

$$\frac{\partial}{\partial t} (\zeta_A F(q)) + \nabla \cdot (\zeta_A \mathbf{v} F(q)) = 0, \quad (2.14)$$

where $F(x)$ again represents an arbitrary differentiable function. Equations (2.13) and (2.14) may be thought of as expressing the same fact, since $hF(q) = h \cdot (\zeta_A/h) \cdot (F(q)/q) = \zeta_A F(q)/q = \zeta_A \tilde{F}(q)$.

If the assumption is made that the bottom topography does not depend on the zonal coordinate x , then another conserved quantity is the zonal momentum

$$M = h \left(u - \int^y f(\xi) d\xi \right).$$

where $f(y)$ is the Coriolis parameter, stated with an arbitrary latitude dependence. (McPhaden and Ripa 1990; Ren and Shepherd 1997). It is easily checked, using the conservation of momentum (2.6) and mass (2.7), that

$$\frac{\partial M}{\partial t} + \nabla \cdot \left(\mathbf{v}M + \mathbf{i}\frac{1}{2}gh^2 \right) = 0,$$

where \mathbf{i} is the unit vector in the x -direction. This is a conservation law for M .

2.2.2 Frictional effects

Since we will study models that contain a parameterization of vertical friction, we briefly review in this section the effects of a small but nonzero amount of friction in a rotating system, where the friction is between the fluid and the bottom solid boundary. We neglect horizontal friction and the surface wind stress in this discussion. Further details may be found in the text by Pedlosky (1987).

For a small amount of friction, the flow may be thought of as being separated into an interior inviscid flow and a frictional boundary layer. The boundary layer near a solid bottom boundary in a rotating system is called an Ekman layer and has a thickness on the order of

$$\delta_E = \sqrt{\frac{2\nu_z}{f}}.$$

where ν_z is a vertical eddy viscosity coefficient and f is the Coriolis parameter (Pedlosky 1987). Within the Ekman layer, friction allows fluid to flow down the pressure gradient (i.e. geostrophic balance is broken), which sets up patterns of convergence

and divergence that are different than in the interior inviscid region. By the conservation of mass, convergence (divergence) in the Ekman layer results in upward (downward) vertical mass flux out of (into) the Ekman layer itself. This phenomenon is called Ekman pumping. Assuming nearly geostrophic flow, the vertical velocity at the top of the Ekman layer may be related to the vorticity of the interior inviscid flow (Pedlosky 1987),

$$w_E = \frac{\delta_E}{2} \zeta,$$

where $\zeta = \partial v / \partial x - \partial u / \partial y$ is the relative vorticity of the interior flow.

This vertical velocity into or out of the interior flow affects the vorticity balance in the interior. Assuming the interior flow may be modelled with the inviscid shallow-water equations, the Ekman pumping may be thought of as a mass source, so that the equations of motion, (2.6) and (2.7), become

$$\frac{\partial \mathbf{v}}{\partial t} + \mathbf{v} \cdot \nabla \mathbf{v} + f \mathbf{k} \times \mathbf{v} = -g \nabla (h + h_B),$$

$$\frac{\partial h}{\partial t} + \nabla \cdot (h \mathbf{v}) = \frac{\delta_E}{2} \zeta.$$

We form the equation governing the evolution of potential vorticity by taking the curl of the momentum equations and eliminating the divergence term using the mass equation. The result is

$$\frac{\partial}{\partial t} \left(\frac{\zeta + f}{h} \right) + \mathbf{v} \cdot \nabla \left(\frac{\zeta + f}{h} \right) = -\frac{\delta_E (\zeta + f)}{2h^2} \zeta.$$

Under the assumption of nearly geostrophic flow, $\zeta + f \approx f$. Then the potential

vorticity equation may be written in the form

$$\frac{\partial}{\partial t} \left(\frac{\zeta + f}{h} \right) + \mathbf{v} \cdot \nabla \left(\frac{\zeta + f}{h} \right) = -\frac{r}{h} \zeta, \quad (2.15)$$

where $r = \delta_E f / (2h)$. This says that *potential* vorticity is dissipated by a sink term proportional to the *relative* vorticity. In fact, this dissipation is through vortex tube stretching and compression resulting from the Ekman pumping associated with the relative vorticity. Note that, if f and h are assumed constant, (2.15) reduces to the statement that relative vorticity is dissipated by a term proportional to the relative vorticity itself, with proportionality coefficient r (Pedlosky 1987).

Suppose that, instead of modelling vertical friction effects with an Ekman pumping term providing a mass source, the friction effects are modelled with Rayleigh damping terms providing a velocity drag,

$$\begin{aligned} \frac{\partial \mathbf{v}}{\partial t} + \mathbf{v} \cdot \nabla \mathbf{v} + f \mathbf{k} \times \mathbf{v} &= -g \nabla (h + h_B) - r \mathbf{v}, \\ \frac{\partial h}{\partial t} + \nabla \cdot (h \mathbf{v}) &= 0. \end{aligned}$$

with the same $r = \delta_E f / (2h)$ as the drag coefficient. The potential vorticity equation of this model is exactly

$$\frac{\partial}{\partial t} \left(\frac{\zeta + f}{h} \right) + \mathbf{v} \cdot \nabla \left(\frac{\zeta + f}{h} \right) = -\frac{r}{h} \zeta,$$

which is identical to (2.15). That is, although the physical mechanisms of mass source (via Ekman pumping) and velocity drag are different from the point of view of mass and momentum balance, they affect the vorticity evolution in exactly the same way. This fact will be exploited in our choice of idealized model in Section 3.1.

2.3 Equatorial waves

2.3.1 Review of barotropic wave theory

Particular dynamics exist at the equator, so it is useful to briefly review the theory of equatorial waves. The barotropic and two-layer baroclinic waves we discuss here will be relevant to the two-layer model we derive in Chapter 4. This work was first conducted by Matsuno (1966b), and further details may be found in textbooks such as Pedlosky (1987) or Holton (1992).

We focus on the horizontal structure of equatorial waves. The vertical structure may be factored out of the equations of motion using separation of variables (Pedlosky 1987). Alternately, one may assume the vertical structure consists of a relatively thin active layer and an infinitely thick inactive layer, i.e. the reduced gravity or one-and-a-half layer model. The case where the motion may be described by two active layers of unequal thicknesses is treated in the next section.

It is assumed that the fluid is described by the shallow-water equations, (2.6) and (2.7), with mean depth H . The equatorial beta plane approximation is made, replacing the Coriolis parameter f with βy , where y is the meridional coordinate. Neglecting variable bottom topography and linearizing about a state of no motion yields the equations

$$\begin{aligned}u_t - \beta y v &= -g\eta_x, \\v_t + \beta y u &= -g\eta_y.\end{aligned}\tag{2.16}$$

$$\eta_t + H(u_x + v_y) = 0,$$

where u, v , and η are the eastward velocity, northward velocity, and height deviation from H , respectively. Under the assumption of zonally propagating waves of the form

$$\{u, v, \eta\} = \{\tilde{u}(y), \tilde{v}(y), \tilde{\eta}(y)\} \exp[i(kx - \omega t)] + \text{c.c.},$$

where c.c. denotes the complex conjugate of the preceding expression, the amplitudes of the waves are governed by the ordinary differential equations

$$\begin{aligned} -i\omega\tilde{u} - \beta y\tilde{v} &= -ikg\tilde{\eta}, \\ -i\omega\tilde{v} + \beta y\tilde{u} &= -g\tilde{\eta}_y, \\ -i\omega\tilde{\eta} + H(ik\tilde{u} + \tilde{v}_y) &= 0. \end{aligned} \tag{2.17}$$

The first of these equations may be used to eliminate \tilde{u} from the remaining equations. to obtain

$$i(\beta^2 y^2 - \omega^2)\tilde{v} + g(\omega\tilde{\eta}_y + k\beta y\tilde{\eta}) = 0. \tag{2.18}$$

$$i(gHk^2 - \omega^2)\tilde{\eta} + H(\omega\tilde{v}_y - k\beta y\tilde{v}) = 0. \tag{2.19}$$

The solution corresponding to $\tilde{v} \equiv 0$ is called the equatorial Kelvin wave. From (2.19), the dispersion relation for this mode is $\omega = \pm\sqrt{gH}k$. That is, this is a nondispersive wave with the same dispersion relation as shallow-water gravity waves. Denote $c = \pm\sqrt{gH}$. The solution of (2.18) is then $\tilde{\eta}(y) \propto \exp(-\beta y^2/2c)$. For the solution to be bounded as $y \rightarrow \pm\infty$, c must be positive. Thus the equatorial Kelvin wave solutions are trapped near the equator (that is, they decay exponentially away from

the equator), exhibit no meridional motion and always travel eastward with the speed of a shallow-water gravity wave.

In fact, it is exactly this equatorial Kelvin wave propagating eastward that allows the equatorial Pacific Ocean to alter its condition from a La Niña state to an El Niño state. In a La Niña state, westward winds at the equator cause the layer of warm surface water to preferentially deepen in the western part of the basin. When those winds weaken, an equatorial Kelvin wave propagates eastward along the thermocline, deepening the surface layer in the eastern part of the equatorial Pacific, establishing El Niño conditions (Neelin, Latif, and Jin 1994).

The non-Kelvin wave solutions are sought by forming a single equation for \tilde{v} from (2.18) and (2.19).

$$\frac{d^2\tilde{v}}{dy^2} + \left[\frac{\omega^2}{gH} - \beta \frac{k}{\omega} - k^2 - \frac{\beta^2}{gH} y^2 \right] \tilde{v} = 0, \quad (2.20)$$

which, by a change of variables $Y = (\beta/\sqrt{gH})^{1/2}y$, may be transformed into

$$\frac{d^2\tilde{v}}{dY^2} + \left[\frac{\sqrt{gH}}{\beta} \left(\frac{\omega^2}{gH} - \beta \frac{k}{\omega} - k^2 \right) - Y^2 \right] \tilde{v} = 0.$$

Note that the derivation of (2.20) required the assumption that $\omega \neq ck$. A solution that remains bounded as $y \rightarrow \pm\infty$ exists if and only if

$$\frac{\sqrt{gH}}{\beta} \left(\frac{\omega^2}{gH} - \beta \frac{k}{\omega} - k^2 \right) = 2n + 1; \quad n = 0, 1, 2, \dots$$

and that solution is $\tilde{v} = H_n(Y) \exp(-Y^2/2)$, where $H_n(Y)$ is the n th Hermite polynomial (Butkov 1968). This dispersion relation may be nondimensionalized by ex-

pressing it in terms of $\tilde{\omega} = \omega/(\beta\sqrt{gH})^{1/2}$ and $\tilde{k} = k(\sqrt{gH}/\beta)^{1/2}$.

$$\tilde{\omega}^2 - \frac{\tilde{k}}{\tilde{\omega}} - \tilde{k}^2 = 2n + 1; \quad n = 0, 1, 2, \dots \quad (2.21)$$

For positive integers n , (2.21) has for any given \tilde{k} three solutions for $\tilde{\omega}$, corresponding to the westward and eastward propagating planetary-scale gravity waves and the westward propagating equatorial Rossby wave. For $n = 0$, there are only two solutions. The third solution, $\tilde{\omega} = -\tilde{k}$, must be rejected since we assumed that $\omega \neq ck$ in the derivation of (2.20). The $n = 0$ mode is called a mixed Rossby-gravity wave (sometimes called a Yanai wave) because, particularly at high wave numbers, the eastward propagating wave behaves like a gravity wave and the westward propagating wave behaves like a Rossby wave.

The dispersion diagram for the various modes is displayed in Figure 2.1. Note that the equatorial Kelvin wave is sometimes labelled as the $n = -1$ mode since $\tilde{\omega} = \tilde{k}$ is indeed a solution of (2.21) when $n = -1$.

2.3.2 Two-layer waves

We seek to describe equatorial waves under the assumption of two-layer dynamics where the layers may be unequal in mean depth. Let the upper and lower layer mean depths be denoted H_1 and H_2 , respectively. Assuming shallow-water theory applies to each layer, the linearized equations of motion are

$$u_{1t} - \beta y v_1 = -g\eta_x.$$

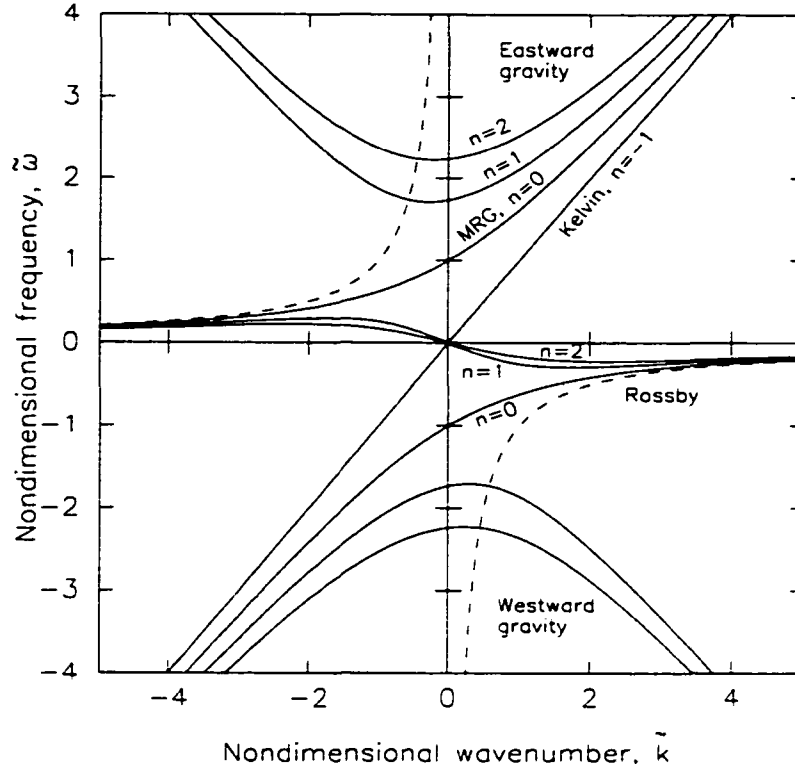


Figure 2.1: The dispersion diagram for equatorial waves. MRG stands for the mixed Rossby-gravity mode. The dotted line shows $\tilde{\omega} = -1/\tilde{k}$, which is relevant for the barotropic modes of two-layer waves.

$$v_{1t} + \beta y u_1 = -g\eta_y.$$

$$-h_t + H_1(u_{1x} + v_{1y}) = 0. \quad (2.22)$$

$$u_{2t} - \beta y v_2 = -g\eta_x - g'h_x.$$

$$v_{2t} + \beta y u_2 = -g\eta_y - g'h_y.$$

$$h_t + H_2(u_{2x} + v_{2y}) = 0.$$

where numeric subscripts refer to the layer (1 for upper, 2 for lower), variable subscripts denote partial derivatives, η is the upper-layer pressure, h is the lower-layer height deviation from H_2 and $g' = g(\rho_2 - \rho_1)/\rho_2$ is the reduced gravity. The rigid-

lid approximation has been made by neglecting η_t as compared to h_t in the third equation, and by neglecting $g'\eta$ as compared to $g'h$ and $g\eta$. This will be a reasonable approximation for the large length scales and small density differences under consideration here.

Equations (2.22) may be combined into two sets of equations that can be solved independently. The baroclinic equations are formed by subtracting the upper layer momentum equations from the lower layer momentum equations, and subtracting H_2 times the upper layer mass equation from H_1 times the lower layer mass equation.

$$\begin{aligned}
 (u_2 - u_1)_t - \mathcal{J}y(v_2 - v_1) &= -g'h_x, \\
 (v_2 - v_1)_t + \mathcal{J}y(u_2 - u_1) &= -g'h_y, \\
 h_t + \frac{H_1 H_2}{H_1 + H_2} [(u_2 - u_1)_x + (v_2 - v_1)_y] &= 0.
 \end{aligned} \tag{2.23}$$

The barotropic equations are formed by adding H_1 times the upper layer momentum equations to H_2 times the lower layer equations, and adding the two conservation of mass equations together. These equations take the form

$$\begin{aligned}
 (H_1 u_1 + H_2 u_2)_t - \mathcal{J}y(H_1 v_1 + H_2 v_2) &= -g(H_1 + H_2)\eta_x - g'H_2 h_x, \\
 (H_1 v_1 + H_2 v_2)_t + \mathcal{J}y(H_1 u_1 + H_2 u_2) &= -g(H_1 + H_2)\eta_y - g'h_y, \\
 (H_1 u_1 + H_2 u_2)_x + (H_1 v_1 + H_2 v_2)_y &= 0.
 \end{aligned} \tag{2.24}$$

The baroclinic equations (2.23) are in the exact same form as the one-layer equations (2.16), and so have already been solved in the previous section. That is, defining the baroclinic velocities $u_{bc} = u_2 - u_1$ and $v_{bc} = v_2 - v_1$, the baroclinic equations will

have wave solutions with

$$\{u_{bc}, v_{bc}, h\} = \{\tilde{u}(y), \tilde{v}(y), \tilde{h}(y)\} \exp[i(kx - \omega t)] + \text{c.c.},$$

where c.c. stands for the complex conjugate of the preceding expression, only when k and ω are related so that their nondimensional forms

$$\tilde{\omega} = \omega/(\beta c)^{1/2} \text{ and } \tilde{k} = k(c/\beta)^{1/2}, \text{ where } c = \sqrt{\frac{g' H_1 H_2}{H_1 + H_2}}.$$

fall upon one of the dispersion curves shown in Figure 2.1. If we take $\beta = 2\Omega/r_0 \approx 2.27 \times 10^{-11} \text{ m}^{-1} \text{ s}^{-1}$ (where Ω is the angular velocity of the Earth and r_0 is the Earth's radius), $H_1 = 4000 \text{ m}$, $H_2 = 400 \text{ m}$, and $g' = 1.7 \times 10^{-3} \text{ m/s}^2$ (Stephens and Marshall 2000), then $c \approx 0.79 \text{ m/s}$ and so $\tilde{\omega} = 1$ corresponds to $\omega \approx 4.2 \times 10^{-6} \text{ s}^{-1}$, which implies a wave period of 17.2 days. With those same parameters, $\tilde{k} = 1$ corresponds to $k \approx 5.4 \times 10^{-6} \text{ m}^{-1}$, for a wavelength of 1200 km.

Defining the barotropic variables

$$u_{bt} = \frac{H_1 u_1 + H_2 u_2}{H_1 + H_2}, \quad v_{bt} = \frac{H_1 v_1 + H_2 v_2}{H_1 + H_2}, \text{ and } \phi = \eta + \frac{\rho_2 - \rho_1}{\rho_2} \frac{H_2}{H_1 + H_2} h.$$

the barotropic equations (2.24) take the form

$$u_{btt} - \beta y v_{bt} = -g \phi_x,$$

$$v_{btt} + \beta y u_{bt} = -g \phi_y. \quad (2.25)$$

$$u_{btx} + v_{bty} = 0.$$

These are similar to the one-layer equations (2.16), except that the velocity is non-divergent. Just as with the one-layer equations, we may assume a wave solution and

form a single ordinary differential equation governing the amplitude of v_{bt} .

$$\frac{d^2 \bar{v}}{dy^2} + \left[-\beta \frac{k}{\omega} - k^2 \right] \bar{v} = 0, \quad (2.26)$$

which is almost exactly like (2.20), except without any of the terms involving H . This is consistent with the fact that the nondivergent case may be thought of as the $H \rightarrow \infty$ limit of the system. The only nontrivial solutions that remain bounded as $y \rightarrow \pm\infty$ are wave solutions in the meridional direction, and these exist only under the condition that

$$-\beta \frac{k}{\omega} - k^2 > 0.$$

Nondimensionalizing k and ω as $\tilde{\omega} = \omega/(\beta c)^{1/2}$ and $\tilde{k} = k(c/\beta)^{1/2}$, for any speed c , this condition is equivalent to

$$\begin{aligned} -\frac{1}{\tilde{k}} < \tilde{\omega} < 0, \quad \text{for } \tilde{k} > 0. \\ 0 < \tilde{\omega} < -\frac{1}{\tilde{k}}, \quad \text{for } \tilde{k} < 0. \end{aligned} \quad (2.27)$$

For brevity in what follows, this condition for the existence of nontrivial solutions to the barotropic equations will be referred to as the *barotropic condition*. For comparison, $\tilde{\omega} = -1/\tilde{k}$ is displayed on the dispersion diagram (Figure 2.1) as a dotted line. Let the meridional wave number be denoted by l . Then, for any k and ω such that the above barotropic condition is satisfied (equivalently, for any $(\tilde{k}, \tilde{\omega})$ on the dispersion diagram located between the dotted line and the \tilde{k} -axis), a wave solution exists to the barotropic equations, with meridional wave number

$$l^2 = -\beta \frac{k}{\omega} - k^2.$$

This relation may be rearranged to find the dispersion relation for this mode:

$$\omega = -\frac{\beta k}{k^2 + l^2}.$$

Thus, these solutions are merely Rossby waves.

If there exist $(\tilde{k}, \tilde{\omega})$ for which both baroclinic and barotropic modes can simultaneously exist, then interaction between the barotropic and baroclinic modes is a possibility. For which $(\tilde{k}, \tilde{\omega})$, then, do both baroclinic and barotropic modes exist? Since baroclinic modes exist only along the curves appearing in the dispersion diagram (Figure 2.1), and barotropic modes exist for any $(\tilde{k}, \tilde{\omega})$ satisfying the barotropic condition, the question reduces to: Which modes in the dispersion diagram satisfy the barotropic condition?

From the dispersion diagram, it appears that no eastward travelling gravity waves, no Kelvin waves, only some westward travelling gravity waves, only the westward travelling mixed Rossby-gravity waves, and all of the baroclinic Rossby wave modes satisfy the barotropic condition. In the discussion below, we confirm these statements analytically.

From the dispersion diagram, it appears that only some of the equatorial wave modes satisfy the barotropic condition: some westward-travelling gravity waves, the westward-travelling mixed Rossby-gravity waves, and all of the baroclinic Rossby wave modes. The following wave modes appear not to satisfy the barotropic condition: the eastward-travelling gravity waves, the Kelvin waves, the eastward-travelling mixed Rossby-gravity waves, and some of the westward-travelling gravity waves. In the

discussion below, we confirm these statements analytically.

The westward propagating gravity waves satisfy the barotropic condition only for sufficiently small wave numbers. In fact, by substituting $\tilde{\omega} = -1/\tilde{k}$ into the dispersion relation (2.21), it may be shown that the mode- n baroclinic gravity wave associated with $(\tilde{k}, \tilde{\omega})$ can couple with barotropic Rossby waves exactly when

$$\tilde{k} < \frac{1}{\sqrt{2n+1}}, \quad \text{for } \tilde{k} > 0.$$

$$\tilde{k} > -\frac{1}{\sqrt{2n+1}}, \quad \text{for } \tilde{k} < 0.$$

To show analytically that the westward propagating Rossby-gravity wave and all the baroclinic Rossby modes satisfy the barotropic condition, we will assume that $\tilde{k} > 0$ and $\tilde{\omega} < 0$, and we will demonstrate that $\tilde{k} < -1/\tilde{\omega}$ for these modes. Since the entire dispersion diagram is antisymmetric (i.e. $\tilde{\omega}$ is an antisymmetric function of \tilde{k} for all modes), similar arguments may be applied for $\tilde{k} < 0$ and $\tilde{\omega} > 0$.

The dispersion relation for the Rossby-gravity mode may be written

$$\tilde{\omega}^2 - \tilde{k}\tilde{\omega} - 1 = 0.$$

which is (2.21) with the $\tilde{\omega} + \tilde{k} = 0$ mode factored out. By solving for \tilde{k} ,

$$\tilde{k} = -\frac{1}{\tilde{\omega}} + \tilde{\omega} < -\frac{1}{\tilde{\omega}}.$$

it is immediately apparent that this mode satisfies the barotropic condition.

We may regard the dispersion relation (2.21) as a quadratic equation in \tilde{k} , and so express \tilde{k} as a function of $\tilde{\omega}$,

$$\tilde{k} = \frac{-1 \pm \sqrt{1 + 4\tilde{\omega}^4 - 4(2n+1)\tilde{\omega}^2}}{2\tilde{\omega}}.$$

The Rossby modes correspond to $n \geq 1$ and $-1 < \tilde{\omega} < 0$, i.e. $0 < \tilde{\omega}^2 < 1$. The negative sign in the numerator corresponds to the part of the curve that asymptotically approaches 0 as $\tilde{k} \rightarrow \infty$ (more specifically, that part of the curve where $\tilde{k} > -1/(2\tilde{\omega})$) and the positive sign describes the $0 \leq \tilde{k} < -1/(2\tilde{\omega})$ part of the curve. We choose the negative sign because the $\tilde{k} < -1/(2\tilde{\omega})$ part of the curve clearly satisfies the barotropic condition. Since $2n + 1 - \tilde{\omega}^2 > 0$ for any positive n ,

$$\tilde{k} = \frac{1 + \sqrt{1 - 4\tilde{\omega}^2[2n + 1 - \tilde{\omega}^2]}}{-2\tilde{\omega}} < \frac{1 + \sqrt{1}}{-2\tilde{\omega}} = -\frac{1}{\tilde{\omega}},$$

and so all the Rossby modes satisfy the barotropic condition.

In this chapter, we have established that shallow-water theory is appropriate to study large-scale equatorial flow: we have reviewed some of the well-known features of shallow-water theory, both in the inviscid limit and in the context of Ekman dynamics; and we have reviewed the theory of equatorial waves in one and two shallow layers. In the next chapter, we will investigate a simple model of equator-crossing flow and compare its dynamics to those of the one-layer shallow-water model. In the subsequent chapter, we derive a two-layer model of equatorial flow which is shown to contain the waves discussed here.

Chapter 3

One-layer model

The frictional geostrophic model employed by Stephens and Marshall (2000) includes frictional effects, allows the flow to be steered by topography, and supplies a diagnostic relation for the velocity field in terms of the pressure field which, unlike the usual geostrophic relations, remains valid even at the equator. However, even though this model has been used to study one-layer equator crossing flow in the literature, the model has not been evaluated to determine which aspects of the dynamics it retains and which it neglects. In this chapter, we compare the frictional geostrophic model to the more realistic shallow-water equations to ascertain how well the model captures the essential physics of the problem.

The reduced-gravity shallow-water model is itself a crude approximation to abyssal dynamics. Neglected effects include turbulent entrainment, vertical overturning behaviour, and baroclinic effects. Possible improvements to the model include employ-

ing several shallow layers to mimic an isopycnal coordinate system. We also caution that, as shown by de Verdière and Schopp (1994) and confirmed in the analysis of Section 2.1, the “horizontal component” of the Coriolis force, which is neglected as part of the hydrostatic approximation, may be important in equatorial dynamics, particularly if the horizontal length scales of motion are smaller than $(Hr_0)^{1/2}$, where H is a vertical scale of the motion and r_0 is the radius of the earth. For a vertical scale of $H = 200$ m, this length scale is on the order of 40 km, which is smaller than the $O(500$ km) length scales we study here, and thus the traditional approximation is retained.

3.1 Frictional geostrophic model

Models in which the momentum equations have been reduced to the geostrophic relations with the addition of a linear term representing the effects of friction have been used to study various large-scale motions by several authors (see Stephens and Marshall 2000; Edwards, Willmott, and Killworth 1998; Samelson 1998; Samelson and Vallis 1997, and further references therein). The model may be written

$$-fv = -g' \frac{\partial(h + h_B)}{\partial x} - ru, \quad (3.1)$$

$$fu = -g' \frac{\partial(h + h_B)}{\partial y} - rv, \quad (3.2)$$

$$\frac{\partial h}{\partial t} + \nabla \cdot (h\mathbf{u}) = 0. \quad (3.3)$$

where $\mathbf{u} = (u, v)$ is the horizontal velocity, h is the height of the fluid layer, h_B is the bottom topography elevation, g' is the reduced gravity, and r is a damping coefficient to be specified.

We observed in Section 2.2.2 (see also Pedlosky 1987; Stephens and Marshall 2000; Kawase and Straub 1991) that, from a vorticity evolution point of view, the effect of a bottom Ekman layer is equivalent to the effect of linear Rayleigh friction with a coefficient $r = (\nu_z f/2)^{1/2}/h = f\delta_E/2h$, where ν_z is a vertical eddy viscosity coefficient, δ_E is the Ekman layer thickness, and h is the layer thickness. This implies that $r \rightarrow 0$ at the equator. In order to allow friction to be nonzero at the equator, Stephens and Marshall (2000) neglect the dependence of r on f , but retain the h dependence. However, Edwards *et al.* (1998), Samelson (1998) and Samelson and Vallis (1997) all neglect the h dependence as well, taking r to be a prescribed constant. For simplicity we will take r to be independent of f and h in this study.

Modelling friction effects with Rayleigh damping terms has the advantage of allowing the velocities to be solved for in a *diagnostic* relation in terms of the pressure gradients.

$$u = g' \frac{-f p_y - r p_x}{f^2 + r^2}, \quad v = g' \frac{f p_x - r p_y}{f^2 + r^2}. \quad (3.4)$$

where $p = h + h_B$ and subscripts denote partial derivatives. It is important to note that (for $r \neq 0$) these equations do not have a singularity at $f = 0$, unlike the usual geostrophic relations. Thus, the model contains a geostrophic component (terms proportional to f in the numerator), and a down-pressure-gradient component

(terms proportional to r in the numerator). In the limit as $f \rightarrow 0$, the motion is that of a potential flow. Note that frictional effects prevent the unbounded acceleration of the fluid downhill, since the downhill component may be interpreted to represent the terminal velocity that the fluid would attain when acceleration and friction effects are in balance at steady state.

A consequence to the form of (3.4) is that the component of velocity parallel to the pressure gradient is necessarily in the direction opposite to that gradient. From (3.4),

$$\begin{aligned}
\mathbf{u} \cdot \nabla p &= g' \frac{-f p_y - r p_x}{f^2 + r^2} p_x + g' \frac{f p_x - r p_y}{f^2 + r^2} p_y \\
&= \frac{g'}{f^2 + r^2} (-f p_y p_x - r p_x^2 + f p_y p_x - r p_y^2) \\
&= -\frac{g' r}{f^2 + r^2} (p_x^2 + p_y^2) \\
&= -\frac{g' r}{f^2 + r^2} |\nabla p|^2 \\
&\leq 0.
\end{aligned}$$

Geometrically, $\mathbf{u} \cdot \nabla p \leq 0$ means the velocity and pressure-gradient vectors have an angle $\theta \geq \pi/2$ between them. Roughly speaking, the velocity may have a downhill component, but never an uphill one.

The model may be written as a single evolution equation for the height field, h , by substituting the velocity relations (3.4) into the conservation of mass equation (3.3),

$$h_t + J \left(g' (h + h_B), \frac{h f}{f^2 + r^2} \right) = r \nabla \cdot \left[\frac{g' h \nabla (h + h_B)}{f^2 + r^2} \right]. \quad (3.5)$$

where $J(A, B) = A_x B_y - A_y B_x$. This form of the model reveals that, despite its simplicity, it is a nonlinear model. As well, it is clear that r determines how diffusive

the model will be, since it multiplies the diffusion-type operator on the right-hand side of the equation. In the $r \rightarrow 0$ and $f \rightarrow 1$ limit, this equation reduces to the lower layer of the (uncoupled) Swaters and Flierl (1991) model, that is, planetary geostrophy.

The nonlinearity in the right-hand side friction term is a result of modelling friction with Rayleigh damping. Had we modelled friction with a mass source term representing Ekman pumping, the right-hand side of this equation would be linear in h . However, the geostrophic relations would have had a singularity at $f = 0$, and so such a model could not have been used to study cross-equatorial flow.

The potential vorticity equation of this model is

$$\frac{\partial}{\partial t} \left(\frac{f}{h} \right) + \mathbf{u} \cdot \nabla \left(\frac{f}{h} \right) = -\frac{r}{h} \zeta, \quad (3.6)$$

where $\zeta = \partial v / \partial x - \partial u / \partial y$ is the relative vorticity. By comparing this equation to the potential vorticity equation of shallow-water theory with Ekman friction (2.15), we see that this model neglects relative vorticity in favour of planetary vorticity, and it simulates the dissipation of potential vorticity by Ekman friction.

Although $r \neq 0$, r is considered to be a small parameter. The potential vorticity equation (3.6) may be investigated to see the behaviour this model predicts in the small- r parameter regime. In the limit as $r \rightarrow 0$, (3.6) states that f/h is conserved following the flow. This implies that, for small r (to be precise, r is assumed to be small relative to the largest value of f , i.e. $0 < r \ll \max|f|$), a mass of fluid approaching the equator will tend to decrease in height, since $|f|$ decreases as the

equator is approached. This process continues until the right hand side of (3.6) becomes non-negligible, which is when $r/h \sim O(1)$ (nondimensional values). This represents the point at which the effects of friction will be dynamically important. Under the assumption that h and f are each $O(1)$ initially, frictional effects will thus be important at a latitude where $f = O(r)$; that is, at a nondimensional distance from the equator of r/β , where $\beta = df/dy$ at $y = 0$. With $r = 0.05$, $\beta = 1$ and $L = 500$ km, this corresponds to a dimensional distance of 25 km.

An equation expressing the evolution of potential energy in this model is found as follows: Writing (3.1) and (3.2) into the vector form

$$r\mathbf{u} + f\mathbf{k} \times \mathbf{u} + \nabla\Phi = \mathbf{0},$$

where $\Phi = g'(h + h_B)$, we take the inner product of this equation and $h\mathbf{u}$ to find

$$rh\mathbf{u} \cdot \mathbf{u} + h\mathbf{u} \cdot \nabla\Phi = 0. \quad (3.7)$$

Upon multiplying Φ by the conservation of mass equation (3.3), it is found that

$$\frac{\partial}{\partial t} \left(\frac{1}{2}gh^2 + gh h_B \right) + \Phi \nabla \cdot (h\mathbf{u}) = 0,$$

which, by using (3.7), may be written in the form

$$\frac{\partial}{\partial t} \left(\frac{1}{2}gh^2 + gh h_B \right) + \nabla \cdot (\Phi h\mathbf{u}) = -rh\mathbf{u} \cdot \mathbf{u}. \quad (3.8)$$

Equation (3.8) is the equation analogous to the conservation of energy in the shallow-water model (2.10). However, (3.8) implies that potential energy, $\frac{1}{2}gh^2 + gh h_B$, is not conserved in this model, but, in fact, decreases with time. It appears that the rate

of potential energy dissipation is simply proportional to the damping parameter r : however.

$$\begin{aligned} \mathbf{u} \cdot \mathbf{u} &= \frac{(g')^2}{(f^2 + r^2)^2} [(-fp_y - rp_x)^2 + (fp_x - rp_y)^2] \\ &= \frac{(g')^2}{f^2 + r^2} [p_x^2 + p_y^2]. \end{aligned} \tag{3.9}$$

so that the potential energy dissipation is only proportional to r as long as $f \gg r$.

Very near the equator, where $f \ll r$, the velocity is proportional to $1/r$, and thus the dissipation of potential energy is actually proportional to $1/r$ there.

The major disadvantage of this model is its oversimplification of the dynamics. In particular, fluid inertia has been neglected. Since the fluid must always move down the pressure gradient, a mass of fluid flowing down one side of an ocean basin does not have the momentum to flow back up the other side.

It is not expected that this model will reproduce the realistic dynamics within the equatorial region. The model will be evaluated on its ability to predict the *net* effect on a geostrophically balanced flow as it passes through the equatorial region, and emerges on the other side or recirculates, again geostrophically balanced.

3.2 Numerical methods

We numerically integrate forward in time the reduced-gravity shallow-water model, (2.6) and (2.7), and the frictional geostrophic model, (3.3) and (3.4), in order to compare the two models. The shallow-water model may be written in nondimensional

form as

$$\frac{\partial \mathbf{u}}{\partial t} + \mathbf{u} \cdot \nabla \mathbf{u} + \frac{f}{Ro} \mathbf{k} \times \mathbf{u} = -\frac{1}{Ro} \nabla (h + h_B) + \mathbf{F}_{\text{fric}}, \quad (3.10)$$

$$\frac{\partial h}{\partial t} + \nabla \cdot (\mathbf{u}h) = 0, \quad (3.11)$$

where \mathbf{u} is the horizontal velocity vector. \mathbf{F}_{fric} represents the friction term (see equation 3.12 below for the specific form of friction used). $Ro = U/f_0L$ is the Rossby number, and U , L , f_0 , and h_0 are typical scales for the velocity, length, Coriolis parameter and fluid depth, respectively. It has been assumed that the time variable is scaled advectively, $T = L/U$, for a time scale T , and that the scale slope for the bottom topography is the same as the scale slope of the fluid height, h_0/L . We have also employed the geostrophic scaling $f_0U = g'h_0/L$, i.e. $U^2/(g'h_0) = Ro$. Since the (dimensional) Coriolis parameter f^* passes through zero in the domain of interest, but we wish to allow the fluid to be in a state of geostrophic balance in part of our numerical domain, we scale f^* by its value $f_0 = 2\Omega \sin \theta_0$ at a latitude θ_0 away from the equator where the flow is geostrophic. Thus, we will take $Ro \ll 1$ and the flow will be in approximate geostrophic balance at $f \approx \pm 1$.

These equations are discretized on an Arakawa C-grid (Figure 3.1, see also Arakawa and Hsu 1990). The spatial discretization of the advection, Coriolis and pressure gradient terms is performed using the scheme of Arakawa and Hsu (1990). This scheme, which is designed to tolerate an arbitrarily small layer thickness (i.e. intersections of the fluid interface with the bottom topography), conserves energy and weakly dissipates potential enstrophy when the mass flux is nondivergent (neglecting friction and

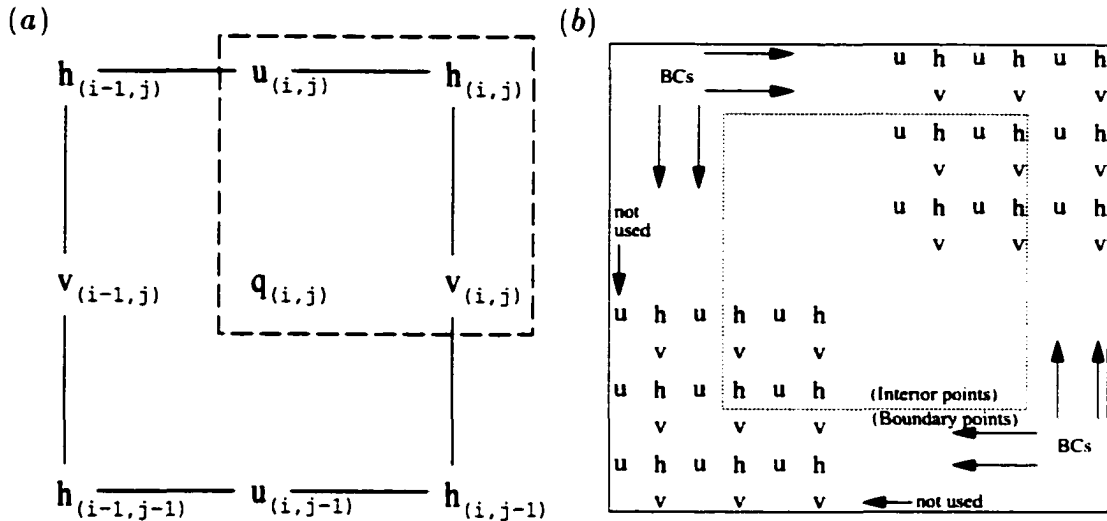


Figure 3.1: The Arakawa C-grid. (a) One cell. q represents vorticity. Note that variables inside the dotted-line box are all labelled identically. (b) Selected points near the edges of the computational domain indicate how the boundary conditions are imposed.

any errors introduced by the time-stepping routine). It is a second-order accurate scheme in space.

We note that the possibility of vanishing layer thickness in the shallow-water equations is an issue that must be carefully treated by the spatial discretization scheme. The momentum equations are discretized in the flux form, (2.8), where the mass flux, $h\mathbf{v}$, multiplies potential vorticity, $q = (\zeta + f)/h$. Near grid points where $h \rightarrow 0$, q may be large, which can lead to numerical instability if care is not taken.

The temporal discretization of the momentum equations is done according to a third-order accurate scheme due to Matsuno (1966a). It is a third-order Runge-Kutta method.

The mass equation is stepped forward in time using the method of Hsu and

Arakawa (1990), which is a predictor-corrector scheme second-order accurate in time and space that maintains the positive-definiteness of the height field h and conserves mass. One other popular method that maintains the positive-definiteness of the layer thickness as it is advanced forward in time is the Flux-Corrected Transport method (Sun, Bleck, and Chassignet 1993). In our tests, we found the scheme of Hsu and Arakawa (1990) to possess superior numerical stability, as compared to the Flux-Corrected Transport method.

To integrate the frictional geostrophic model numerically, the same routine as for the full shallow-water equations is used for the mass equation, but since there is no time derivative to evaluate in the velocity relations (3.4), these are simply evaluated at each time step using second-order accurate central differences for the derivatives.

For all the simulations reported here, the boundary conditions used for the height field were Dirichlet conditions. That is, the height was specified on the boundary, usually to be zero, but nonzero in the case of the inflow simulations performed over realistic topography. Except for inflow conditions, no-slip and no-flux conditions were enforced at the boundary, that is, both components of the velocity were held fixed at zero all along the boundary for all times. For the simulations with inflow conditions, the velocity at the boundary was set to be the geostrophic velocity, based on the topography and the height field of the inflow current at the boundary.

3.3 Parameter values and observations

We have taken friction to be of the form

$$\mathbf{F}_{\text{fric}} = A_H \nabla^2 \mathbf{u} + A_N \nabla^6 \mathbf{u} - A_V \frac{\mathbf{u}}{h^2}, \quad (3.12)$$

where A_H , A_N and A_V are the horizontal, numerical and vertical friction coefficients, respectively. For the simulations reported here $A_H = 10^{-5}$, $A_N = 10^{-9}$, and $A_V = 4 \times 10^{-8}$, unless otherwise noted. These values were all chosen to be as small as possible so that the friction increased the stability of the scheme, but affected the leading-order dynamics as little as possible. The horizontal friction term is intended to represent the effects of horizontal diffusion of momentum by subgrid-scale eddies. The numerical and vertical friction terms are added for numerical stability. Numerical friction effectively removes small scale features, and vertical friction is added only to prevent the unphysical acceleration of massless grid points. (All grid points in the numerical domain, including grid points at which there is no fluid, have velocities associated with them. The topography causes downhill acceleration, even at these massless grid points. The vertical friction term prevents unbounded acceleration at such points.) The horizontal and numerical terms are evaluated at each of the three time levels in the Matsuno (1966a) scheme, but the vertical term is fully implicit at each time step.

Note that the numerical scheme of Arakawa and Hsu (1990) tolerates arbitrarily small thicknesses, but not a thickness of exactly zero, since potential vorticity $q = (\zeta + f)/h$ must be explicitly calculated. Thus, we maintained a minimum nonzero height

field at all grid points. This was set to a nondimensional value of 10^{-5} . Smaller values led to increased numerical instability, and larger values led to poorer conservation of kinetic and potential energy.

Typical velocities observed for the Antarctic Bottom Water current as it approaches the Equator from the south are on the order of several centimetres per second. DeMadron and Weatherly (1994) measured the geostrophic velocity of the current at 25° S latitude at approximately 1–2 cm/s, 2 cm/s at 17° S, and 5 cm/s at 10° S. Rhein, Stramma, and Send (1995) took direct and geostrophic velocity measurements at 5° S, and found a highly variable current with velocities up to 10 cm/s there. Sandoval and Weatherly (2001) also analyzed measurements at $4^{\circ}30'S$, and found velocities in the range 5–8 cm/s. Hall *et al.* (1997) took direct measurements of the velocity (without employing any geostrophic calculations) right at the equator, and found that velocities of approximately 5 cm/s are typical in the centre of the current, with temporal variations giving velocities of up to 10 cm/s. Rhein *et al.* (1995) also measured AABW velocities of 5–10 cm/s in the equatorial channel. Unless otherwise noted, we will assume a velocity scale of 5 cm/s.

When one chooses a value for the parameter g' , thereby setting the density difference between the two layers, one assumes that the density is constant within the current and outside the current, with a jump discontinuity at the interface. This is a rough approximation to the actual density variation, which is continuously varying in the vertical direction even within the current itself, and changes

slightly along the current path (see, for example, the density sections of DeMadron and Weatherly 1994 and Sandoval and Weatherly 2001). Stephens and Marshall (2000), in their numerical simulations of equatorial flow using a simplified model, use $g' = 1.7 \times 10^{-3} \text{ m/s}^2$, but Borisov and Nof (1998) and Nof and Borisov (1998) use a much smaller $g' = 2 \times 10^{-4} \text{ m/s}^2$. In these papers, Nof and Borisov state that they use a g' smaller than is often used because they are studying the core of the current. We will take the more typical value $g' = 1 \times 10^{-3} \text{ m/s}^2$, unless otherwise specified.

It is known that AABW enters and exits the Brazil Basin (a region of the southern Atlantic Ocean between South America and the mid-Atlantic ridge, extending from about 30°S to the equator) through specific channels. The volume flux entering the basin has been measured at $6.9 \times 10^6 \text{ m}^3 \text{ s}^{-1} = 6.9 \text{ Sv}$ (Hogg, Siedler, and Zenk 1999), where Sv stands for the flux units of Sverdrups, and $1 \text{ Sv} = 10^6 \text{ m}^3 \text{ s}^{-1}$. The amount exiting through the equatorial channel northwest of the basin is 2.0–2.2 Sv (Hall *et al.* 1997), and the amount exiting through fracture zones in the mid-Atlantic ridge to the northeast of the basin is $1.22 \pm 0.25 \text{ Sv}$ (Mercier and Speer 1998) (see Figure 3.8 for the geography of the bottom topography). The remaining 3.6 Sv of fluid is believed to upwell, or mix vertically, into shallower waters (Ledwell *et al.* 2000). The behaviour of the current is complicated by the fact that it is believed to split up into two parts with different paths (Sandoval and Weatherly 2001) and that it is highly variable in time (Hall *et al.* 1997; Rhein *et al.* 1995; Mercier and Speer 1998).

The bottom topography and functional form of Coriolis parameter are chosen in a

particular way to provide a clean testing ground for the comparison of the two models. In particular, we are interested in diagnosing how well the propagation speed of an eddy, as predicted by each of the models, agrees with the Nof (1983) speed, $g's/f$, where s is the bottom slope. A nearly constant bottom slope and Coriolis parameter away from the channel bottom and equator facilitates computing this diagnostic. Therefore, the bottom topography is chosen to be a simplified meridional channel with a hyperbolic cross section, $h_B = \sqrt{x^2 + 1}$, which has a slope approaching ± 1 away from $x = 0$, and the Coriolis parameter is chosen to be $f = \tanh(\beta_0 Ly/f_0)$, which tends to a non-dimensional f -plane value of unity away from $y = 0$, and has a slope at $y = 0$ of $\beta_0 L/f_0$. For simulations reported here, $\beta_0 L/f_0 = 1$, which, for f_0 evaluated at 5° latitude, corresponds to choosing a horizontal length scale of $L = 500$ km. The variation of this functional form of the Coriolis parameter is shown in Figure 3.2.

3.4 Flow over idealized topography

The frictional geostrophic (hereafter referred to as FG, not to be confused with the term frontal geostrophic) model and the shallow-water model are compared for flow over simplified bottom topography. The topography takes the shape of a meridional channel. Simulations were performed with all the fluid initially south of the equator, flowing northward along the western half of the channel, in the form of an eddy, i.e. the height field initially had compact support in the domain. The height of the eddy

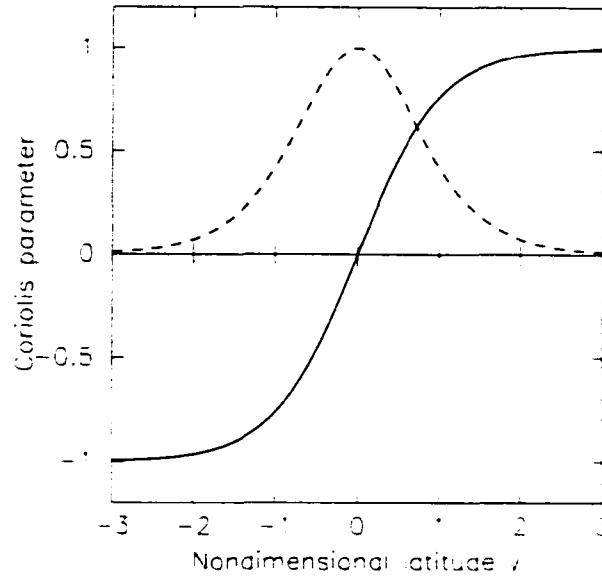


Figure 3.2: Coriolis parameter variation with latitude. Solid line is Coriolis parameter $f = \tanh y$. Dotted line is $df/dy = \text{sech}^2 y$. Nondimensional domain is $-3 \leq y \leq 3$, or dimensionally, $-1500 \text{ km} \leq y^* \leq 1500 \text{ km}$.

is set to have a cosine cross-section.

$$h = \frac{h_{\max}}{2} \left[1 + \cos \left(\frac{\pi R}{R_{\max}} \right) \right], \quad 0 \leq R \leq R_{\max},$$

where $R = \sqrt{(x - x_c)^2 + (y - y_c)^2}$ and (x_c, y_c) , h_{\max} and R_{\max} are specified parameters corresponding to the centre coordinates, height and the radius of the eddy, respectively. This height profile was chosen so that the height field is continuous and differentiable. These initial conditions were chosen, in part, to simulate the Antarctic Bottom Water flow, which flows northward along the western slope toward the equator.

The motion of an isolated eddy, as opposed to a current, is studied in this section because we are evaluating the FG model and not trying to simulate the details of AABW flow. One advantage of isolated eddy simulations over current simulations is

the flow may be easily analyzed in terms of the evolution of the centre of mass of the eddy. The propagation speed of the centre of mass of the eddy will be compared to its theoretical speed (Nof 1983). Numerical simulations of the evolution of a current will be described in the next section, where simulations over realistic topography are discussed.

Several simulations of an isolated abyssal dome of fluid approaching the equator from the south have been carried out varying only the damping parameter r in the case of the FG model, or the Rossby number Ro in the case of the shallow-water model. In Figure 3.3, we show snapshots from a typical simulation employing the shallow-water equations. The panels in Figure 3.3 are labelled with nondimensional time. With $L = 500$ km and $U = 5$ cm/s, one nondimensional time unit corresponds to a dimensional value of $T = L/U = 10^7 s \approx 116$ days. The eddy is observed to propagate along the shelf without losing much height until almost at the equator (top left panel, $t = 0.2$ or $t^* = 23$ days), when fluid starts to accelerate downhill (top right, $t = 1.4$ or $t^* = 162$ days). Part of the fluid is located slightly north of the equator while flowing downhill. The fluid rises up the other side of the channel (bottom left, $t = 2.4$ or $t^* = 278$ days), and ultimately splits into two eddies: one flowing north, the other flowing south (bottom right, $t = 4.0$ or $t^* = 463$ days). This is qualitatively consistent with the simulations of Borisov and Nof (1998), who investigated eddies crossing the equator in a meridional channel.

Figure 3.4 displays the simulation of the motion of the same initial eddy, but as

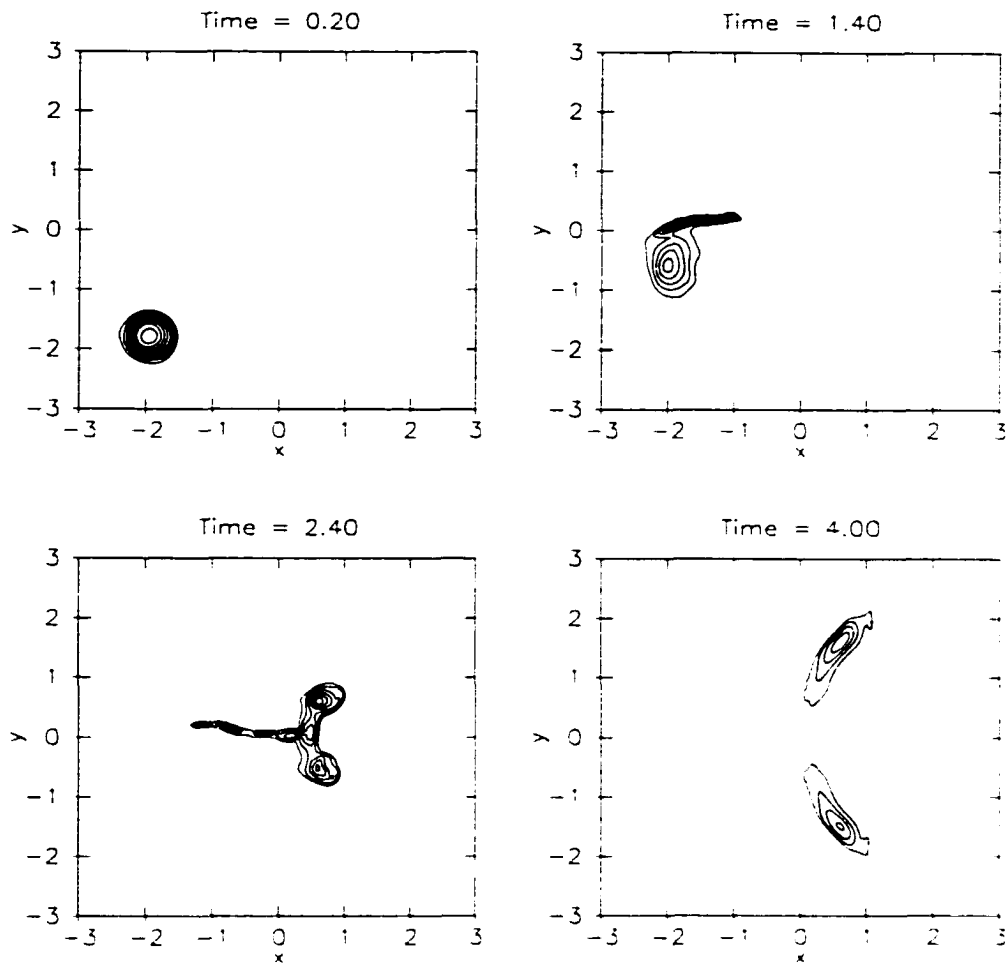


Figure 3.3: The results of a shallow-water simulation. $Ro = 0.02$. The contour spacing is 0.02.

predicted by the FG model. The eddy is seen to travel initially along the slope (top left, $t = 0.2$ or $t^* = 23$ days), as in the shallow-water simulation, but upon reaching the equator, flows directly downhill, with very little fluid found north of the equator as it does so (top right, $t = 1.4$ or $t^* = 162$ days). The fluid pools at the bottom of the channel at the equator (bottom left, $t = 2.4$ or $t^* = 278$ days), and then *proceeds to split into two parts*, one flowing north, and the other recirculating back south (bottom right, $t = 4.0$ or $t^* = 463$ days). Despite the simplicity of the model, it captures the

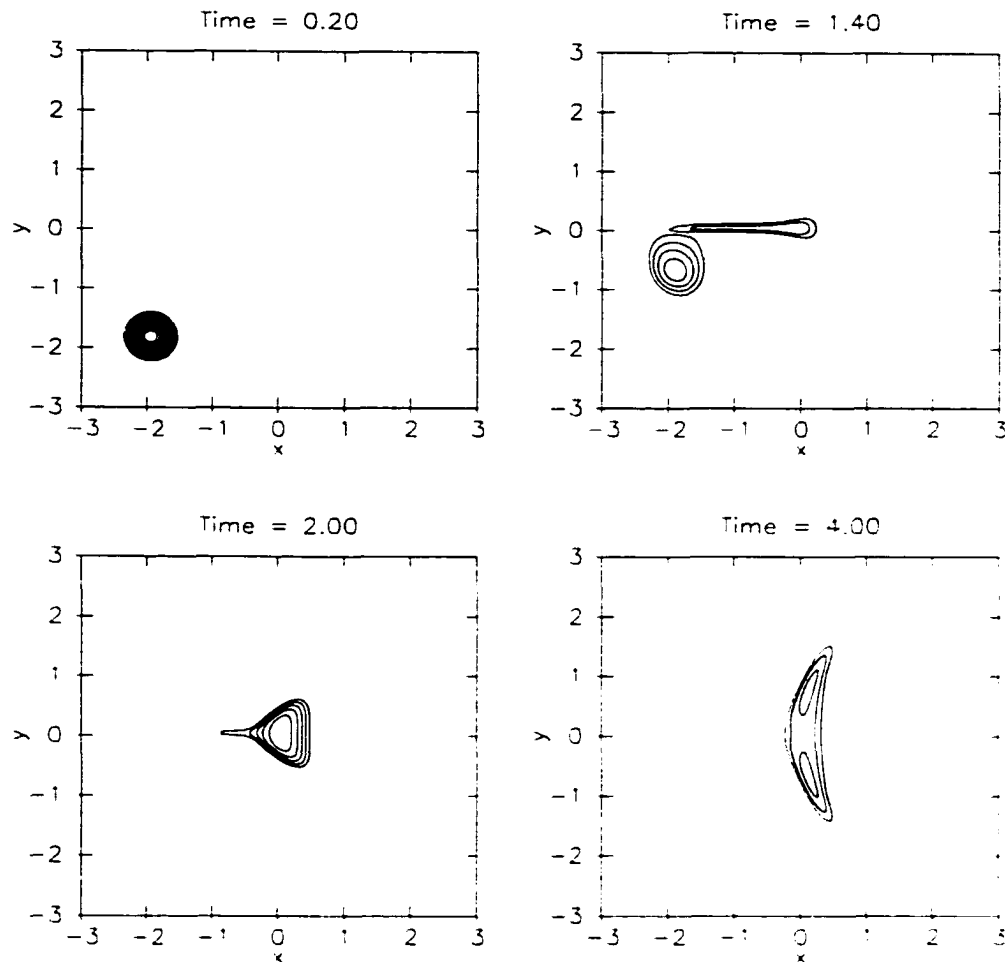


Figure 3.4: The results of an FG model simulation, $r = 0.02$. The contour spacing is 0.02.

characteristic splitting of the fluid into northward and southward flowing parts seen in the shallow-water simulation. The lack of inertia in the model is seen in both the sharp turn from along-slope flow to downhill flow and the immediate deceleration from fast downhill flow to nearly stationary fluid pooling at the equatorial channel bottom. Thus the net result of the lack of inertia in the model is that the north-south splitting of the flow is very symmetric, and that the final flow is very near the bottom of the channel.

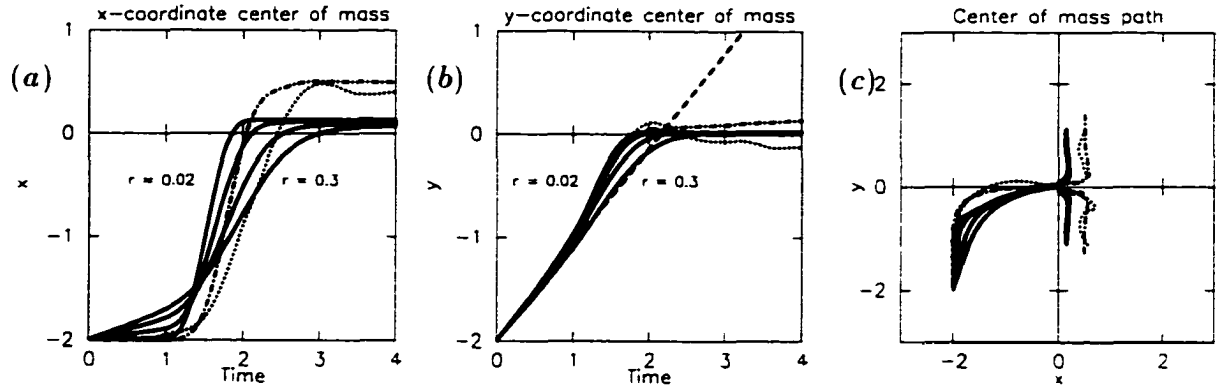


Figure 3.5: Centre of mass motion. Solid lines correspond to the FG model, $r = 0.02, 0.1, 0.2, 0.3$. Dash-dot lines: shallow-water, $Ro = 0.02$. Dotted lines: shallow-water, $Ro = 0.1$. Dashed line is the slope with which an eddy moving with the Nof (1983) speed would move.

We calculate the centre of mass of fluid in the domain at each time for the different runs performed, where the x - and y -coordinates of the centre of mass are

$$\bar{x} = \frac{\iint_{\Omega} x h dA}{\iint_{\Omega} h dA}, \quad \bar{y} = \frac{\iint_{\Omega} y h dA}{\iint_{\Omega} h dA},$$

respectively, where the integral is performed over the whole domain,

$$\Omega = \{(x, y) \mid |x| \leq 3, |y| \leq 3\}.$$

The evolution of the centre of mass with time is displayed in Figure 3.5. One may see from the \bar{x} versus time plot (Figure 3.5a) that for $r = 0.02$, the eddy propagates primarily along the shelf with almost no downhill motion, then suddenly accelerates in the downhill direction. For higher values of r , the downslope motion is greater initially, and the maximum downhill velocity is lower. For all the FG model runs, the fluid does not flow as high onto the opposite bank as for the shallow-water runs.

This further points to the lack of fluid inertia in the FG model. The \bar{y} versus time plot (Figure 3.5b) shows that the initial propagation speed along the shelf of all the runs agreed well with the Nof (1983) speed. To reveal the splitting of the fluid after passing the equatorial bottom of the channel, we compute three centres of mass: the overall centre of mass location, (\bar{x}, \bar{y}) (as already defined), the centre of mass of fluid in the northeastern quadrant of the domain,

$$\bar{x}_{NE} = \frac{\iint_{\Omega_1} x h dA}{\iint_{\Omega_1} h dA}, \quad \bar{y}_{NE} = \frac{\iint_{\Omega_1} y h dA}{\iint_{\Omega_1} h dA}, \quad \Omega_1 = \{(x, y) | 0 \leq x \leq 3, 0 \leq y \leq 3\}.$$

and the centre of mass of fluid in the southeastern quadrant,

$$\bar{x}_{SE} = \frac{\iint_{\Omega_2} x h dA}{\iint_{\Omega_2} h dA}, \quad \bar{y}_{SE} = \frac{\iint_{\Omega_2} y h dA}{\iint_{\Omega_2} h dA}, \quad \Omega_2 = \{(x, y) | 0 \leq x \leq 3, -3 \leq y \leq 0\}.$$

In the left half of the y versus x plot in Figure 3.5c, we display the centre of mass of the entire fluid (\bar{x}, \bar{y}) , but in the right half of the plot we display the centres of mass of fluid in the northeastern quadrant $(\bar{x}_{NE}, \bar{y}_{NE})$ and the southwestern quadrant $(\bar{x}_{SE}, \bar{y}_{SE})$ of the domain.

The plots in Figure 3.6 show diagnostics of the motion after the fluid has reached the bottom of the channel and split into northward and southward flowing parts. The motion predicted by the FG model is seen to be quite steady in time as compared with the shallow-water model. In the plot of centre of mass speed versus time (Figure 3.6b), the speed is scaled by the *local* Nof speed, $s(\bar{x}, \bar{y})/f(\bar{y})$ in nondimensional variables, where the slope $s(\bar{x}, \bar{y})$ and the Coriolis parameter $f(\bar{y})$ are each evaluated at the centre of mass position. The propagation speed in the shallow-water simulation

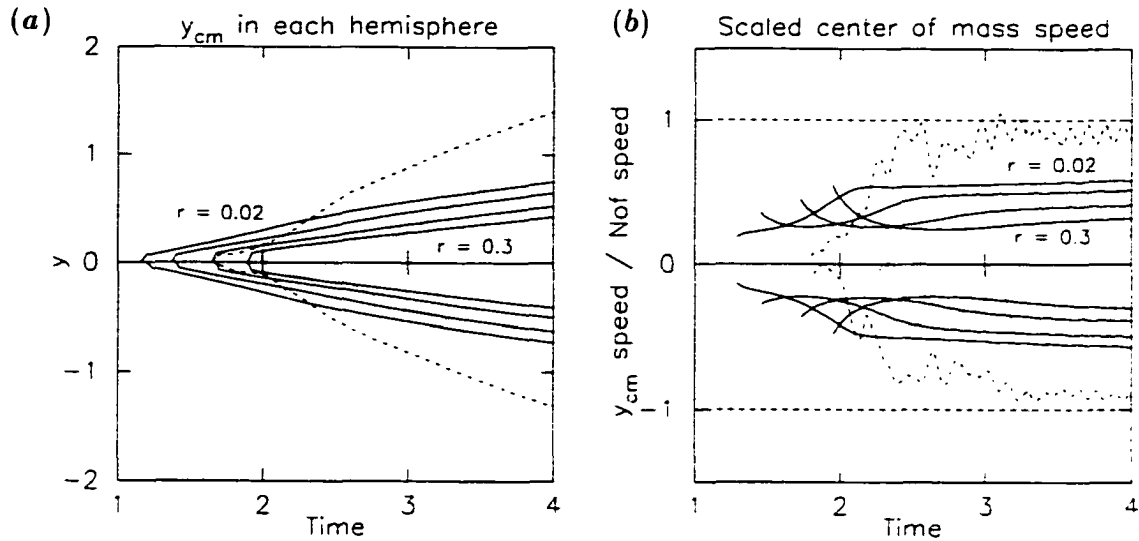


Figure 3.6: Motion after splitting. Solid lines correspond to the FG model, $r = 0.02, 0.1, 0.2, 0.3$. Dash-dot lines: shallow-water, $Ro = 0.02$. Dotted lines: shallow-water, $Ro = 0.1$. The propagation speed is scaled by the *local* Nof speed.

with low Rossby number is seen to agree well with the theoretical speed. The higher Rossby number flow is highly variable in time, and so it is difficult to say whether or not it moves with the predicted speed in the long-term time-mean case or not. The FG model predicts that the centre of mass of the flow propagates slower than the Nof speed for all damping parameters shown. This reflects the fact that the fluid is not in the form of northward- and southward-propagating isolated domes of fluid, but is instead spreading, with part of the fluid remaining stationary in the centre of the channel (see Figure 3.4. $t = 4.0$).

Figure 3.7 displays the fraction of the total fluid residing in either hemisphere for $x \geq 0$ as a function of time. The FG model seems to consistently predict a very symmetric north-south splitting of the current. The shallow-water model does

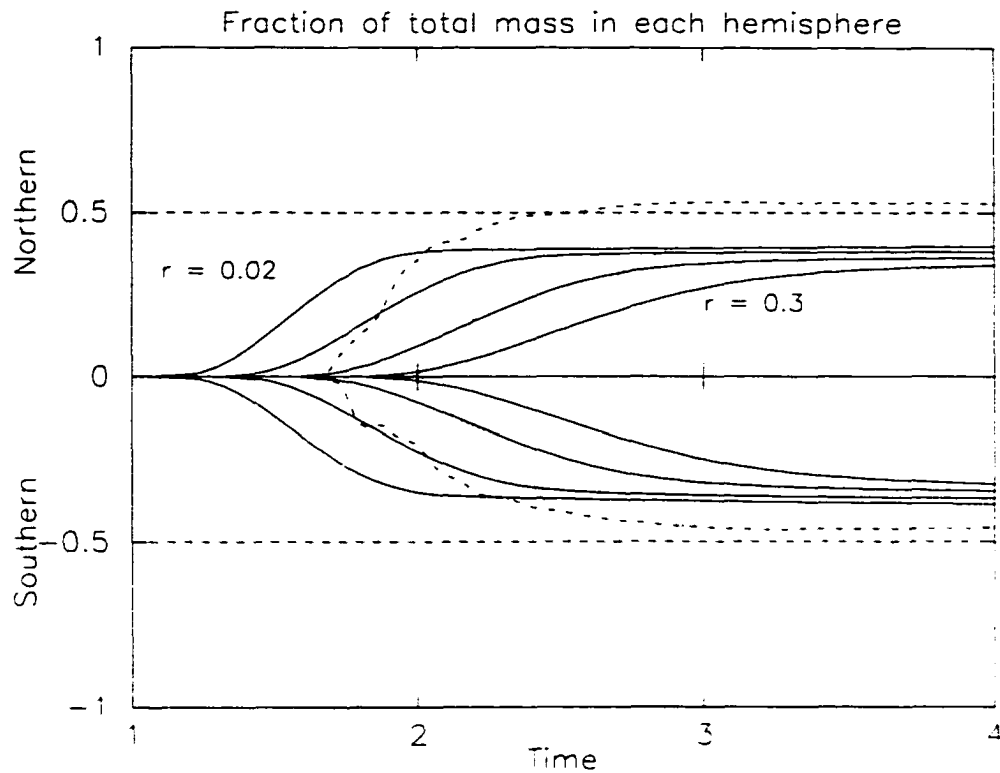


Figure 3.7: Amount of fluid in each hemisphere after splitting. Solid lines correspond to the FG model, $r = 0.02, 0.1, 0.2, 0.3$. Dash-dot lines: shallow-water, $Ro = 0.02$. Dotted lines: shallow-water, $Ro = 0.1$. The FG model predicts a symmetric splitting due to lack of fluid inertia in the model.

not predict a perfectly symmetric splitting. As documented by Borisov and Nof (1998), the amount of fluid ending up in either hemisphere is a complicated function of the channel geometry and the initial conditions of the eddy. For the particular simulations shown in Figure 3.7, the higher Rossby number flow has slightly more fluid recirculating south than flowing north, and vice versa for the lower Rossby number flow. The cause for this is likely related to the subtle differences in the speed and direction with which the eddy impinges upon the equator, which Borisov and Nof (1998) found to be the important factors determining how much fluid crossed the

equator.

The bottom topography of the Atlantic Ocean is certainly more complicated than that of a meridional channel (Figure 3.8). Although one may argue that the topography may reasonably be modelled as a meridional channel away from the equator, in the vicinity of the equator, the large-scale channel nature disappears, and the local topography is actually better approximated by an east-west channel, or a basin. Thus it remains to compare the predictions of these models over a realistic bottom topography.

3.5 Flow over realistic topography

The bottom topography of the Atlantic is shown in Figure 3.8. One detail of note is that the 4500 m contour does not cross the equator. So if, as observations seem to suggest, Antarctic Bottom Water flows at depths of approximately 4500 m, and yet successfully crosses the equator, then a certain amount of uphill flow is part of the current's path. If this is true, then the frictional geostrophic model studied here would have difficulty describing such a flow, since the model does not capture motions involving flow up the dynamic pressure gradient. We shall see that this is indeed the case.

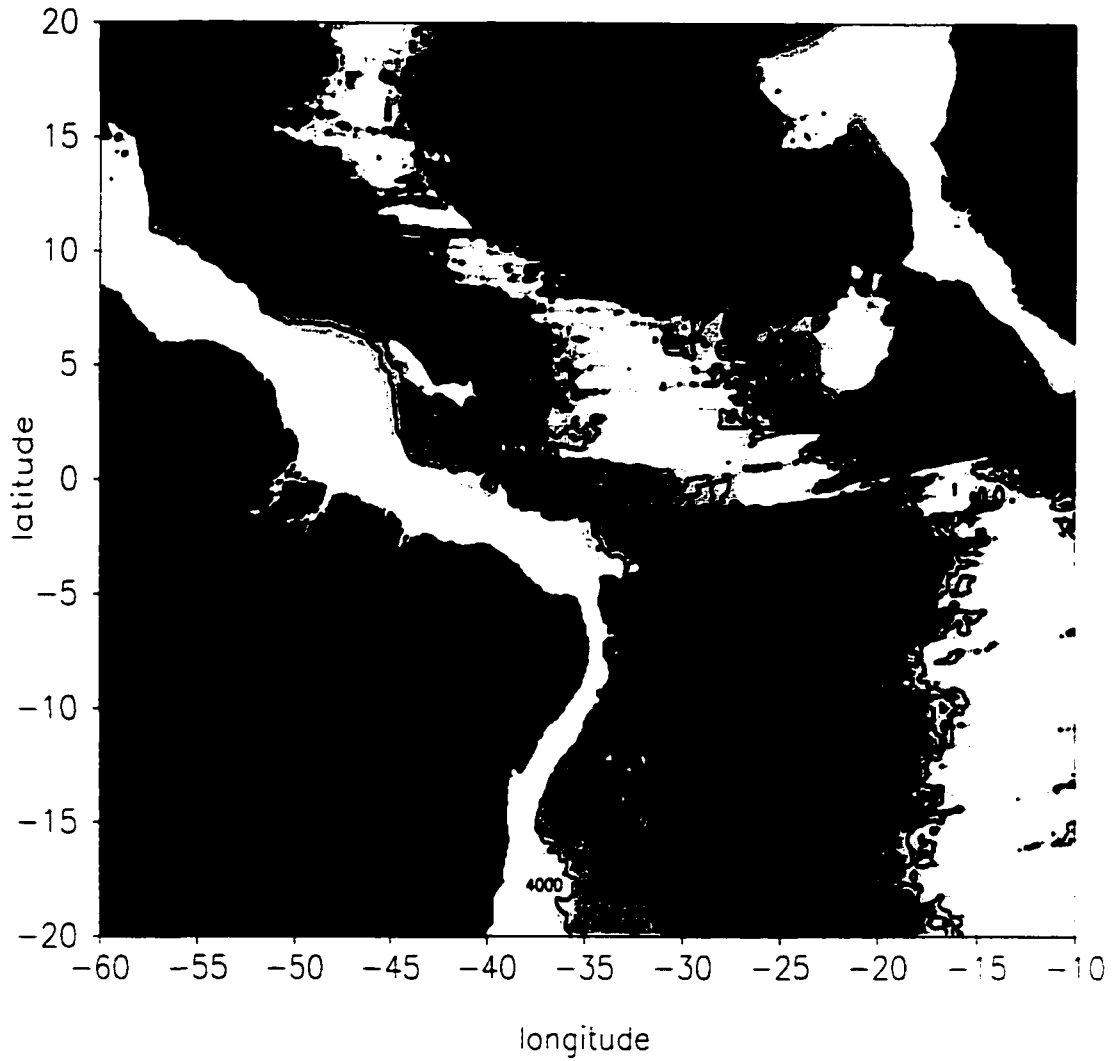


Figure 3.8: Bottom topography of the equatorial Atlantic. Contours of depths 4000 m, 4500 m, and 5000 m are shown. Bathymetric data is from the Naval Oceanographic Office Data Warehouse at <http://idbms.navo.navy.mil/>.

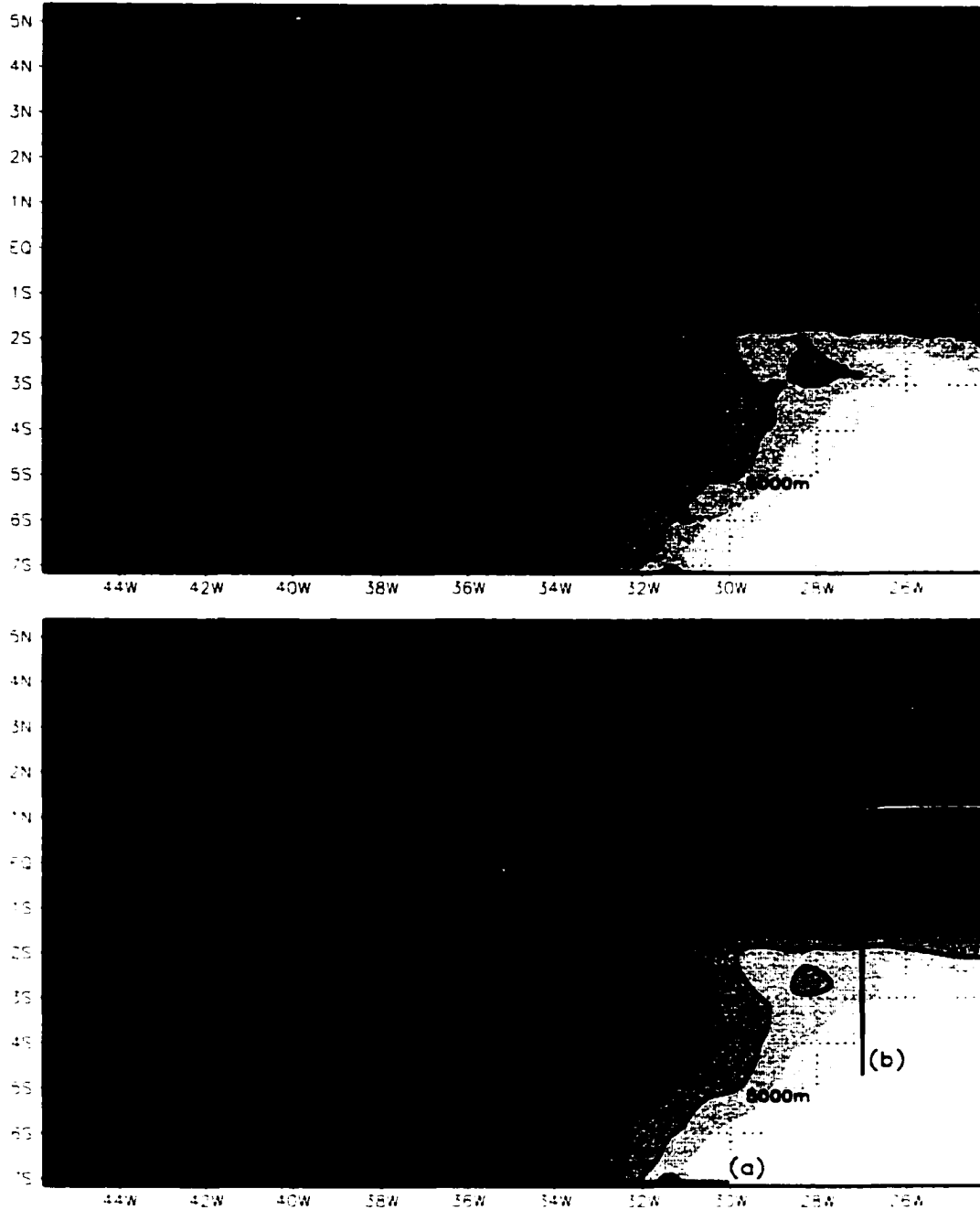


Figure 3.9: Bottom topography before and after smoothing. The smoothed topography is used in the numerical simulations. Shading interval is 200 m. Bathymetric data is from the Naval Oceanographic Office Data Warehouse at <http://idbms.navo.navy.mil/>. The six + signs mark the mooring locations of Hall *et al.* (1997). The five lines labelled (a)–(e) are the lines across which the flux is measured in our simulations.

3.5.1 Numerical scheme

To perform numerical simulations, we first smooth the bathymetry data to remove gridscale features. The bathymetric data is projected onto a 148 by 253 grid, and it is smoothed by six iterations of replacing a data point with the nine-point average of the data surrounding it. This averaging was judged by eye to be a reasonable compromise between removing gridscale features and retaining large-scale features of the topography. The raw topographic data and the smoothed topography is shown for the actual numerical domain in Figure 3.9.

The inflow conditions are specified via Dirichlet boundary conditions on the height and velocity fields. The height at the boundary is set to have a cosine profile.

$$h = \frac{h_{\max}}{2} \left[1 + \cos \left(\frac{\pi R}{R_{\max}} \right) \right], \quad 0 \leq R \leq R_{\max}.$$

where $R = |x - x_c|$ and x_c , h_{\max} and R_{\max} are specified parameters corresponding to the centre, height and the half-width of the inflow profile, respectively. This height profile was chosen so that the height field is continuous and differentiable, to assist with numerical stability. The influx velocity is calculated from the height profile on the boundary, assuming the flow is geostrophic. Unless otherwise specified, the inflow has a height of 0.7 (280 metres) and a half-width of 0.5 (100 km). Outflow conditions are crudely set by providing a mass sink along the northern and eastern edges of the domain. The mass sink decreases the height field, with factors that decrease smoothly from exactly one over most of the domain to zero right near the edge of the domain.

The velocity scale has been taken to be 5 cm s^{-1} , the Coriolis parameter has been

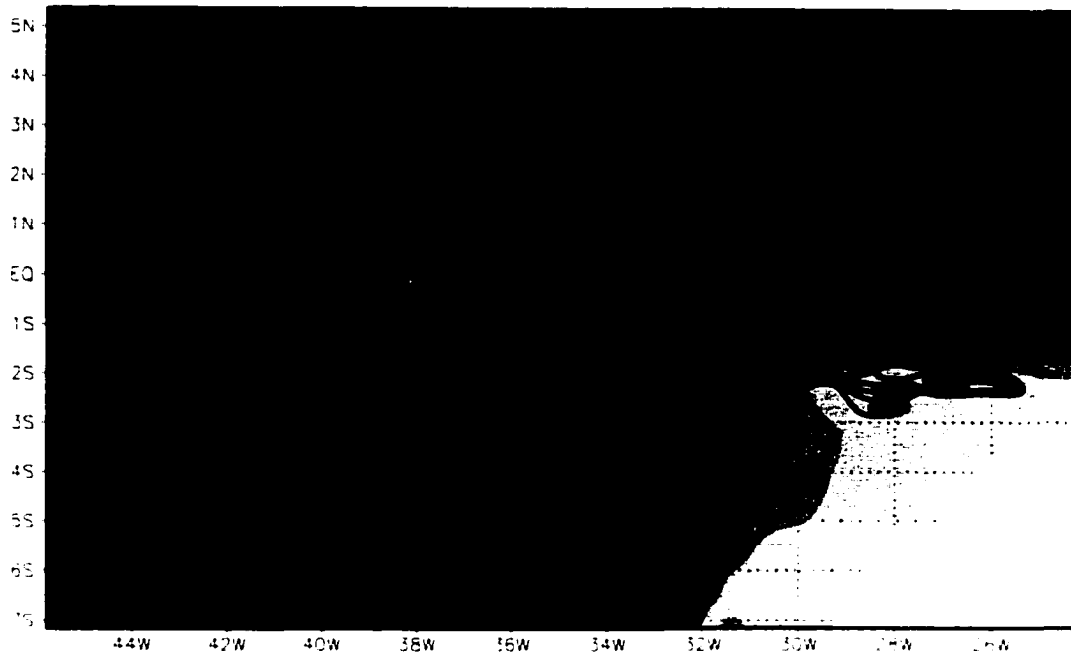


Figure 3.10: Height field at steady state, shallow-water model. Contour interval is 0.1, or 20 metres.

scaled by its value at 5°N , and the horizontal length scale is 200 km. This gives a Rossby number (at 5°N or 5°S) of $Ro = 0.0197$, and a time scale of $T = 46.3$ days, i.e. 1 year is 7.88 nondimensional time units. The spatial variation of the Coriolis parameter is $f = \sin \theta / \sin 5^\circ$, where θ is latitude.

3.5.2 Steady-state results

The shallow-water model and the frictional geostrophic model were run to steady state. Steady state was determined to have been reached when the output diagnostic values of potential and kinetic energy approached steady values. (Typically, at steady state the diagnostic variables were varying by less than 1% of their value over one

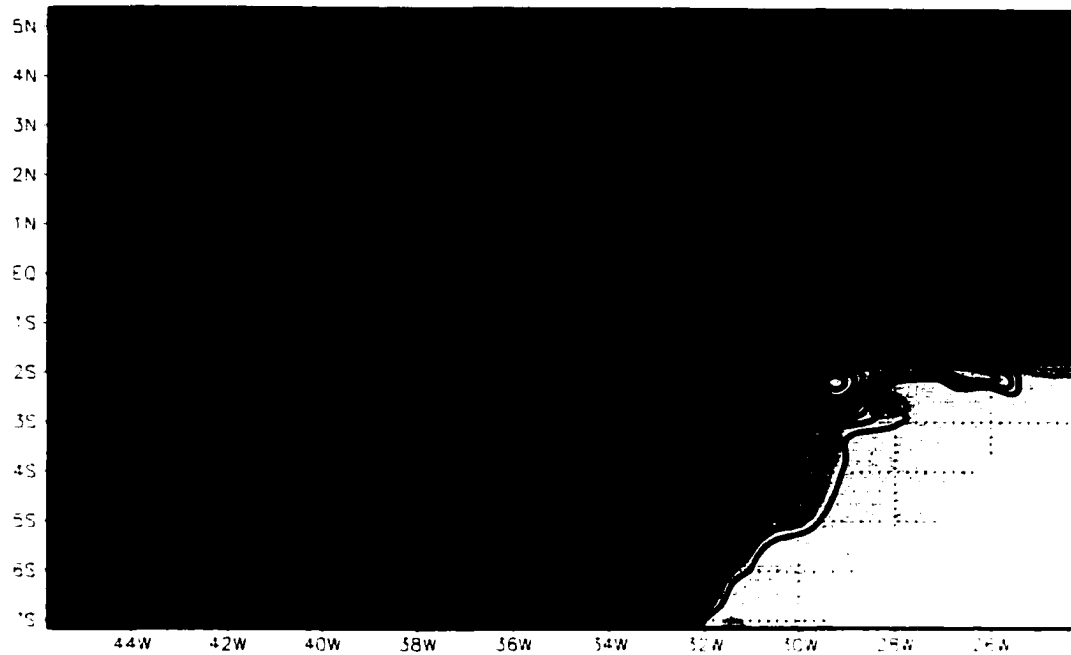


Figure 3.11: Height field near steady state, FG model. Contour interval is 0.1, or 20 metres.

nondimensional time unit.) An image of the resulting height field for each run, with identical influx conditions, is shown in each of Figures 3.10 and 3.11. Note that Figure 3.11 shows the system when it is not quite at steady state, since the equatorial basin is still filling slowly. However, the height field east of 34°W is already as it appears at steady state.

For both models, the flow is observed to follow bathymetric contours quite closely. While the entire current initially flows northward along the contours, part of the flow turns north-west and enters the equatorial basin, which is located between 1°S and 1°N and between 34°W and 38°W, and part of the flow turns east and exits the numerical domain. However, the frictional geostrophic model predicts much less flow into the equatorial basin, and ultimately, across the equator.

Line label	Description	Location	Direction	Range
(a)	into domain	7°S	North	35°W–30°W
(b)	out of domain	25°W	East	3°S–0.5°S
(c)	into eq. basin	33.7°W	West	4°S–0.2°S
(d)	HMW moorings	35.9°W	West	2°S–1°N
(e)	out of eq. basin	39.2°W	West	0.8°S–1.3°N

Table 3.1: Lines across which the flux is calculated in the simulations.

The mass transport of this current is measured for each of these simulations across five locations (see Figure 3.9 and Table 3.1). The measured fluxes are (a) the flow into the domain, (b) the flow eastward out of the domain, (c) the flux into the equatorial basin, (d) the flux across the mooring locations of Hall *et al.* (1997), and (e) the flux out of the equatorial basin.

For the simulations shown in Figures 3.10 and 3.11, the shallow-water model predicts a 0.115 Sv flux across the equator, but the frictional geostrophic model predicts only a flow of 0.024 Sv across the equator. Since uphill flow is not permitted in the FG model, the only fluid successfully crossing the equator is fluid that was initially at shallow enough depths to flow over the ridges located before and after the equatorial basin.

If this hypothesis is true, then the equator-crossing flux predicted by the FG model should therefore sensitively depend upon influx position. The influx position was varied, and the flux across the equator measured at steady state, with the results

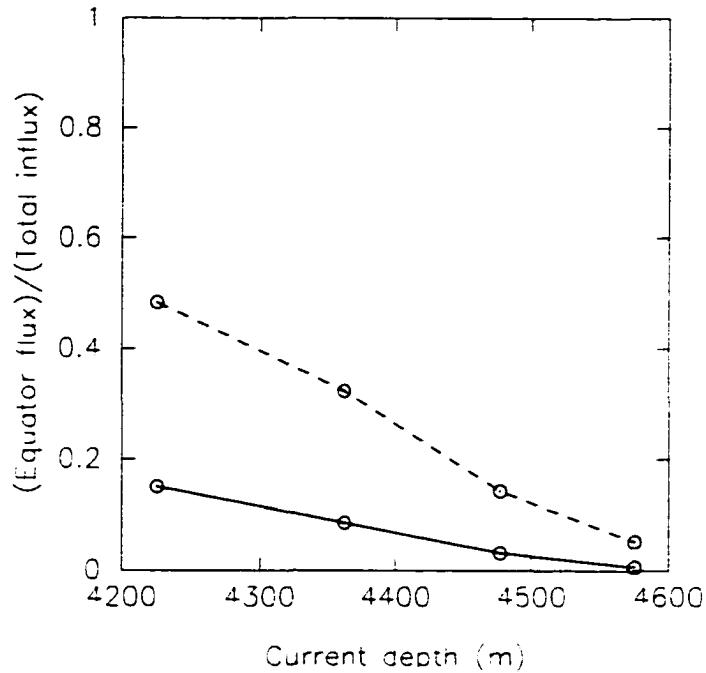


Figure 3.12: Flux across equator as a function of inflow position. Dotted line corresponds to shallow-water simulations, solid line to FG model.

shown in Figure (3.12). For this figure, the depth of the current is the position relative to the ocean surface of the centre of mass of the influx profile, as calculated by numerically integrating over the region of inflow for each of the different current locations. For both models, the equator-crossing flux depends on the initial depth of the current, with the frictional geostrophic model consistently predicting less equator-crossing flow than the shallow-water model at the same initial current position.

It is worth noting that we have not observed, no matter how shallow the inflow depth, the entire current crossing the equator. Sandoval and Weatherly (2001) propose that the AABW splits up into two currents: the shallower one, which flows with 1.1 Sv flux at 4.5°S at a depth of 4400 to 4500 m, flows directly into the equatorial

basin, eventually crossing the equator.¹ Since we have not observed more than 50% of the current flowing into the equatorial basin in our numerical simulations, even for current depths much more shallow than oceanic observations suggest, we propose that only part of this observed shallower current flows into the equatorial basin.

Note that for realistic inflow depths, the shallow-water model captures the observed southern-intensified western flow within the equatorial basin. (See Hall *et al.* 1997 for observations, Figure 3.13 for our simulations.) However, for inflow higher up on the topography, the resulting flow is observed to circulate the opposite way in the equatorial basin, and is seen to be much more variable in time. (It has not been observed to settle to a steady state.) This alternate flow appears to be the result of a small amount of fluid that flows through the gap in the ridge near (4°S, 34°W), and, as it enters the equatorial basin, interacts with the remaining flow, diverting it northward and establishing a counterclockwise flow in the basin.

Since the downhill component of flow in the FG model also depends upon the damping coefficient, that coefficient should also affect the amount of current crossing the equator. The damping parameter was varied, and the percentage flux crossing the equator measured at steady state. The results are shown in Figure 3.14. An increase in the damping parameter leads to a decrease in the amount of fluid crossing the equator. The damping parameter is set to $r = 0.05$ for most simulations since

¹The discrepancy in measured fluxes near 5°S and across the equator (2.1 Sv, Hall *et al.* 1997) may be due to entrainment effects or to measurement errors due to large variability. For example, the best estimates (Sandoval and Weatherly 2001) of the transport in this current at 13°S is 3.8 Sv.

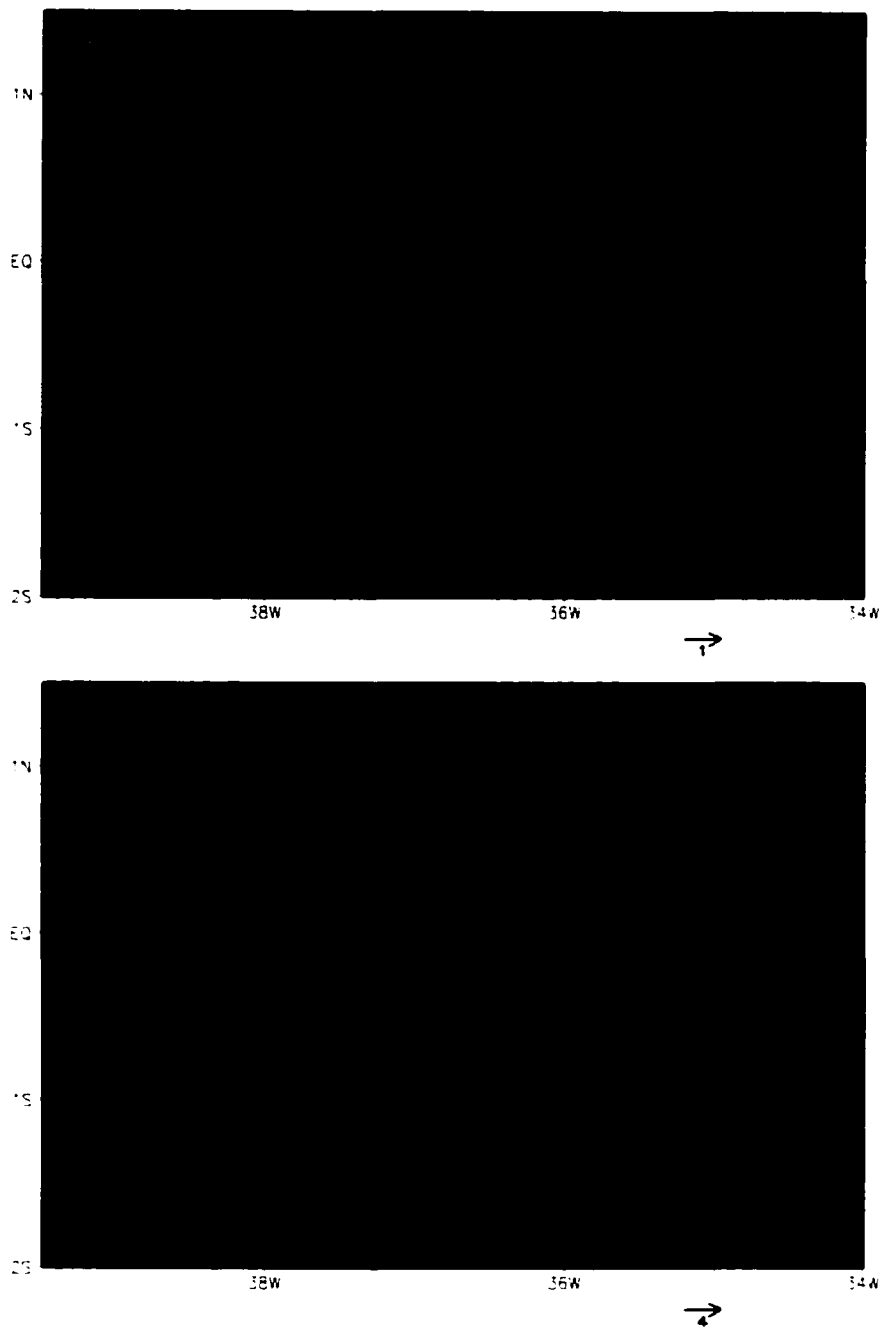


Figure 3.13: Velocity fields in the equatorial basin for realistic and very shallow inflow. Upper plot: inflow depth = 4575 m. arrow at bottom is for 5 cm s⁻¹. Lower plot: inflow depth = 4226 m. arrow at bottom is for 20 cm s⁻¹.

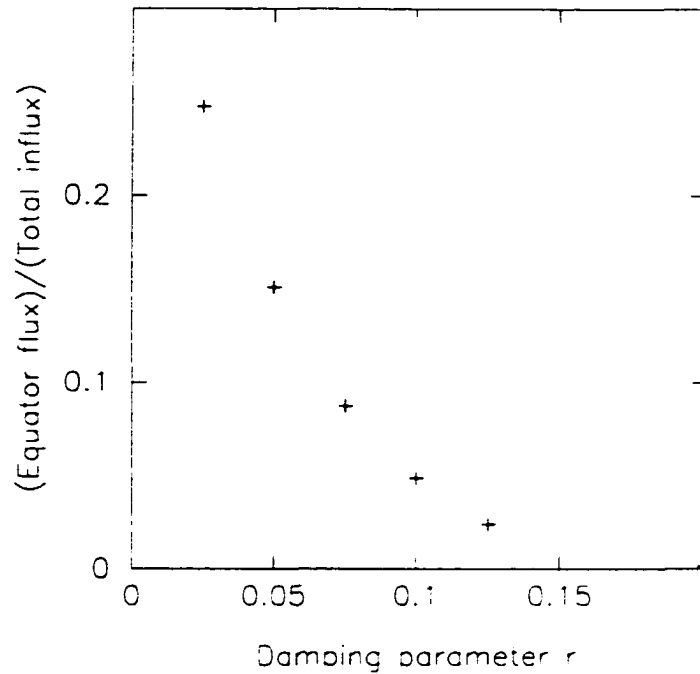


Figure 3.14: Percentage flux across equator as a function of damping parameter.

the velocity at $f = 0$ is proportional to $1/r$ (see equation 3.9). so smaller damping parameters lead to unreasonably high velocities at the equator, causing numerical instability unless the time step is quite small.

3.5.3 Time-dependent flow

Hall *et al.* (1997) (hereafter referred to as HMW) measured a mean equator crossing flux of about 2.0 Sv, but also observed a significant time variability in the AABW flow in the equatorial basin. In Figure 3.15, we display their figure showing the measured transport of Antarctic Bottom Water across the equator as a function of time. They measured changes in the observed transport on the order of 4 Sv in a few

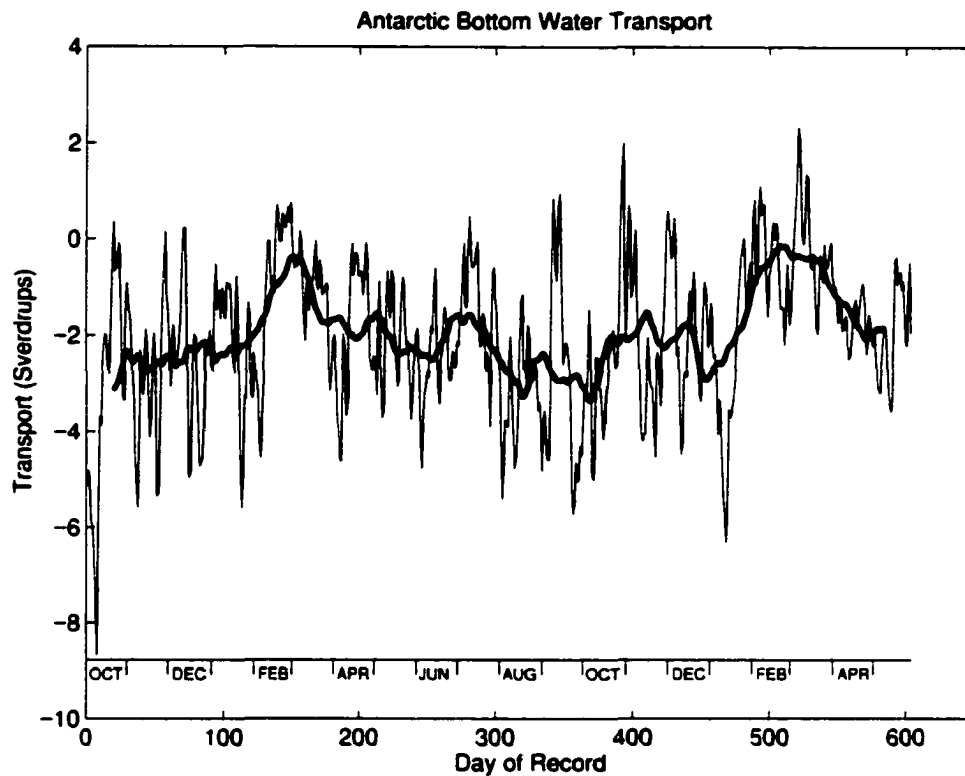


Figure 3.15: Time-dependent flux as measured by HMW. Thin line: daily transport. Thick line: 40-day boxcar average. Negative values indicate northward flow. Reproduced with permission of the journal publishers.

days, varying from as much as 5 Sv northward to 2 Sv southward over the 604 day dataset. Perhaps most significantly, they observed that the 40-day averaged transport was slightly greater than 2 Sv northward for much of the year, but was close to zero at the same time of year (beginning of March) two years in a row. This implies that the AABW has an annual signal associated with it, with magnitude on the order of the total volume flux itself.

To evaluate the ability of the shallow-water model and the frictional geostrophic model to capture this time variability, simulations were performed with time-varying inflow conditions, and the flux was measured as a function of time across the five key positions. The model was first run out to steady state, then the inflow was varied sinusoidally in time, with a period of one year and an amplitude of 10 percent. The results are shown in Figures 3.16 and 3.17.

Figure 3.16 shows the five measured fluxes as they vary in time. Although the magnitude of the inflow was varied by only 10%, the response of the measured fluxes was significantly greater. As a result of the time-varying inflow conditions, the flow into the equatorial basin actually reversed direction for a brief period of time, while the flow that actually crossed the equator changed its volume flux by 17% of its mean value. Most significantly, the time variability of the fluid across the position where HMW took their data shows a relative change of 75% of its mean value. The difference in time variability of the fluid at the mooring locations and at the exit of the equatorial basin is easily explained by the fact that much of the extra fluid

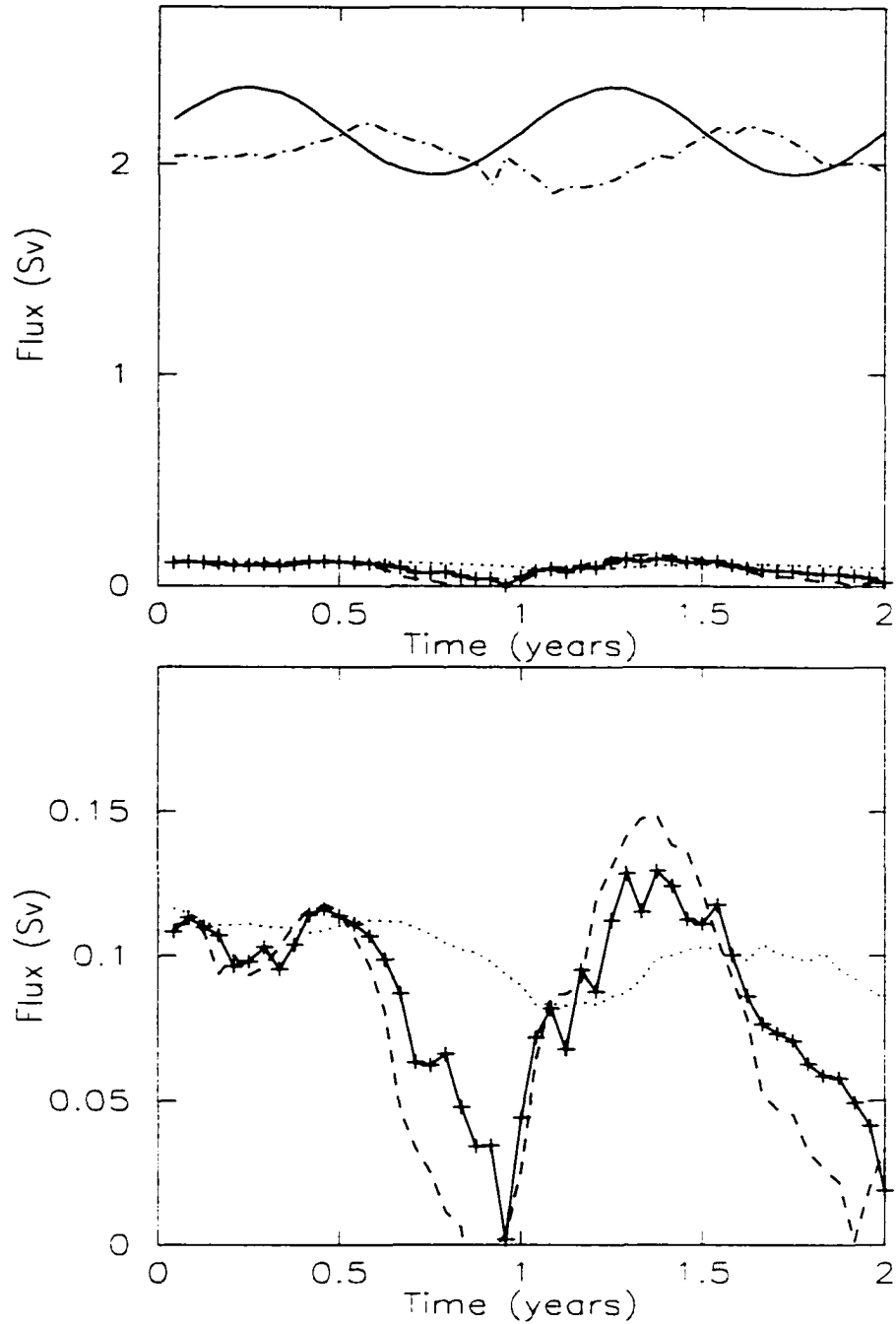


Figure 3.16: Time-dependent flux as predicted by shallow-water theory. inflow position of $x_c = 1.25$. Solid line: inflow conditions. Dash-dot: outflow eastward. Dashed line: flow into equatorial basin. Dotted line: flow out of equatorial basin. Solid with +: flow across HMW mooring locations. Bottom plot is shown with limited axis range to show time variability.

entering the basin simply filled it, and did not exit.

These results imply that the time variability observed by HMW is a result of the local topography and of the location of the current meters, and does not reflect the amount of time variability of the amount of fluid crossing the equator, nor the time variability of the AABW current as it approaches the equatorial basin.

The same experiment was conducted with the frictional geostrophic model, with the results shown in Figure 3.17. Although this model does display less time-variability than the shallow-water model, it still predicts that a 10% change in flux approaching the equatorial basin leads to larger relative changes in flux into and through the basin. The flow into the equatorial basin varied by 44% of its mean value, while the flow across the HMW mooring locations varied by 25%. The flow out of the equatorial basin varied by 9.4% of its mean.

To investigate how the time-dependent behaviour seen in Figure 3.16 depends on inflow location, we performed the same experiment as in Figure 3.16, but with the current inflow set to a nondimensional position of 1.15 (centre of mass at 4477 m depth) instead of 1.25 (centre of mass at 4575 m depth). The centre of mass of the current at the southern boundary is thus at a depth consistent with observations. The results are shown in Figure 3.18. The amplitudes of the fluctuations in and through the equatorial basin are not quite as great as for the deeper current case. Also, the crests and troughs seem more symmetric in this shallower current experiment than in the deeper current experiment, where the asymmetry is similar to the asymmetry

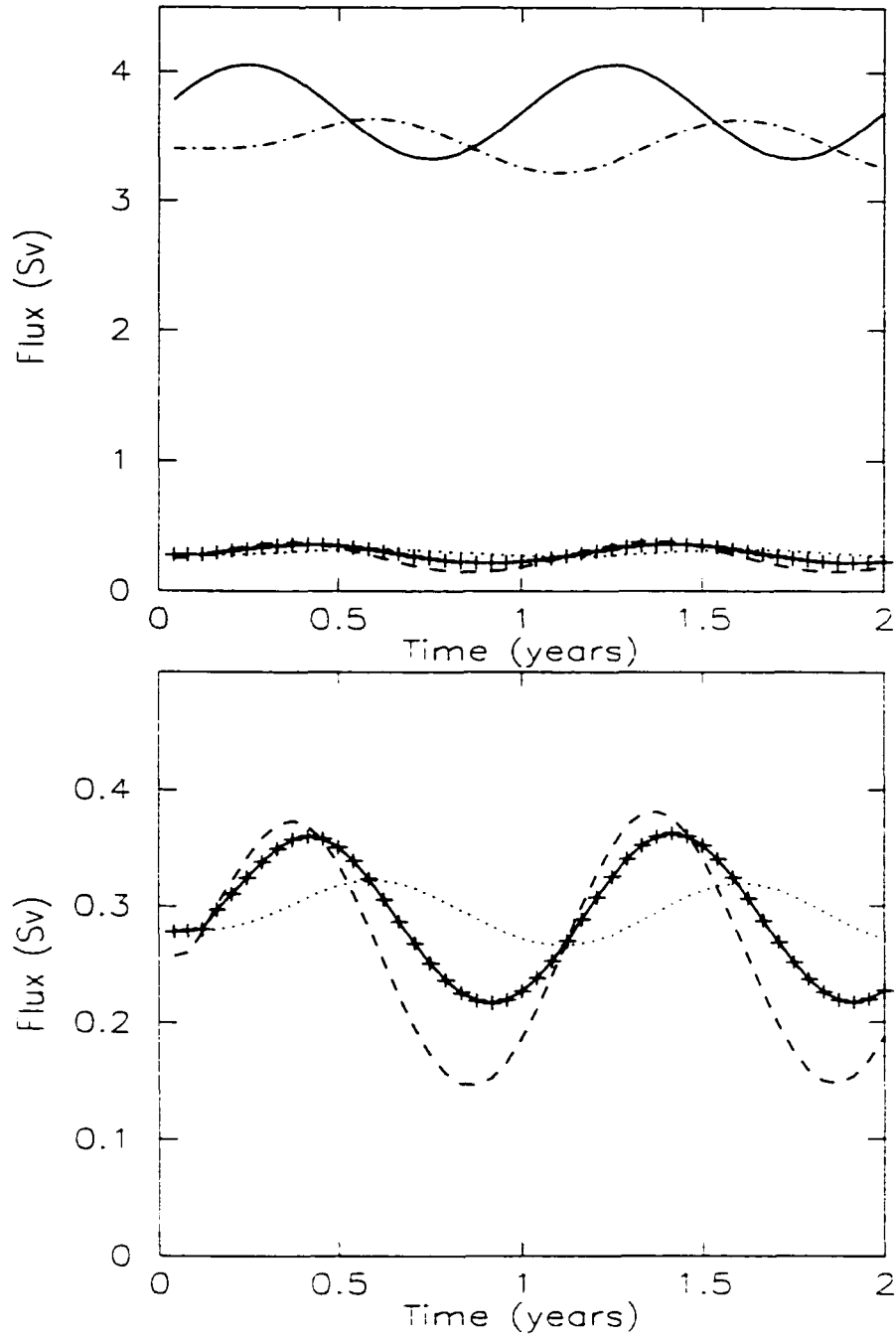


Figure 3.17: Time-dependent flux as predicted by FG model. Solid line: inflow conditions. Dash-dot: outflow eastward. Dashed line: flow into equatorial basin. Dotted line: flow out of equatorial basin. Solid with +: flow across HMW mooring locations. Bottom plot is shown with limited axis range to show time variability.

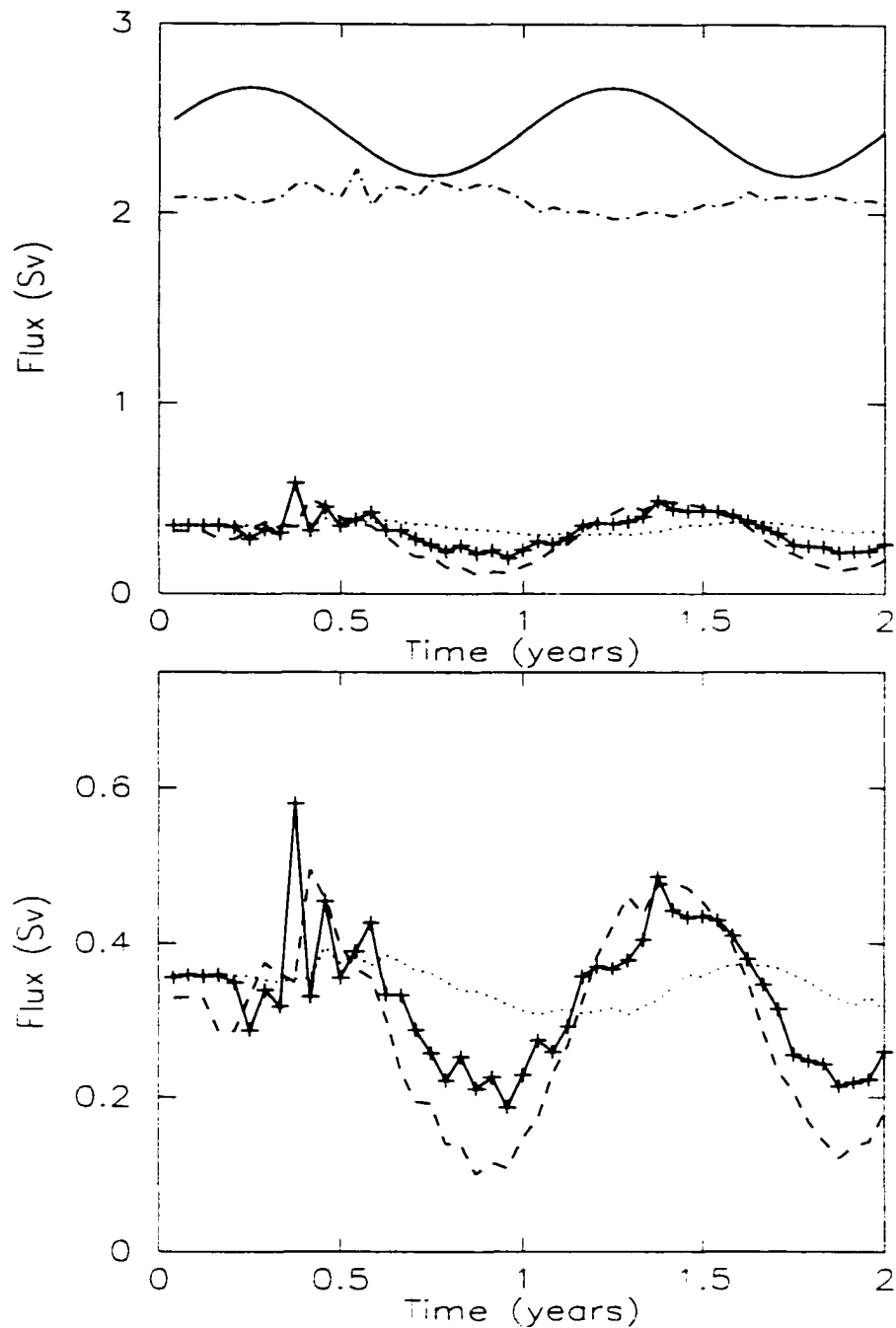


Figure 3.18: Time-dependent flux as predicted by shallow-water theory, inflow position of $x_c = 1.15$. Solid line: inflow conditions. Dash-dot: outflow eastward. Dashed line: flow into equatorial basin. Dotted line: flow out of equatorial basin. Solid with +: flow across HMW mooring locations. Bottom plot is shown with limited axis range to show time variability.

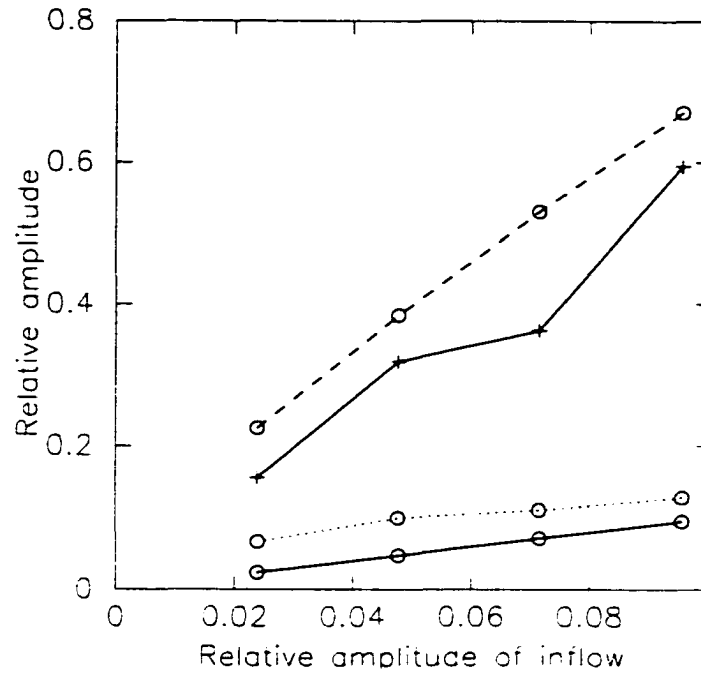


Figure 3.19: Amplitude of time-dependent fluxes versus amplitude of time-dependent inflow condition, shallow-water simulations. Inflow position, $x_c = 1.15$. Solid line with circles: inflow conditions. Dashed line with circles: flow into equatorial basin. Dotted line with circles: flow out of equatorial basin. Solid line with +: flow across HMW mooring locations.

seen in the observations (Figure 3.15).

In the experiment shown in Figure 3.18, the inflow was varied by 10% over the course of one year. The same experiment was repeated, but with inflow variations of 7.5%, 5%, and 2.5%, and the results are summarized in Figure 3.19. The experiments were run for two simulated years, and each of the transports was averaged over the two years. We compute the “relative amplitude” of time variability as

$$\text{relative amplitude} = \frac{0.5(\text{max. transport} - \text{min. transport})}{\text{average transport}}$$

This is a simple measure of how much the transport deviates from its average. If the transport were a sinusoidal function of time, the numerator would be the crest-

to-average amplitude. We plot the relative amplitude in Figure 3.19 as a measure of how much the relative time-variation of transport across each of the locations depends on the relative time-variation of transport as AABW approaches the equator. The amount of fluid successfully crossing the equator is seen to show slight amplification of time-variability, but the amount of fluid flowing into the equatorial basin and also across the HMW mooring locations shows large amplification of time-variability.

These results suggest that the large time-variability in cross-equatorial transport observed by HMW may be the result of variations in the source of AABW on the order of merely 10% to 15% of its mean transport. These results also suggest that the amount of fluid successfully crossing the equator (i.e. exiting the equatorial basin) does not have the same amplitude of time-variability as was measured by HMW, but has a smaller amplitude of approximately 10% to 20% of the mean flow.

The model studied here parameterizes frictional and other ageostrophic effects into a simple Rayleigh damping term. This model has been used in studies of large-scale flow, including abyssal equator-crossing flow. We have investigated the viability of this model by comparing its predictions to the predictions of shallow-water theory over simplified and realistic topography. Despite the simplicity of the model, it broadly captures certain aspects of shallow-water flow well.

Although the model studied in this chapter is a candidate for the lower layer of the two layer model we are constructing, it is not a reasonable model for the upper layer because the thick upper layer would not have bottom friction playing a leading-order

role in the dynamics. In the next chapter, we will explore two-layer models.

Chapter 4

Two-layer model

In this chapter, the effect of a dynamically active upper layer is considered. Leading-order two-layer models are derived for a mid-latitude scaling as well as an equatorial scaling. In the mid-latitude scaling, the shallow-water equations or the frictional geostrophic model studied in the previous chapter may be employed in the lower layer, and in the upper layer a relation is derived that resembles the balance equations (Gent and McWilliams 1983). A model is thus derived that, while predicting a well-defined flow at the equator, simplifies to the Swaters and Flierl (1991) model in the mid-latitude limit. In the equatorial scaling, we obtain two models, corresponding to two different mechanisms for inducing motion in the upper layer. In one of the equatorial models, the lower layer dynamics are governed by the shallow-water equations, and the upper layer dynamical equations are shown to be related to the linearized shallow-water equations. Thus, the equatorial wave analysis of Chapter 2 applies to that

equatorial scaling model. Finally, the three models are merged into one leading-order uniformly valid model which reduces in each of the limits to the appropriate local model.

We first present a modified Nof (1983) analysis to help motivate the need for an upper layer.

4.1 Modified Nof analysis

Nof (1983) showed that the velocity of any steadily-travelling compactly-supported mass of inviscid shallow water on a linearly sloping bottom on an f -plane is along the slope with speed $g's/f$, where g' is the reduced gravity, s is the slope of the bottom topography, and f is the Coriolis parameter. Swaters and Flierl (1991) modified Nof's analysis to include the effects of baroclinic interactions with the upper layer on the velocity. Here, we extend the analysis further to include the effects of bottom friction as parameterized by a linear damping term.

The equations of motion for the lower layer, including the effects of variation in pressure of the upper layer and linear damping, may be written

$$\mathbf{u}_t + \mathbf{u} \cdot \nabla \mathbf{u} + f \hat{\mathbf{e}}_3 \times \mathbf{u} + g' \nabla (h - sy) + g \nabla \eta = -r \mathbf{u}, \quad (4.1)$$

$$h_t + \nabla \cdot (\mathbf{u} h) = 0, \quad (4.2)$$

where we have assumed the bottom topography is linearly sloping, deepening in the positive y direction, and we have applied the rigid lid approximation. We assume

that the region of non-zero height has compact support, i.e. that the fluid occupies a local region only. Denote the region of non-zero height by R and let the boundary of the region, ∂R , be given by $\phi(x, y, t) = 0$. On ∂R , the following boundary conditions apply:

$$\phi_t + \mathbf{u} \cdot \nabla \phi = 0 \quad \text{and} \quad h = 0. \quad (4.3)$$

What is the speed at which this eddy travels at steady-state? We assume the dome of fluid is steadily travelling with velocity $\mathbf{c} = (c_x, c_y)$, and re-write the equations in the co-moving frame of reference. Let

$$\xi = x - c_x t, \quad \zeta = y - c_y t. \quad (4.4)$$

define the moving coordinates. Then the equations and boundary conditions in the moving frame of reference are

$$(\mathbf{u} - \mathbf{c}) \cdot \nabla \mathbf{u} + f \hat{\mathbf{e}}_3 \times \mathbf{u} + g' \nabla (h - sy) + g \nabla \eta = -r \mathbf{u}. \quad (4.5)$$

$$\nabla \cdot [(\mathbf{u} - \mathbf{c})h] = 0. \quad (4.6)$$

$$(\mathbf{u} - \mathbf{c}) \cdot \nabla \phi = 0, \quad \text{on} \quad \phi(\xi, \zeta) = 0. \quad (4.7)$$

where we have used $\nabla \cdot \mathbf{c} = 0$. We may determine the steady speed \mathbf{c} by multiplying (4.5) by h and integrating over R , yielding

$$\int_R \{h(\mathbf{u} - \mathbf{c}) \cdot \nabla \mathbf{u} + hf \hat{\mathbf{e}}_3 \times \mathbf{u} + hg' \nabla (h - sy) + hg \nabla \eta + hr \mathbf{u}\} dA = \mathbf{0}. \quad (4.8)$$

Let us simplify this equation term-by-term. Note that the nonlinear advection term vanishes, since

$$\int_R h(\mathbf{u} - \mathbf{c}) \cdot \nabla \mathbf{u} dA = \int_{\partial R} [h(\mathbf{u} - \mathbf{c}) \cdot \hat{\mathbf{n}}] \mathbf{u} dl - \int_R \nabla \cdot [h(\mathbf{u} - \mathbf{c})] \mathbf{u} dA = \mathbf{0}.$$

The term proportional to g' may also be simplified as follows:

$$\int_R g' h \nabla(h - sy) dA = -\hat{e}_2 g' s \int_R h dA + \frac{g'}{2} \int_R \nabla(h^2) dA = -\hat{e}_2 g' s \int_R h dA.$$

To simplify the second and fifth terms in (4.8), note that the fact that the mass flux in the moving frame is nondivergent (4.6) implies that there exists a function ψ such that $\hat{e}_3 \times \nabla \psi = (\mathbf{u} - \mathbf{c})h$. Thus,

$$\begin{aligned} \int_R \mathbf{u} h dA &= \int_R \mathbf{c} h dA + \int_R \hat{e}_3 \times \nabla \psi dA \\ &= \mathbf{c} \int_R h dA + \hat{e}_3 \times \int_{\partial R} \psi \hat{\mathbf{n}} dl \\ &= \mathbf{c} \int_R h dA. \end{aligned}$$

where the second integral vanishes because ψ is constant on ∂R , which is true since on $\phi = 0$, $0 = h(\mathbf{u} - \mathbf{c}) \cdot \nabla \phi = (\hat{e}_3 \times \nabla \psi) \cdot \nabla \phi = J(\psi, \phi)$. Using this in (4.8) simplifies it to

$$f \hat{e}_3 \times \mathbf{c} + r \mathbf{c} = g' s \hat{e}_2 - g \langle h \nabla \eta \rangle.$$

where $\langle (*) \rangle = \int_R (*) dA / \int_R h dA$. The translation velocity \mathbf{c} may be solved for.

$$\mathbf{c} = \frac{r}{r^2 + f^2} \{g' s \hat{e}_2 - g \langle h \nabla \eta \rangle\} + \frac{f}{r^2 + f^2} \{g' s \hat{e}_1 + g \hat{e}_3 \times \langle h \nabla \eta \rangle\}. \quad (4.9)$$

or, componentwise,

$$c_x = \frac{f \{g' s - g \langle h \eta_y \rangle\} - r g \langle h \eta_x \rangle}{f^2 + r^2}. \quad (4.10)$$

$$c_y = \frac{f g \langle h \eta_x \rangle + r \{g' s - g \langle h \eta_y \rangle\}}{f^2 + r^2}. \quad (4.11)$$

Equation (4.9), or the pair (4.10) and (4.11), is the Nof (1983) velocity modified to include the effects of upper layer pressure and lower layer friction.

Some special cases may be investigated. In the limit as $\eta \rightarrow 0$ and $r \rightarrow 0$, equation (4.9) reduces to the Nof (1983) result describing along-slope motion with velocity $g's/f$. If only $r \rightarrow 0$, (4.9) reduces to the Swaters and Flierl (1991) result in which the Nof velocity is modified to include the effects of the upper layer pressure.

$$c_x = \frac{g's}{f} - \frac{g}{f}\langle h\eta_y \rangle, \quad c_y = \frac{g}{f}\langle h\eta_x \rangle.$$

In the limit as $\eta \rightarrow 0$ with $r > 0$, (4.9) recovers the fact that friction in the one-layer frictional geostrophic model induces a downslope component to the flow.

$$\mathbf{c} = \frac{g's}{r^2 + f^2}(r\hat{\mathbf{e}}_2 + f\hat{\mathbf{e}}_1).$$

Note that an alternate derivation may be used to arrive at this result. The alternate derivation requires the assumption that a fluid parcel is moving along a slope in such a way that there exists a three-way balance between the forces of gravity, Rayleigh friction, and the Coriolis effect. Since such a derivation may be applied to any fluid parcel in such a balance, the result generalizes to currents in balance in addition to steady-travelling eddies.

Clearly, the presence of a dynamically active upper layer modifies the direction of flow of the lower layer. In particular, note that it is possible for the lower layer to have an upslope component to the velocity field.

4.2 Generic nondimensionalization

We seek to model abyssal flow, taking into account interactions with the fluid above. From the outset, then, we anticipate that the lower layer is relatively thin and the upper layer is thick. This implies that, while bottom friction is potentially important in the lower layer, it may be neglected in the upper layer. Thus, our starting point is two-layer shallow-water equations, where the upper layer is frictionless and the lower layer retains a Rayleigh damping term representing the effects of bottom friction.

The two-layer shallow-water equations may be written in dimensional form as

$$\mathbf{u}_1^*{}_{,t^*} + \mathbf{u}_1^* \cdot \nabla^* \mathbf{u}_1^* + f^* \hat{\mathbf{e}}_3 \times \mathbf{u}_1^* = -g \nabla^* \eta^* \quad (4.12)$$

$$(\eta^* - h^*)_{,t^*} + \nabla^* \cdot [\mathbf{u}_1^* (H + \eta^* - h^* - h_B^*)] = 0 \quad (4.13)$$

$$\mathbf{u}_2^*{}_{,t^*} + \mathbf{u}_2^* \cdot \nabla^* \mathbf{u}_2^* + f^* \hat{\mathbf{e}}_3 \times \mathbf{u}_2^* = -\frac{1}{\rho_2} \nabla^* p^* - r^* \mathbf{u}_2^* \quad (4.14)$$

$$h_{,t^*}^* + \nabla^* \cdot (\mathbf{u}_2^* h^*) = 0, \quad (4.15)$$

where an asterisk denotes a dimensional variable. The upper and lower layer velocities are denoted by \mathbf{u}_1 and \mathbf{u}_2 respectively. H is the scale depth of the upper layer, h is the lower layer thickness, h_B is the height of the bottom topography above an arbitrary reference level, η is the upper layer pressure and the lower layer pressure p^* is given by

$$p^* = \rho_1 g \eta^* + \rho_2 g' (h^* + h_B^*), \quad (4.16)$$

where $g' = g(\rho_2 - \rho_1)/\rho_2$ is the reduced gravity. The form of the upper and lower layer pressure terms is such that the pressure vanishes at the upper layer surface and

the pressure is continuous across the interface between the two layers. Here, by “pressure”, we are referring to the dynamic pressure, where the hydrostatic component has been subtracted out. In the lower layer momentum equation, we have retained the Rayleigh damping term, which parameterizes the effects of bottom friction, to allow for the possibility of recovering the FG model in the lower layer.

We first employ the generic scalings

$$\begin{aligned} (x^*, y^*) &= L(x, y), \quad \mathbf{u}_1^* = U_1 \mathbf{u}_1, \quad \mathbf{u}_2^* = U_2 \mathbf{u}_2, \\ t^* &= Tt, \quad f^* = f_0 f, \quad r^* = f_0 r, \quad p^* = s \rho_2 g' H p \\ \eta^* &= \frac{g'}{g} \delta H \eta, \quad h^* = \delta H h, \quad h_B^* = s H h_B, \end{aligned} \quad (4.17)$$

where $s = h_B^*/H = s^* L/H$ and $\delta = h^*/H$ are dimensionless parameters representing the ratios of the scale height of, respectively, the bottom topography and the lower layer thickness, to the scale height of the upper layer (see Figure 4.1). A relatively thin lower layer and a shallowly sloping bottom correspond to $0 < \delta \ll 1$ and $0 < s \ll 1$.

Substituting the above scalings into the shallow-water equations yields

$$U_1 \left(\frac{L}{T} \mathbf{u}_{1t} + U_1 \mathbf{u}_1 \cdot \nabla \mathbf{u}_1 \right) + f_0 U_1 L f \hat{\mathbf{e}}_3 \times \mathbf{u}_1 = -\delta g' H \nabla \eta, \quad (4.18)$$

$$\nabla \cdot \mathbf{u}_1 = s h_t + \nabla \cdot (\mathbf{u}_1 (\delta h + s h_B)). \quad (4.19)$$

$$U_2^2 (\mathbf{u}_{2t} + \mathbf{u}_2 \cdot \nabla \mathbf{u}_2) + f_0 U_2 L f \hat{\mathbf{e}}_3 \times \mathbf{u}_2 = -g' H \nabla [\delta (\eta + h) + s h_B] - f_0 U_2 L r \mathbf{u}_2, \quad (4.20)$$

$$h_t + \nabla \cdot (\mathbf{u}_2 h) = 0. \quad (4.21)$$

Time has been scaled advectively with respect to the lower layer velocity so that $T = L/U_2$. Also, we have made the rigid lid approximation, valid for $g'/g \ll 1$, by

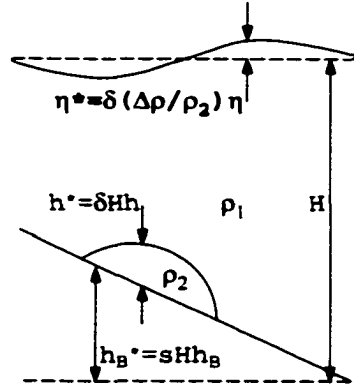


Figure 4.1: The geometry of the problem.

neglecting the η terms in the upper layer conservation of mass equation (4.13) and the term proportional to g'/g in the lower layer pressure equation (4.16). The lower layer height h and bottom topography h_B have been assumed to be much smaller in amplitude than the overlying ocean, and the upper and lower layer pressures have been scaled such that the upper layer pressure strongly interacts with the lower layer height. We have retained a generic dependence of the Coriolis parameter on latitude, $f = f(y)$.

4.3 Mid-latitude model: Equatorial Swaters-Flierl

The scaling of Swaters and Flierl (1991) is applicable at mid-latitudes. Their scalings arise out of the generic scalings by setting

$$L = \frac{\sqrt{g'H}}{f_0}, \quad U_1 = \delta f_0 L, \quad T = \frac{1}{s f_0}, \quad U_2 = \frac{g's^*}{f_0} = \frac{g'sH}{f_0 L} = s f_0 L = U_1/\mu. \quad (4.22)$$

where s^* is the slope of the bottom topography and

$$\mu = \frac{\delta}{s}. \quad (4.23)$$

The parameter μ is one of the key parameters related to the stability characteristics of the Swaters and Flierl (1991) model, and we will refer to it as the Swaters stability parameter. It is a measure of the ratio of the destabilizing effect of baroclinicity to the stabilizing effect of bottom slope (Swaters 1991).

The length scale is then the Rossby deformation radius of the upper layer, and the lower layer velocity scale is the Nof (1983) speed. The parameter s is related to the slope of the bottom topography, s^* , via $s = s^*L/H$, and so is referred to as the scaled slope parameter. In these scalings, s also plays the role of the Rossby number of the flow¹, by virtue of the definition for U_2 ,

$$s = \frac{U_2}{f_0 L}.$$

We will, in general, assume that $s \ll 1$, so that s will serve as the small parameter in our asymptotic expansions.

With the scalings (4.22), the governing equations now take the form

$$s(\mathbf{u}_{1t} + \mu \mathbf{u}_1 \cdot \nabla \mathbf{u}_1) + f \hat{\mathbf{e}}_3 \times \mathbf{u}_1 = -\nabla \eta. \quad (4.24)$$

$$\nabla \cdot \mathbf{u}_1 = s\{h_t + \nabla \cdot [\mathbf{u}_1(\mu h + h_B)]\}. \quad (4.25)$$

$$s(\mathbf{u}_{2t} + \mathbf{u}_2 \cdot \nabla \mathbf{u}_2) + f \hat{\mathbf{e}}_3 \times \mathbf{u}_2 = -\nabla(\mu(\eta + h) + h_B) - r \mathbf{u}_2. \quad (4.26)$$

¹ s is the temporal and advective Rossby number of the lower layer, but only the temporal Rossby number of the upper layer. δ is the advective Rossby number of the upper layer.

$$h_t + \nabla \cdot (\mathbf{u}_2 h) = 0. \quad (4.27)$$

When $f \equiv 1$, the model is geostrophic to leading order, and expanding the dependent variables in terms of the asymptotic parameter s , as well as taking $r \rightarrow 0$, yields the Swaters and Flierl (1991) model. However, when $f \rightarrow 0$, the scaling of the terms in the upper layer momentum equation (4.24) implies that the nondimensional gradient of pressure $\nabla \eta$ will adjust from $O(1)$ to $O(s)$ to balance the remaining terms. Thus, in the context of these nondimensional scales, we expect that $\nabla \eta$ will be $O(s)$ at the equator. In fact, we show in Section 4.4 that such an assumption about the scaling of η yields dynamics equivalent to that of a model derived from standard equatorial β -plane scalings.

The model we will obtain with these scalings is derived by forming the vorticity equation and the divergence equation of the upper layer. The divergence equation is formed by taking the divergence of the momentum equations, and will provide a generalization of geostrophic balance that is valid at the equator. The vorticity equation is formed by taking the curl of the momentum equation. The upper layer equations will be expressed in terms of a stream function and a velocity potential, using the assumption that the upper layer velocity field may be written as the sum of a nondivergent part and an irrotational part, i.e. employing the Helmholtz decomposition

$$\mathbf{u}_1 = \hat{\mathbf{e}}_3 \times \nabla \psi + s \nabla \chi. \quad (4.28)$$

The irrotational part is assumed to be $O(s)$ because the divergence of the upper layer velocity is $O(s)$ (see 4.25).

4.3.1 Derivation of the vorticity equation

The vorticity equation is formed by taking (the vertical component of) the curl of the momentum equation (4.24). We first rewrite the momentum equation into the following form:

$$s\mathbf{u}_{1t} + (f + s\mu\zeta)\hat{\mathbf{e}}_3 \times \mathbf{u}_1 + \nabla \left(\eta + \frac{1}{2}s\mu\mathbf{u}_1 \cdot \mathbf{u}_1 \right) = \mathbf{0},$$

where $\zeta = \hat{\mathbf{e}}_3 \cdot \nabla \times \mathbf{u}_1$ is the relative vorticity of the upper layer. Note that $\zeta = \Delta\psi$, by virtue of (4.28). Applying the differential operator $(\hat{\mathbf{e}}_3 \cdot \nabla \times)$ to the above equation, and using the following vector identity, which is valid for any vector function $\mathbf{u}(x, y)$ and scalar function $A(x, y)$:

$$\nabla \times (A\hat{\mathbf{e}}_3 \times \mathbf{u}) = \hat{\mathbf{e}}_3 (\mathbf{u} \cdot \nabla A + A\nabla \cdot \mathbf{u}),$$

we arrive at the vorticity equation

$$s\zeta_t + \mathbf{u}_1 \cdot \nabla (f + s\mu\zeta) + (f + s\mu\zeta)\nabla \cdot \mathbf{u}_1 = 0. \quad (4.29)$$

The upper layer conservation of mass (4.25) is used to eliminate the divergence term and (4.28) is used to rewrite the vorticity equation in terms of ψ and χ . The vector identities

$$\mathbf{u}_1 \cdot \nabla A = J(\psi, A) + s\nabla\chi \cdot \nabla A,$$

and

$$\nabla \cdot (\mathbf{u}_1 A) = J(\psi, A) + s\nabla\chi \cdot \nabla A + sA\Delta\chi,$$

where $J(A, B) = A_x B_y - A_y B_x$ is the Jacobian operator, allow us to write the vorticity equation, without approximation, as

$$\begin{aligned}
& s\Delta\psi_t + J(\psi, f + s\mu\Delta\psi) + s\nabla\chi \cdot \nabla(f + s\mu\Delta\psi) \\
& + s(f + s\mu\Delta\psi)[h_t + J(\psi, \mu h + h_B) + s(\mu h + h_B)\Delta\chi \\
& + s\nabla\chi \cdot \nabla(\mu h + h_B)] = 0.
\end{aligned} \tag{4.30}$$

While it may appear that the leading order vorticity equation is $J(\psi, f) = 0$, this is not true since, on the scales of motion we are considering, $df/dy = O(s)$ (and, of course, $df/dx = 0$). The alternate assumption, $df/dy = O(s^0)$, corresponds to considering basin-sized scales of motion. Our analysis does not apply to that scale since we have neglected other dynamics important on that scale such as wind-driven circulation, which causes vertical velocities. In fact, the leading-order vorticity balance on that scale is known to be $\beta v = f\partial w/\partial z$, where w is the vertical velocity, and is called the Sverdrup relation (Pedlosky 1996). Note that $J(\psi, f) = 0$ is the Sverdrup relation with $w \equiv 0$.

The leading-order vorticity equation may therefore be written

$$\Delta\psi_t + J(\psi, f/s + \mu\Delta\psi) + f\{h_t + J(\psi, \mu h + h_B)\} = 0. \tag{4.31}$$

where ψ is the stream function for the rotational part of the velocity. The vorticity equation used in the model of Swaters and Flierl (1991) is recovered if $f \equiv 1$. Note that we have neglected the $\nabla\chi \cdot \nabla f$ term since $df/dy = O(s)$.

4.3.2 Divergence equation derivation

To derive the divergence equation, it is convenient to use the form of the momentum equations as expressed in (4.24). The following definitions and relations are used:

$$\nabla \cdot s\mathbf{u}_{1t} = s^2\Delta\chi_t, \quad \nabla \cdot \nabla\eta = \Delta\eta,$$

and

$$\begin{aligned} \nabla \cdot [f\hat{\mathbf{e}}_3 \times \mathbf{u}_1] &= \nabla \cdot \{f[-\nabla\psi + s\hat{\mathbf{e}}_3 \times \nabla\chi]\} \\ &= -\nabla \cdot [f\nabla\psi] + s\nabla f \cdot \hat{\mathbf{e}}_3 \times \nabla\chi \\ &= -\nabla \cdot [f\nabla\psi] + sJ(\chi, f). \end{aligned}$$

The most straightforward way to calculate the divergence of the advection terms is to write out the terms explicitly. Denoting $\mathbf{u}_1 = (u, v)$ so that $u = -\psi_y + s\chi_x$ and $v = \psi_x + s\chi_y$,

$$\begin{aligned} \nabla \cdot [\mathbf{u}_1 \cdot \nabla\mathbf{u}_1] &= u_x u_x + 2u_y v_x + v_y v_y + u(u_x + v_y)_x + v(u_x + v_y)_y \\ &= 2J(\psi_y, \psi_x) + s\{J(\psi, \Delta\chi) + 2J(\psi_x, \chi_x) + 2J(\psi_y, \chi_y)\} \\ &\quad + s^2\{\nabla \cdot [\Delta\chi \nabla\chi] + 2J(\chi_y, \chi_x)\}. \end{aligned}$$

The full divergence equation is therefore

$$\begin{aligned} &s^2\Delta\chi_t + 2s\mu J(\psi_y, \psi_x) + s^2\mu\{J(\psi, \Delta\chi) + 2J(\psi_x, \chi_x) + 2J(\psi_y, \chi_y)\} \\ &+ s^3\mu\{\nabla \cdot [\Delta\chi \nabla\chi] + 2J(\chi_y, \chi_x)\} - \nabla \cdot [f\nabla\psi] + sJ(\chi, f) + \Delta\eta = 0. \end{aligned} \quad (4.32)$$

Therefore, the leading order balance is

$$\Delta\eta = \nabla \cdot [f\nabla\psi]. \quad (4.33)$$

This equation is a generalization of geostrophic balance. When $f \equiv 1$ (and with identical boundary conditions on η and ψ), this reduces to $\eta = \psi$, the statement that

the geostrophic pressure is a stream function for the flow. Equation (4.33) is the divergence equation in the “Linear Balance Equations” of Gent and McWilliams (1983). Additionally, note that this relation contains within it the equatorial geostrophic relation $\beta u = -\eta_{yy}$, where β is the meridional derivative of the Coriolis parameter. The equatorial geostrophic relation may be derived by taking the meridional derivative of the expression of geostrophic balance between the zonal velocity and the meridional pressure gradient, assuming that the meridional pressure gradient vanishes right on the equator (McCartney and Curry 1993). At $f = 0$, (4.33) reduces to $\Delta\eta = J\psi_y$, which simplifies to the equatorial geostrophic relation if it is further assumed that $\eta_{xx} = 0$.

4.3.3 Mid-latitude model

For reference, we state here the model we have derived. We first state the equations of motion for which no approximations have been made. In the upper layer, these consist of the vorticity equation (4.30) and the divergence equation (4.32), while in the lower layer, they are the conservation of momentum (4.26) and mass (4.27). One more equation is required: the upper-layer conservation of mass equation, which will be used to solve for χ , if needed. From (4.25),

$$\begin{aligned}
 \Delta\chi &= h_t + \nabla \cdot [\mathbf{u}_1(\mu h + h_B)] \\
 &= h_t + \mathbf{u}_1 \cdot \nabla(\mu h + h_B) + (\mu h + h_B)s\Delta\chi \\
 &= h_t + J(\psi, \mu h + h_B) + s\nabla \cdot [\nabla\chi(\mu h + h_B)].
 \end{aligned}$$

This set of equations is, in fact, the full set of shallow-water equations stated in terms of ψ , χ and s , and are valid for any s . This fact will be exploited when we derive a model valid for both mid-latitude scalings and equatorial scalings simultaneously.

Full equations without approximation

These equations are as follows:

$$\begin{aligned}
& s\Delta\psi_t + J(\psi, f + s\mu\Delta\psi) + s\nabla\chi \cdot \nabla(f + s\mu\Delta\psi) \\
& + s(f + s\mu\Delta\psi)[h_t + J(\psi, \mu h + h_B) + s(\mu h + h_B)\Delta\chi \\
& + s\nabla\chi \cdot \nabla(\mu h + h_B)] = 0.
\end{aligned} \tag{4.34}$$

$$\begin{aligned}
& s^2\Delta\chi_t + 2s\mu J(\psi_y, \psi_x) + s^2\mu\{J(\psi, \Delta\chi) + 2J(\psi_x, \chi_x) + 2J(\psi_y, \chi_y)\} \\
& + s^3\mu\{\nabla \cdot [\Delta\chi\nabla\chi] + 2J(\chi_y, \chi_x)\} - \nabla \cdot [f\nabla\psi] + sJ(\chi, f) + \Delta\eta = 0.
\end{aligned} \tag{4.35}$$

$$\Delta\chi = h_t + J(\psi, \mu h + h_B) + s\nabla \cdot [\nabla\chi(\mu h + h_B)]. \tag{4.36}$$

$$s(\mathbf{u}_{2t} + \mathbf{u}_2 \cdot \nabla\mathbf{u}_2) + f\hat{\mathbf{e}}_3 \times \mathbf{u}_2 = -\nabla(\mu(\eta + h) + h_B) - r\mathbf{u}_2. \tag{4.37}$$

$$h_t + \nabla \cdot (\mathbf{u}_2 h) = 0. \tag{4.38}$$

The leading-order equations for the upper layer in this model are the vorticity equation (4.31) and the balance equation (4.33). Our two-layer model is formed by coupling these equations with the complete lower-layer equations as stated above in (4.37) and (4.38).

Equatorial Swaters-Flierl model

In summary, then, the leading-order model derived from a mid-latitude scaling is

$$\Delta\psi_t + J(\psi, f/s + \mu\Delta\psi) + f \{h_t + J(\psi, \mu h + h_B)\} = 0. \quad (4.39)$$

$$\Delta\eta = \nabla \cdot [f\nabla\psi], \quad (4.40)$$

$$h_t + \nabla \cdot (\mathbf{u}_2 h) = 0. \quad (4.41)$$

$$s(\mathbf{u}_{2t} + \mathbf{u}_2 \cdot \nabla \mathbf{u}_2) + f\hat{\mathbf{e}}_3 \times \mathbf{u}_2 = -\nabla(\mu(\eta + h) + h_B) - r\mathbf{u}_2. \quad (4.42)$$

Although the model was derived from a mid-latitude scaling, it allows f to vary, and indeed, no singularities arise in the $f \rightarrow 0$ limit. It is straightforward to check that as $f \rightarrow 1$ and $r \rightarrow 0$, this system reduces to the Swaters and Flierl (1991) model. Thus, we have successfully derived a version of that model that describes well-defined flow at the equator, and so we refer to it as the Equatorial Swaters-Flierl model, henceforth abbreviated as the ESF model.

In the lower layer momentum equations (4.42), we have retained both the $O(s)$ inertial terms and the $O(r)$ frictional term. In the $s \ll r$ limit, the frictional geostrophic model discussed in the previous chapter is recovered. In the $r \ll s$ limit, the frictionless and inertial shallow-water model, with s as a Rossby number, is recovered. Thus, the model as written is general enough to employ either model studied in the previous chapter to govern the lower layer dynamics.

4.3.4 ESF model simulations

Numerical simulations of this model will allow us to assess whether this model does, in fact, reproduce the behaviour of the Swaters and Flierl (1991), and to investigate if this model has any equatorial waves.

The numerical procedure used is similar to the procedure of Swaters (1998) for the upper layer equations, and identical to the procedure described in Chapter 3 for the lower layer equations. At each time step, we solve the model equations in the following order:

$$q_t + J(\psi, q + f - fh) + fJ(\psi, h + h_b) = 0.$$

$$s(\mathbf{u}_{2t} + \mathbf{u}_2 \cdot \nabla \mathbf{u}_2) + f\hat{\mathbf{e}}_3 \times \mathbf{u}_2 = -\nabla(\mu(\eta + h) + h_B) - r\mathbf{u}_2,$$

$$h_t + \nabla \cdot (\mathbf{u}_2 h) = 0.$$

$$\Delta\psi = q - fh,$$

$$\Delta\eta = \nabla \cdot [f\nabla\psi].$$

where the vorticity $q = \Delta\psi + fh$ is updated using a leapfrog time discretization. Arakawa and Lamb (1981) schemes are employed for the Jacobian terms, and the Laplacian operators are inverted using the same direct solver (see Swaters 1998). The lower layer velocity field and the lower layer height field are advanced via methods described in Chapter 3.

We begin with a test simulation of the ESF model where $f = 1$, $r = 0$, and the bottom topography is that of a linearly sloping shelf, $h_B = y$. Under the conditions

of $f = 1$ and $r = 0$, the model should reduce to the Swaters (1991) model. The simulation shown in Figure 4.2 is set up similarly to the simulations of Swaters (1998). The results seem very similar to those of Swaters (1998). For example, the baroclinic instabilities that are preferentially amplified on the downslope side of the current are clearly seen. Throughout the simulation, the η and ψ fields are identical. This shows that the ESF model derived is indeed a generalization of the Swaters and Flierl (1991) model to the case of varying Coriolis parameter, and indeed, allowing for $f = 0$ in the domain.

When we perform simulations of the ESF model over idealized meridional channel topography (Figure 4.3), we see little qualitative differences from the one-layer model simulations. As the equator is approached, the lack of coupling between layers is apparent. In Figure 4.3, the lower layer is FG dynamics. We show in Figure 4.4 snapshots from simulations in which the lower layer is governed by shallow-water dynamics. In neither of these simulations does there appear to be much wave motion in the upper layer. The lower layer seems to behave exactly as in the one-layer simulations. Even quantitatively (right-hand plots), there is not much difference.

To investigate the wave-nature of the upper layer, we display in Figure 4.5 a similar simulation, but with the eddy initially on the left slope of the topography right on the equator. The results are similar: although the upper layer seems to be forced by the lower layer, there seems to be little dynamical influence of the upper layer back on the lower layer.

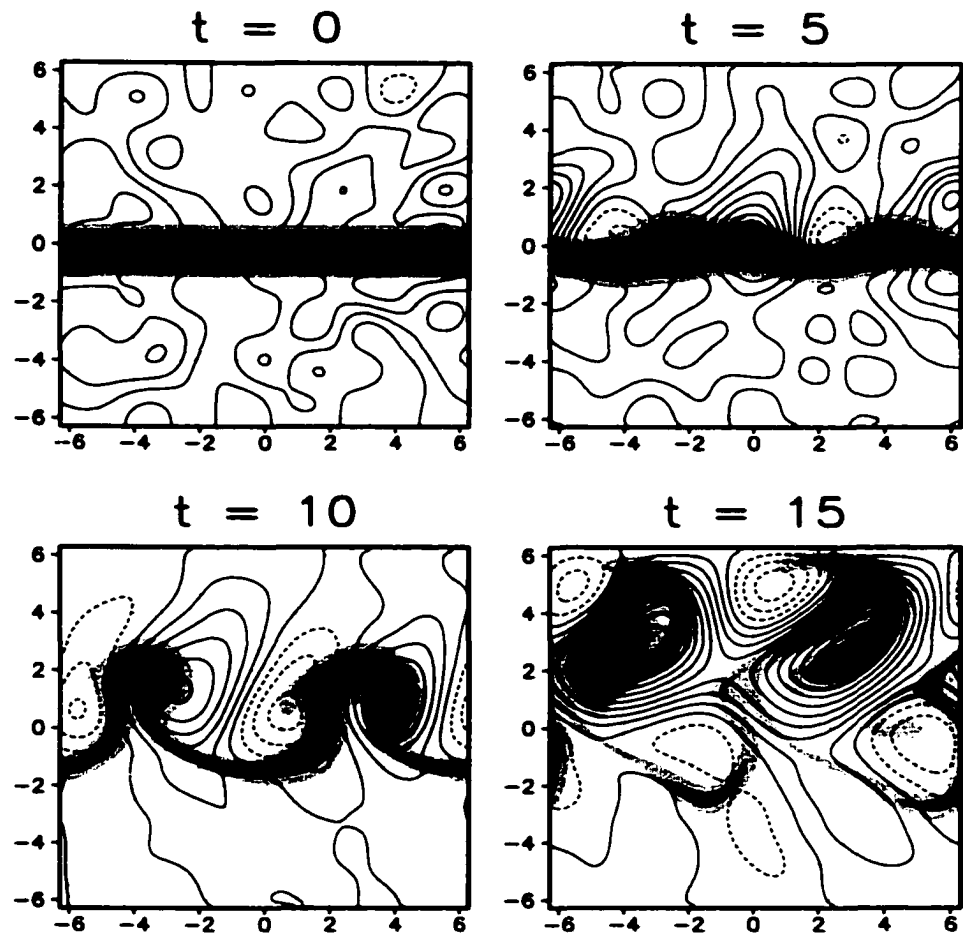


Figure 4.2: Two-layer model simulation with $f = 1$, $r = 0$, and $h_B = y$. The shaded region is the lower layer height, darker corresponds to higher values. Contours are of the upper layer η field. The ψ field is exactly equal to the η field. Contour interval is 0.05 for $t = 0, 5$ and 0.25 for $t = 10, 15$. Dotted contours denote negative values.

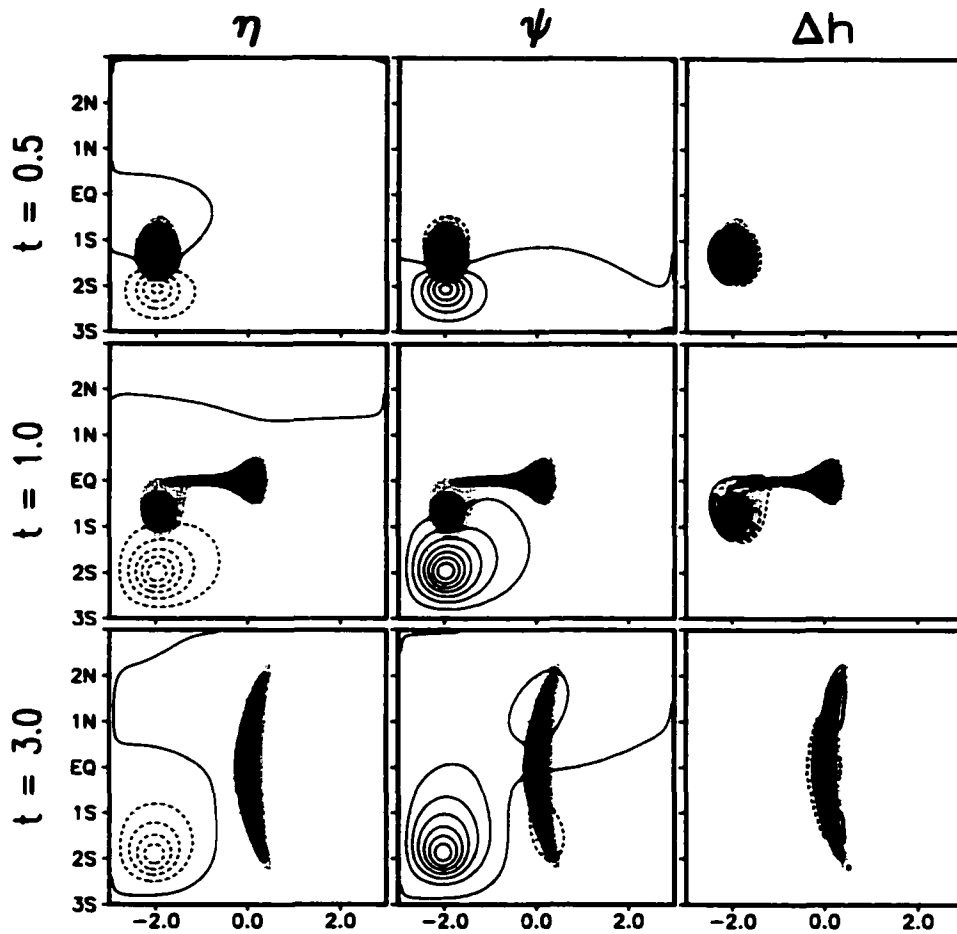


Figure 4.3: Two-layer model simulation over idealized channel. lower layer is FG model. The shaded region is the lower layer height, darker corresponds to higher values. Contours are of the upper layer η field, ψ field, or Δh field, where $\Delta h = h_{1\text{-layer}} - h_{2\text{-layer}}$. Contour interval is 0.005, with ± 0.001 replacing the zero contour for Δh .

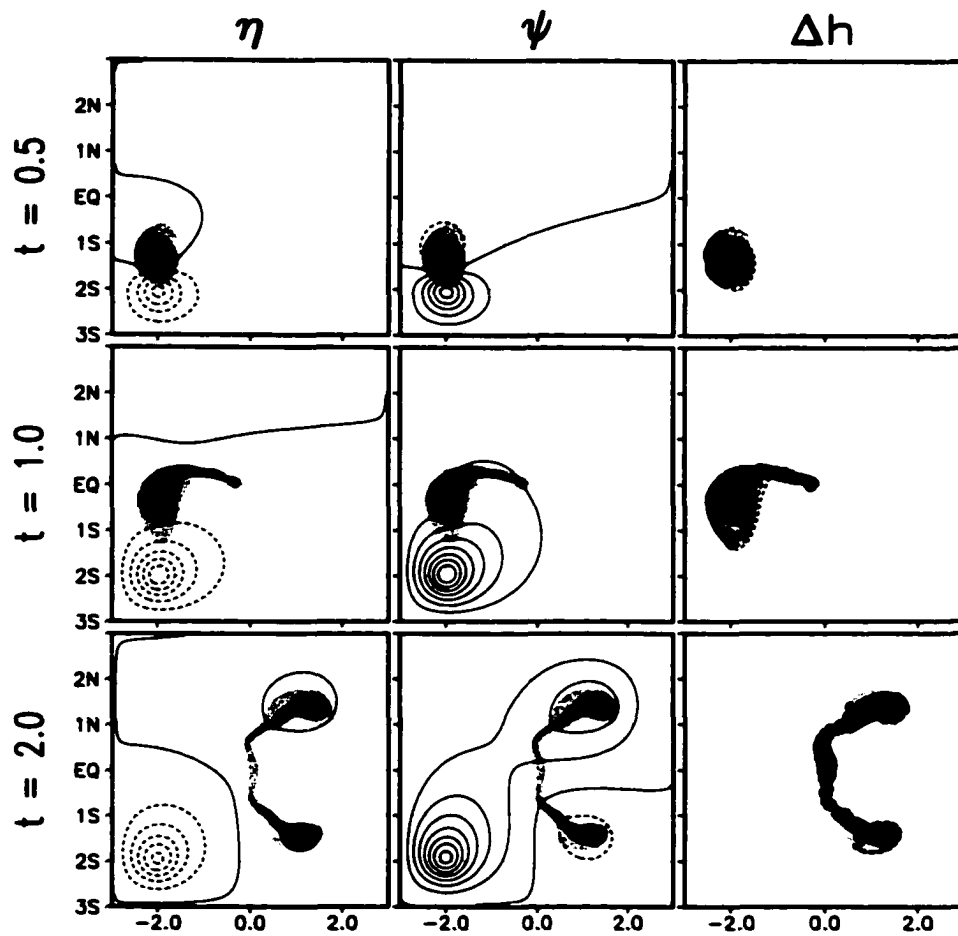


Figure 4.4: Two-layer model simulation over idealized channel. lower layer is governed by the shallow-water model. Displayed fields and contour levels are as in Figure 4.3.

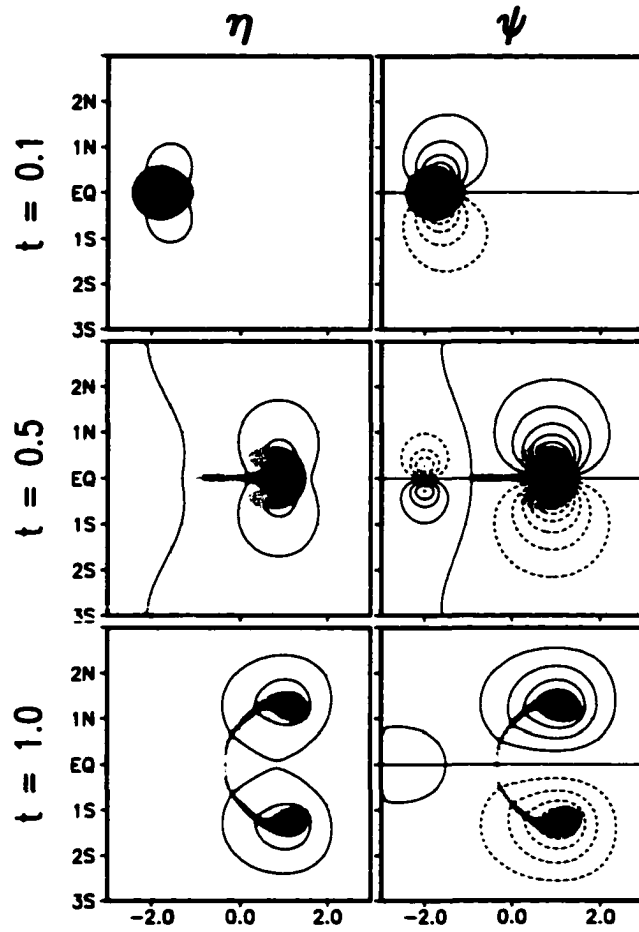


Figure 4.5: Two-layer model simulation, eastward eddy. Contour interval is 0.00025 for $t = 0.1, 0.5$ and 0.0025 for $t = 1.0$.

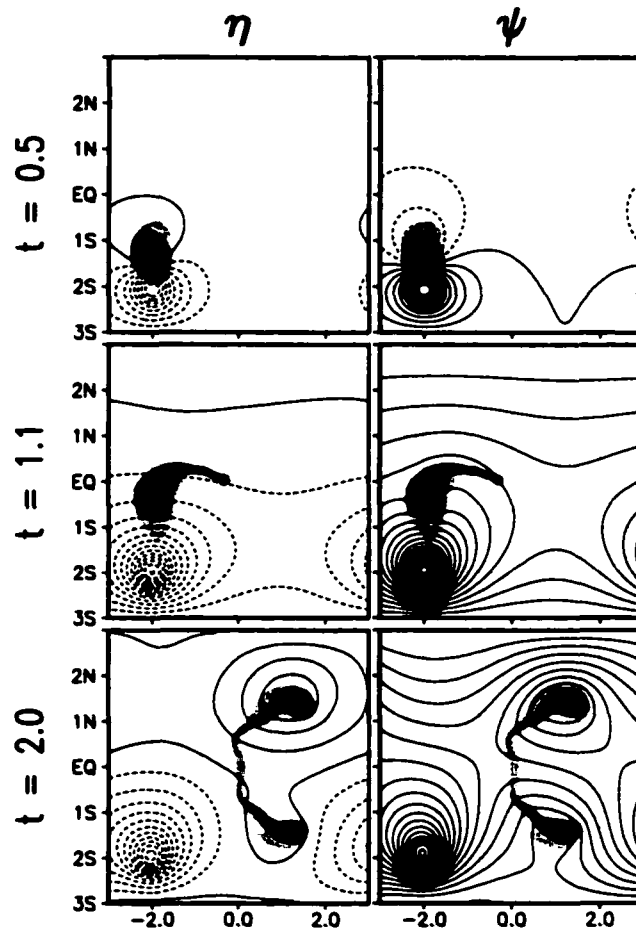


Figure 4.6: Two-layer model simulation over idealized channel. lower layer is governed by the shallow-water model. periodic conditions. Contour interval is 0.0025.

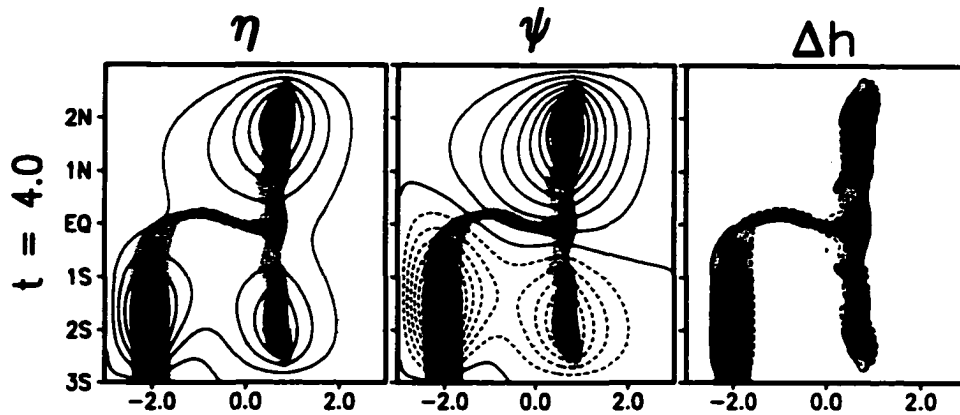


Figure 4.7: Two-layer model simulation over idealized channel. lower layer is governed by the shallow-water model, inflow current. Contour interval is 0.0025 for η and ψ , and 0.005 for Δh .

A test run was performed (Figure 4.6) to make sure the boundaries were not impeding wave motions in the upper layer. In this run, the upper layer boundary conditions were periodic in the zonal direction. The upper layer eddy which was spun up from the initial conditions remains stationary, however. There is a slow drift, but it is on much slower time scales than the behaviour of the lower layer.

Finally, to investigate conditions that are more relevant to AABW flow than that of an eddy, we simulated a current flowing into the domain with steady inflow conditions (Figure 4.7). The current behaves in a similar way to that observed in the simulations of Nof and Borisov (1998).

4.4 Equatorial model

The traditional nondimensional scaling in the study of equatorial dynamics uses the equatorial deformation radius (Cushman-Roisin 1994) as the length scale. The equatorial scaling may be conveniently stated by replacing f_0 with $\beta_0 L$, where we define $\beta_0 = df/dy$ at $y = 0$.

$$L = \frac{\sqrt{g'sH}}{\beta_0 L}, \quad U_1 = \mu\beta_0 L^2, \quad T = \frac{1}{\beta_0 L}, \quad U_2 = \frac{g's^*}{\beta_0 L} = \frac{g'sH}{\beta_0 L^2} = \beta_0 L^2 = U_1/\mu. \quad (4.43)$$

Note that the Nof (1983) velocity scaling is retained, but the length scale is now the Rossby deformation radius of the *lower* layer. We have scaled the velocity slightly differently in the two layers, incorporating the Swaters stability parameter μ in the same way as in the mid-latitude scaling. With the scaling (4.43), the equations of motion (4.18)–(4.21) become

$$\mathbf{u}_{1t} + \mu\mathbf{u}_1 \cdot \nabla\mathbf{u}_1 + f\hat{\mathbf{e}}_3 \times \mathbf{u}_1 = -\nabla\eta. \quad (4.44)$$

$$\nabla \cdot \mathbf{u}_1 = s\{h_t + \nabla \cdot [\mathbf{u}_1(\mu h + h_B)]\}. \quad (4.45)$$

$$\mathbf{u}_{2t} + \mathbf{u}_2 \cdot \nabla\mathbf{u}_2 + f\hat{\mathbf{e}}_3 \times \mathbf{u}_2 = -\nabla(\mu(\eta + h) + h_B) - r\mathbf{u}_2. \quad (4.46)$$

$$h_t + \nabla \cdot (\mathbf{u}_2 h) = 0. \quad (4.47)$$

The variable f appearing in the equations now acts as the inverse of the Rossby number of the flow. In the $f \gg 1$ regime, the dynamics will be geostrophic, and so the Swaters and Flierl (1991) model is relevant in that limit.

4.4.1 Equatorial model derivation

The momentum equations scaled for equatorial flow do not seem to be simplified at all as compared to the full shallow-water equations. However, in the upper layer, the conservation of mass equation implies that we can still justify the assumption of the Charney balance model, in which the velocity field is written as the sum of its irrotational and nondivergent parts, with an order $O(s)$ irrotational part.

$$\mathbf{u}_1 = \nabla \times \psi + s \nabla \chi. \quad (4.48)$$

Following the derivation of the upper layer equations for the case of the mid-latitude scaling, we first note that the upper layer vorticity equation,

$$\zeta_t + \mathbf{u}_1 \cdot \nabla (f + \mu \zeta) + (f + \mu \zeta) \nabla \cdot \mathbf{u}_1 = 0. \quad (4.49)$$

is as in Section 4.3, but effectively with $s = 1$. Eliminating the divergence term and writing the vorticity equation in terms of ψ and χ ,

$$\begin{aligned} \Delta \psi_t + J(\psi, f + \mu \Delta \psi) + s \nabla \chi \cdot \nabla (f + \mu \Delta \psi) \\ + s (f + \mu \Delta \psi) [h_t + J(\psi, \mu h + h_B) + s (\mu h + h_B) \Delta \chi \\ + s \nabla \chi \cdot \nabla (\mu h + h_B)] = 0. \end{aligned} \quad (4.50)$$

The leading-order vorticity equation is

$$\Delta \psi_t + J(\psi, f + \mu \Delta \psi) = 0. \quad (4.51)$$

In this form, the connection to equation (4.39) is clear: this form may be derived from (4.39) in the limit as $f \rightarrow O(s)$. Stated another way, the model of Swaters and

Flierl (1991) may be derived from this model in the limit as $f \rightarrow O(s^{-1})$. Note that, in the equatorial scaling, $df/dy = O(1)$, so the $J(\psi, f)$ term is retained.

According to (4.51), the vorticity equation is not at all coupled to the lower layer height field. This is reasonable in the sense that as $f \rightarrow O(s)$ in (4.39), the terms involving the lower layer height do indeed move to the next order. Also, the model is still coupled in the sense that motions in the ψ field will affect the h field. However, there is nothing to induce motions in the upper layer stream function field except perhaps boundary forcing, i.e. the stream function may be forced by waves propagating in from the far-field. If motions are not explicitly inserted into the upper layer stream function field by boundary forcing, then the solution to (4.51) is $\psi = 0$. In that case, the stream function is an $O(s)$ quantity to leading order. Therefore, we have two cases to explore: the boundary-forced $\psi = O(1)$ case, and the $\psi = O(s)$ case. Let us first complete our derivation of the $\psi = O(1)$ model before we turn our attention to the $\psi = O(s)$ model.

4.4.2 Boundary-forced $\psi = O(1)$ model

The leading-order momentum equation for this model is (4.51). The derivation of the divergence of the momentum equations is similar to the Section 4.3 derivation, yielding

$$\begin{aligned}
 & s\Delta\chi_t + 2\mu J(\psi_y, \psi_x) + s\mu\{J(\psi, \Delta\chi) + 2J(\psi_x, \chi_x) + 2J(\psi_y, \chi_y)\} \\
 & + s^2\mu\{\nabla \cdot [\Delta\chi \nabla\chi] + 2J(\chi_y, \chi_x)\} - \nabla \cdot [f\nabla\psi] + sJ(\chi, f) + \Delta\eta = 0.
 \end{aligned} \tag{4.52}$$

Neglecting the $O(s)$ terms, the upper layer balance may be written

$$\Delta\eta = \nabla \cdot [f\nabla\psi] + 2J(\psi_x, \psi_y), \quad (4.53)$$

which is similar to the balance equation with the mid-latitude scaling, but with the additional nonlinear term. This equation is exactly the form of the divergence equation appearing in the Balance Equations of Gent and McWilliams (1983).

For convenient reference, we restate here the entire leading-order boundary-forced equatorial model. The vorticity equation is as stated in (4.51). The divergence equation is (4.53). The conservation of momentum (4.46) and mass (4.47) equations are only simplified by the neglect of the $O(r)$ term.

Boundary-forced equatorial model

This model consists of the following set of equations:

$$\Delta\psi_t + J(\psi, f + \mu\Delta\psi) = 0. \quad (4.54)$$

$$\Delta\eta = \nabla \cdot [f\nabla\psi] + 2J(\psi_x, \psi_y). \quad (4.55)$$

$$\mathbf{u}_{2t} + \mathbf{u}_2 \cdot \nabla \mathbf{u}_2 + f\hat{\mathbf{e}}_3 \times \mathbf{u}_2 = -\nabla(\mu(\eta + h) + h_B). \quad (4.56)$$

$$h_t + \nabla \cdot (\mathbf{u}_2 h) = 0. \quad (4.57)$$

4.4.3 Lower-layer-forced $\psi = O(s)$ model

We assume here that the stream function is an $O(s)$ quantity to leading order. We rescale ψ so that

$$\psi = s\tilde{\psi},$$

where $\tilde{\psi} = O(1)$. Rescaling the full vorticity equation (4.50) to take this into account reveals that the leading order vorticity equation is

$$\Delta\tilde{\psi}_t + J(\tilde{\psi}, f) + \nabla\chi \cdot \nabla f + fh_t = 0. \quad (4.58)$$

Physically, this means that the time rate of change of $\Delta\tilde{\psi} + fh$, which is the leading-order potential vorticity in the upper layer, is forced by the northward advection of planetary vorticity. At this order, h appears explicitly so that the upper layer relative vorticity may be thought of as being forced by the lower layer height field.

The divergence of the momentum equations (4.52) with $w = s\tilde{w}$ becomes

$$\begin{aligned} & s\Delta\chi_t + 2s^2\mu J(\tilde{w}_y, \tilde{w}_x) + s^2\mu\{J(\tilde{\psi}, \Delta\chi) + 2J(\tilde{w}_x, \chi_x) + 2J(\tilde{w}_y, \chi_y)\} \\ & + s^2\mu\{\nabla \cdot [\Delta\chi \nabla\chi] + 2J(\chi_y, \chi_x)\} - s\nabla \cdot [f\nabla\tilde{\psi}] + sJ(\chi, f) + \Delta\eta = 0. \end{aligned} \quad (4.59)$$

which alerts us to the fact that η must be rescaled for the same reasons as w .

$$\eta = s\tilde{\eta}.$$

The leading-order balance equation is now

$$\Delta\chi_t + \Delta\tilde{\eta} = \nabla \cdot [f\nabla\tilde{\psi}] + J(f, \chi). \quad (4.60)$$

With $\eta = O(s)$, however, the upper layer variables are removed from the lower layer dynamics to leading order. The motion in the lower layer is still forced by the sloping topography, so the solution of the lower layer is not that of no motion.

The velocity potential χ appears explicitly in the model. Therefore, we will need an additional equation to solve for χ . From (4.45),

$$\begin{aligned}\Delta\chi &= h_t + \nabla \cdot [\mathbf{u}_1(\mu h + h_B)] \\ &= h_t + \mathbf{u}_1 \cdot \nabla(\mu h + h_B) + (\mu h + h_B)s\Delta\chi \\ &= h_t + sJ(\tilde{\psi}, \mu h + h_B) + s\nabla \cdot [\nabla\chi(\mu h + h_B)],\end{aligned}$$

so the leading-order equation for χ is

$$\Delta\chi = h_t. \quad (4.61)$$

This is the statement that lower layer height changes cause divergence or convergence in the upper layer. This is reasonable, considering that the rigid-lid approximation has been made.

In the lower layer equations (4.46) and (4.47), all the terms seem to be scaled with equal weight, except for the η in the pressure term, which is now $O(s)$. Therefore, the lower layer equations of this model are the shallow-water equations, uncoupled from the upper layer.

Lower-layer-forced $\psi = O(s)$ model

The equatorial model in which $\tilde{\psi}$ is driven by coupling with the lower layer is thus

$$\Delta\tilde{\psi}_t + J(\tilde{\psi}, f) + \nabla\chi \cdot \nabla f + fh_t = 0, \quad (4.62)$$

$$\Delta\chi_t + \Delta\tilde{\eta} = \nabla \cdot [f\nabla\tilde{\psi}] + J(f, \chi), \quad (4.63)$$

$$\Delta\chi = h_t, \quad (4.64)$$

$$\mathbf{u}_{2t} + \mathbf{u}_2 \cdot \nabla \mathbf{u}_2 + f\hat{\mathbf{e}}_3 \times \mathbf{u}_2 = -\nabla(\mu h + h_B), \quad (4.65)$$

$$h_t + \nabla \cdot (\mathbf{u}_2 h) = 0. \quad (4.66)$$

Each of the two models derived from equatorial scales of motion is a partially uncoupled model. In the $\psi = O(1)$ model (4.54)–(4.57), the upper layer variables are not directly affected by the lower layer variables, and in the $\psi = O(s)$ model (4.62)–(4.66), the lower layer variables are not directly affected by the upper layer variables. This weakening of the coupling mechanism in the vicinity of the equator lends support to the relevance of the reduced-gravity simulations studied in Chapter 3.

4.4.4 Waves in the lower-layer-forced model

We show in this section that the $\psi = O(s)$ equatorial model (4.62)–(4.66) is equivalent to a two-layer equatorial model whose upper layer is described by linear equatorial dynamics and whose lower layer is governed by the shallow-water equations. Let us write out the model for the case where $f = \beta y$, $r = 0$, $\mu = 1$, and $h_B = 0$, and linearize the equations about a state where $h = 1$ and all the other variables are zero. The model then takes the form

$$\Delta\tilde{\psi}_t + \beta\tilde{\psi}_x + \beta\chi_y + \beta y\Delta\chi = 0.$$

$$\Delta\chi_t + \Delta\tilde{\eta} = \beta y\Delta\tilde{\psi} + \beta\tilde{\psi}_y - \beta\chi_x.$$

$$\Delta \chi = h_t, \quad (4.67)$$

$$\mathbf{u}_{2t} + \beta y \hat{\mathbf{e}}_3 \times \mathbf{u}_2 = -\nabla h,$$

$$h_t + \nabla \cdot \mathbf{u}_2 = 0.$$

The lower layer equations are identical to the linearized equations of motion (2.16) in our analysis of one-layer equatorial waves, with the nondimensional scalings such that $H = 1$ and $g = 1$. How similar are the model's upper layer equations to the upper layer equations in the two-layer rigid-lid model whose waves were analyzed in Chapter 2? The upper layer equations in the set (2.22), which represents two-layer linear dynamics, with $g = 1$ and $H_1 = 1$ are

$$\begin{aligned} u_{1t} - \beta y v_1 &= -\eta_x, \\ v_{1t} + \beta y u_1 &= -\eta_y, \\ -h_t + u_{1x} + v_{1y} &= 0. \end{aligned} \quad (4.68)$$

With the Helmholtz decomposition $u_1 = -\tilde{\psi}_y + \chi_x$, $v_1 = \tilde{\psi}_x + \chi_y$, the vorticity, divergence, and mass equations take the form

$$\begin{aligned} \Delta \tilde{\psi}_t + \beta y \Delta \chi + \beta(\tilde{\psi}_x + \chi_y) &= 0, \\ \Delta \chi_t - \beta y \Delta \tilde{\psi} + \beta(\tilde{\psi}_y - \chi_x) &= -\Delta \tilde{\eta}, \\ -h_t + \Delta \chi &= 0, \end{aligned}$$

which are identical to the upper layer equations in (4.67). Note that the assumptions $r = 0$, $h_B = 0$ and the linearizing process do not affect the upper layer equations at

all. Thus, if $f = \beta y$, the upper layer equations in the $\psi = O(s)$ equatorial model are completely equivalent to the upper layer of the linearized two-layer shallow-water theory analyzed in Chapter 2. Therefore, our system consists of an independent lower layer that contains all the waves of one-layer equatorial wave theory, and an upper layer driven by those waves. Although the coupling is slightly different than in the analysis of the two-layer waves performed there, it may be shown that baroclinic waves do exist in the system by considering (4.68) as the equations of motion in the upper layer. For any wave solution $\{u_2, v_2, h\}$ in the lower layer,

$$u_1 = -u_2, \quad v_1 = -v_2, \quad \eta = -h.$$

transforms the upper layer equations (4.68) into the lower layer equations, therefore $\{u_1, v_1, \eta\}$ is a solution. Thus, any wave solution discussed in Chapter 2 for the one-layer case exists in the equatorial model as a baroclinic mode.

4.5 Uniformly valid model

We seek a model that at mid-latitudes is, to leading order, the ESF model we derived, but at the equator reduces, again to leading order, to the equatorial models we found. In this section, we first derive such a model using a heuristic approach in which the balance of forces is considered at mid-latitudes and in the limit of $f \rightarrow 0$. We then show rigorously that this “meta-model” does reduce at leading order to the appropriate local model in each of the limits by expressing the variables in the

appropriate scales. We start by summarizing the mid-latitude and equatorial models we have derived, stating both the full unapproximated equations of motion and the leading-order model in each limit.

4.5.1 Model summary

The models we have derived are as follows:

Unapproximated mid-latitude model

$$\begin{aligned}
& s\Delta\psi_t + J(\psi, f + s\mu\Delta\psi) + s\nabla\chi \cdot \nabla(f + s\mu\Delta\psi) \\
& + s(f + s\mu\Delta\psi) [h_t + J(\psi, \mu h + h_B) + s(\mu h + h_B)\Delta\chi \\
& + s\nabla\chi \cdot \nabla(\mu h + h_B)] = 0, \\
& s^2\Delta\chi_t + 2s\mu J(\psi_y, \psi_x) + s^2\mu\{J(\psi, \Delta\chi) + 2J(\psi_x, \chi_x) + 2J(\psi_y, \chi_y)\} \\
& + s^3\mu\{\nabla \cdot [\Delta\chi\nabla\chi] + 2J(\chi_y, \chi_x)\} - \nabla \cdot [f\nabla\psi] + sJ(\chi, f) + \Delta\eta = 0, \\
& \Delta\chi = h_t + J(\psi, \mu h + h_B) + s\nabla \cdot [\nabla\chi(\mu h + h_B)], \\
& s(\mathbf{u}_{2t} + \mathbf{u}_2 \cdot \nabla\mathbf{u}_2) + f\hat{\mathbf{e}}_3 \times \mathbf{u}_2 = -\nabla(\mu(\eta + h) + h_B) - r\mathbf{u}_2, \\
& h_t + \nabla \cdot (\mathbf{u}_2 h) = 0.
\end{aligned} \tag{4.69}$$

Leading-order mid-latitude model

$$\begin{aligned}
& \Delta\psi_t + J(\psi, f/s + \mu\Delta\psi) + f\{h_t + J(\psi, \mu h + h_B)\} = 0, \\
& \Delta\eta = \nabla \cdot [f\nabla\psi].
\end{aligned} \tag{4.70}$$

$$h_t + \nabla \cdot (\mathbf{u}_2 h) = 0,$$

$$s(\mathbf{u}_{2t} + \mathbf{u}_2 \cdot \nabla \mathbf{u}_2) + f \hat{\mathbf{e}}_3 \times \mathbf{u}_2 = -\nabla(\mu(\eta + h) + h_B) - r \mathbf{u}_2.$$

Unapproximated equatorial model

$$\begin{aligned} \Delta \psi_t + J(\psi, f + \mu \Delta \psi) + s \nabla \chi \cdot \nabla (f + \mu \Delta \psi) \\ + s(f + \mu \Delta \psi) [h_t + J(\psi, \mu h + h_B) + s(\mu h + h_B) \Delta \chi \\ + s \nabla \chi \cdot \nabla (\mu h + h_B)] = 0. \end{aligned}$$

$$s \Delta \chi_t + 2\mu J(\psi_y, \psi_x) + s\mu \{J(\psi, \Delta \chi) + 2J(\psi_x, \chi_x) + 2J(\psi_y, \chi_y)\}$$

(4.71)

$$+ s^2 \mu \{ \nabla \cdot [\Delta \chi \nabla \chi] + 2J(\chi_y, \chi_x) \} - \nabla \cdot [f \nabla \psi] + sJ(\chi, f) + \Delta \eta = 0.$$

$$\Delta \chi = h_t + J(\psi, \mu h + h_B) + s \nabla \cdot [\nabla \chi (\mu h + h_B)].$$

$$\mathbf{u}_{2t} + \mathbf{u}_2 \cdot \nabla \mathbf{u}_2 + f \hat{\mathbf{e}}_3 \times \mathbf{u}_2 = -\nabla(\mu(\eta + h) + h_B) - r \mathbf{u}_2.$$

$$h_t + \nabla \cdot (\mathbf{u}_2 h) = 0.$$

Leading-order equatorial model, $\psi = O(1)$

$$\Delta \psi_t + J(\psi, f + \mu \Delta \psi) = 0.$$

$$\Delta \eta = \nabla \cdot [f \nabla \psi] + 2J(\psi_x, \psi_y). \quad (4.72)$$

$$\mathbf{u}_{2t} + \mathbf{u}_2 \cdot \nabla \mathbf{u}_2 + f \hat{\mathbf{e}}_3 \times \mathbf{u}_2 = -\nabla(\mu(\eta + h) + h_B).$$

$$h_t + \nabla \cdot (\mathbf{u}_2 h) = 0.$$

Leading-order equatorial model, $\psi = O(s)$

$$\Delta \tilde{\psi}_t + J(\tilde{\psi}, f) + \nabla \chi \cdot \nabla f + fh_t = 0,$$

$$\Delta \chi_t + \Delta \tilde{\eta} = \nabla \cdot [f \nabla \tilde{\psi}] + J(f, \chi), \quad (4.73)$$

$$\Delta \chi = h_t,$$

$$\mathbf{u}_{2t} + \mathbf{u}_2 \cdot \nabla \mathbf{u}_2 + f \hat{\mathbf{e}}_3 \times \mathbf{u}_2 = -\nabla(\mu h + h_B),$$

$$h_t + \nabla \cdot (\mathbf{u}_2 h) = 0.$$

4.5.2 Adjustment of dependent variables

In the above analysis, the mid-latitude nondimensional scalings led only to the mid-latitude model. However, it is possible to also derive the equatorial models using the mid-latitude scalings as long as the dependent variables are re-scaled. Observe that, if the equations of motion are scaled using the mid-latitude length and time scalings along with the additional re-scalings

$$f = O(s), \quad r = O(s), \quad \eta = O(s), \quad h = O(s), \quad \text{and} \quad h_B = O(s),$$

then the full equations of motion in mid-latitude variables (4.69) transform exactly to their equatorial counterparts, (4.71), except for the upper-layer mass equation, which does not appear in either the mid-latitude model nor the $\psi = O(1)$ equatorial model. Thus, the leading-order $\psi = O(1)$ equatorial model (4.72) is derived.

In the case where the solution to the leading-order vorticity equation was $\psi = O(s)$, the ψ and η fields are each re-scaled to be an order of magnitude smaller. Thus, note that the mid-latitude scaling with the re-scalings

$$f = O(s), \quad r = O(s), \quad \psi = O(s), \quad \eta = O(s^2), \quad h = O(s), \quad \text{and} \quad h_B = O(s),$$

yields exactly the full equations of the equatorial model. (4.71), but with ψ and η an order smaller, and thus the leading-order $\psi = O(s)$ equatorial model is recovered, again with the exception of the upper-layer mass equation.

From this point of view, the mid-latitude scaling with $\eta = O(1)$ yields the mid-latitude model, or the “outer” equations, and the mid-latitude scaling with $\eta = O(s^2)$ yields the lower-layer-forced equatorial scaling model, or the “inner” equations, while the mid-latitude scaling with $\eta = O(s)$, which may be thought of as an “intermediate” set of equations, produces the boundary-forced equatorial model.

Given this connection between the outer, inner and intermediate models, we may now identify in the mid-latitude derivation those terms that emerge in the leading-order equatorial model. By retaining those terms in the mid-latitude model, we will find a model that is, to leading order, uniformly valid. We retain exactly those higher-order terms that, although not leading-order terms at mid-latitudes, contribute to the leading-order balance in the equatorial (inner and intermediate) limit.

Therefore, we refer to the vorticity equation in the mid-latitude scaling that states all the terms, and we retain the leading-order terms plus the terms that contribute to the equatorial vorticity balance. The leading-order vorticity equation may therefore

be written

$$\Delta\psi_t + J(\psi, f/s + \mu\Delta\psi) + \nabla\chi \cdot \nabla f + f \{h_t + J(\psi, \mu h + h_B)\} = 0. \quad (4.74)$$

where ψ is the stream function for the rotational part of the velocity. This is the equation that expresses the dynamical evolution of the upper layer in this model. It remains true that the model of Swaters and Flierl (1991) is recovered in the case where $f \equiv 1$.

To derive the unified version of the divergence (or balance) equation, we refer to the complete divergence equation in the mid-latitude scaling and retain the leading-order terms plus the terms that contribute to the equatorial balance. Explicitly keeping the appropriate $O(s)$ and $O(s^2)$ terms in our balance equation.

$$\Delta\eta = \nabla \cdot [f\nabla\psi] + 2s\mu J(\psi_x, \psi_y) - s^2\Delta\chi_t + sJ(f, \chi). \quad (4.75)$$

Our two-layer model is formed by coupling these equations with the lower layer equations, which are unapproximated as stated in the model. The complete model, which we will refer to as the meta-model, may be written

$$\Delta w_t + J(w, f/s + \mu\Delta\psi) + \nabla\chi \cdot \nabla f + f \{h_t + J(\psi, \mu h + h_B)\} = 0. \quad (4.76)$$

$$\Delta\eta = \nabla \cdot [f\nabla\psi] + 2s\mu J(w_x, w_y) - s^2\Delta\chi_t + sJ(f, \chi). \quad (4.77)$$

$$\Delta\chi = h_t. \quad (4.78)$$

$$h_t + \nabla \cdot (\mathbf{u}_2 h) = 0. \quad (4.79)$$

$$s(\mathbf{u}_{2t} + \mathbf{u}_2 \cdot \nabla\mathbf{u}_2) + f\hat{\mathbf{e}}_3 \times \mathbf{u}_2 = -\nabla(\mu(\eta + h) + h_B) - r\mathbf{u}_2 \quad (4.80)$$

The form of the divergence equation (4.77) is consistent with the family of balance models studied by Gent and McWilliams (1983). The balance when $s \rightarrow 0$, which is the balance found in the mid-latitude scaling model, is part of the Linear Balance Equations (LBE). The balance retaining the leading-order plus the $J(\psi_x, \psi_y)$ term, which is the balance found in the equatorial scaling with boundary forcing, corresponds to the Balance Equations (BE). Retaining the leading-order terms plus the $J(f, \chi)$ term produces the balance equation of the global Linear Balance Equations (gLBE), and retaining all the terms except $\Delta\chi_t$ yields the balance equation for the global Balance Equations (gBE).

All the forms of the balance equations neglect the $\Delta\chi_t$ term. This reduces the number of prognostic equations in the system, thereby filtering out an entire class of waves.

4.5.3 Adjustment of length, velocity and time scales

The meta-model as written is expressed in terms of variables which have been nondimensionalized using the mid-latitude scaling. To show explicitly that this model contains the equatorial scaling model within its dynamics, we re-scale the uniform model using the equatorial nondimensional scales. That is, we shall show that the meta-model, when expressed in equatorial variables, recovers the leading-order equatorial model, and therefore is a uniformly-valid model.

The length, time and velocity scales in the equatorial and mid-latitude scalings

Mid-latitude	Equatorial
$L = R_d$	$L = s^{1/2} R_d$
$U_1 = \mu s f_0 R_d$	$U_1 = \mu s^{1/2} f_0 R_d$
$U_2 = s f_0 R_d$	$U_2 = s^{1/2} f_0 R_d$
$T = L/U_2$	$T = L/U_2$

Table 4.1: Length, velocity and time scales in the mid-latitude and equatorial nondimensional scalings. $R_d = \sqrt{g'H}/f_0$ is the internal Rossby deformation radius of the upper layer. $f_0 = \beta_0 L$ in the equatorial scaling.

are summarized in Table (4.1). When the scales are written in terms of the internal Rossby deformation radius of the upper layer.

$$R_d = \frac{\sqrt{g'H}}{f_0}.$$

where f_0 stands for $\beta_0 L$ in the equatorial scalings, the scales only differ by powers of s . Thus, denoting equatorial variables (nondimensional variables having been scaled by the equatorial scalings) with a caret (e.g. \hat{x}), and the mid-latitude variables without a caret.

$$(x, y) = s^{1/2}(\hat{x}, \hat{y}), \quad \mathbf{u}_1 = s^{-1/2}\hat{\mathbf{u}}_1, \quad \mathbf{u}_2 = s^{-1/2}\hat{\mathbf{u}}_2, \quad t = s\hat{t}.$$

We must scale ψ and χ as well. The nondimensionalization of ψ and χ arises directly from their definition in the Helmholtz decomposition of u_1 (4.48).

$$\psi^* = LU_1\psi, \quad \chi^* = sLU_1\chi.$$

Therefore, ψ and χ actually scale exactly the same in both coordinates.

$$\psi = \hat{\psi}, \quad \chi = \hat{\chi}.$$

There is no need to express the variables h , h_B , η , and f , in terms of equatorial variables since their scales are set in the generic nondimensionalization, independent of U_1 , U_2 , L or T . Writing the meta-model equations (4.76)–(4.80) in terms of equatorial variables, they transform to

$$\hat{\Delta}\hat{\psi}_i + \hat{J}(\hat{\psi}, f + \mu\hat{\Delta}\hat{\psi}) + s\hat{\nabla}\hat{\chi} \cdot \hat{\nabla}f + sf \{h_i + \hat{J}(\hat{\psi}, \mu h + h_B)\} = 0. \quad (4.81)$$

$$\hat{\Delta}\eta = \hat{\nabla} \cdot [f\hat{\nabla}\hat{\psi}] + 2\mu\hat{J}(\hat{\psi}_x, \hat{\psi}_y) - s\hat{\Delta}\hat{\chi}_i + s\hat{J}(f, \hat{\chi}). \quad (4.82)$$

$$\hat{\Delta}\hat{\chi} = h_i. \quad (4.83)$$

$$h_i + \hat{\nabla} \cdot (\hat{\mathbf{u}}_2 h) = 0. \quad (4.84)$$

$$\hat{\mathbf{u}}_{2i} + \hat{\mathbf{u}}_2 \cdot \hat{\nabla}\hat{\mathbf{u}}_2 + f\hat{\mathbf{e}}_3 \times \hat{\mathbf{u}}_2 = -\hat{\nabla}(\mu(\eta + h) + h_B) - r\hat{\mathbf{u}}_2. \quad (4.85)$$

At leading order, this reduces to the boundary-forced equatorial model. Therefore, the meta-model contains within it the dynamics described by that model.

It remains to investigate whether or not the lower-layer-forced equatorial model is contained within the meta-model. In that model, the w and η fields are a factor of s smaller than in the boundary-forced equatorial model. That is,

$$\hat{\psi} = s\tilde{w}, \quad \eta = s\tilde{\eta},$$

which, upon substituting into the set of equations (4.81)–(4.85), transforms them into the form

$$\hat{\Delta}\tilde{w}_i + \hat{J}(\tilde{w}, f + s\mu\hat{\Delta}\tilde{w}) + \hat{\nabla}\hat{\chi} \cdot \hat{\nabla}f + f \{h_i + s\hat{J}(\tilde{w}, \mu h + h_B)\} = 0. \quad (4.86)$$

$$\hat{\Delta}\tilde{\eta} = \hat{\nabla} \cdot [f\hat{\nabla}\tilde{w}] + 2s\mu\hat{J}(\tilde{w}_x, \tilde{w}_y) - \hat{\Delta}\hat{\chi}_i + \hat{J}(f, \hat{\chi}). \quad (4.87)$$

$$\hat{\Delta} \hat{\chi} = h_i, \quad (4.88)$$

$$h_i + \hat{\nabla} \cdot (\hat{\mathbf{u}}_2 h) = 0. \quad (4.89)$$

$$\hat{\mathbf{u}}_{2i} + \hat{\mathbf{u}}_2 \cdot \hat{\nabla} \hat{\mathbf{u}}_2 + f \hat{\mathbf{e}}_3 \times \hat{\mathbf{u}}_2 = -\hat{\nabla} (s\mu(\eta + h) + h_B) - r \hat{\mathbf{u}}_2. \quad (4.90)$$

At leading order, this set of equations reduces to the lower-layer-forced equatorial model. This completes the proof that the meta-model is indeed a leading-order uniformly valid model.

We note that it remains for future research to investigate the uniformly-valid model numerically. Since this model contains within it two-layer shallow-water dynamics (with a linear upper layer), it contains faster scales of motion than the slow dynamics of Swaters and Flierl (1991). One numerical technique to dealing with these faster time scales in layered models is to separate the dynamics into barotropic and baroclinic modes, and advance these modes forward in time using different schemes. The barotropic mode requires shorter time steps or more sophisticated methods because of the faster waves it contains. Another difficulty is the fact that the $s^2 \Delta \chi_t$ term in the divergence equation is multiplied by a small parameter, suggesting that the evolution of $\Delta \chi$ itself may be rapid.

4.6 Summary

In this chapter, we have addressed the issue of two-layer equatorial models. In the generalized Nof analysis, we have demonstrated that, with two layers and friction,

an analytical expression may be derived for the steady propagation of an eddy on a constant slope in the context of the f -plane approximation.

We derived three preliminary models of equatorial flow, one from a mid-latitude nondimensionalization, and two from an equatorial nondimensionalization. These models have not previously been stated in the literature, and all models predict well-defined flow at the equator. The mid-latitude (ESF) model may be thought of as a direct extension of the Swaters and Flierl (1991) model to the case of varying Coriolis parameter f . The equatorial model with lower-layer forcing has linear shallow-water dynamics in the upper layer and nonlinear shallow-water dynamics in the lower layer, and so contains within it the equatorial waves reviewed in Chapter 2. Both equatorially-scaled models are only partially coupled in their dynamics.

A leading-order uniformly valid model was then derived that, when written using the appropriate nondimensionalization, simplified to the preliminary mid-latitude or equatorial model.

Chapter 5

Conclusions

5.1 Summary

One of the goals of this research was to investigate models of equatorial abyssal flows in order to learn about the dynamics of these flows. Our approach was to base the models on the shallow-water equations, either in their original form or with simplifications, and in one- or two-layer configurations. Thus, our first step was to establish the conditions under which the shallow-water model is appropriate for these flows.

Therefore, we performed an asymptotic expansion of the three-dimensional equations of motion on the surface of a sphere, under the assumptions of constant density and frictionless flow. We showed that for motion near the equator, the equations of motion reduce to the shallow-water equations without curvature terms or the hor-

horizontal component of the Coriolis effect as long as the length scales of motion are less than the Earth's radius and longer than $\sqrt{Hr_0}$, where H is the vertical scale of motion and r_0 is the Earth's radius.

We then summarized some known results about the shallow-water model, and reviewed equatorial wave theory. The two-layer model we derived later in the thesis was based on two-layer shallow-water theory where the layers were of unequal depth and the surface of the upper layer was constrained by a rigid-lid assumption. In anticipation of deriving such a model, we investigated equatorial wave theory in the context of those same assumptions. It was shown that the waves of barotropic free-surface equatorial wave theory arise in the form of baroclinic modes, with the frequency and wave number scaled using a wave speed $c = \sqrt{g'H_1H_2/(H_1 + H_2)}$, where g' is the reduced gravity and H_1, H_2 are the depths of the two layers. Superimposed on this baroclinic motion are nondivergent barotropic Rossby waves.

The frictional geostrophic model was then described and its predictions compared with that of reduced-gravity shallow-water theory. In the frictional geostrophic model, the momentum equations are replaced by geostrophic balance plus a Rayleigh damping term. Thus, ageostrophic effects are parameterized as a flow down the pressure gradient. The two models were compared in simulations of a localized mass of dense fluid moving over idealized bottom topography, and in simulations of the evolution of a dense current over realistic Atlantic Ocean bottom topography, where the fluid is constantly flowing into the domain from the south.

In numerical simulations over idealized topography, the frictional geostrophic model was observed to successfully capture the overall path of northward along-slope, downhill, and north-south splitting that is predicted by the shallow-water model. Quantitatively, the simple model even predicts the along-slope Nof (1983) speed well. However, the lack of fluid inertia causes the simple model to underestimate the height that the fluid will reach when flowing up the opposite side of the channel. It also causes a very symmetric north-south splitting of the fluid.

In simulations of the two models over realistic equatorial topography, the simple model again captured the qualitative path of the fluid quite well. However, as compared to the shallow-water model simulations, it predicted a smaller mass flux across the equator, owing to the lack of inertia and the inability to flow up and over key ridges along the path. The amount of fluid crossing the equator was seen to depend sensitively on the choice of damping parameter r , with higher r correlating with less cross-equatorial flow. The amount crossing the equator was also seen to depend strongly upon initial depth of the current that approaches the equator. This is consistent with the concept that in this model the fluid is constrained to have a downhill component only, and no uphill flow.

For realistic parameter regimes, the shallow-water model was seen to agree qualitatively with observations, including capturing the clockwise flow in the equatorial basin. For inflow currents at shallower depths, the shallow-water model was observed to predict a dramatically different flow regime, characterized by a counterclockwise

flow in the equatorial basin and high time variability. This is understood to be caused by the introduction of new pathways of the current.

In the time-dependent simulations over realistic topography, we observed large fluctuations in the mass transport across the equator, as calculated at the mooring locations of Hall *et al.* (1997). In fact, we saw time-dependence that seemed to be consistent with their observed time-dependence of AABW flow across the equator. Our simulations implied that the extreme time-dependence may partially be an artifact of the precise location of the data collection site. That is, the amount of AABW successfully crossing the equator may not exhibit the same magnitude of time variability as the amount of AABW crossing those particular mooring locations. Furthermore, our simulations implied that the large time variability observed may be the result of a much smaller time variability in the source current.

The shallow-water simulations over realistic topography seemed to imply that the flow is almost entirely determined by the location (horizontal position and depth) of the narrow constrictions of the flow located at shallow sills. This, in turn, implies that observational studies should be focussed on these sills, such as the one at the entrance to the equatorial basin (from the southeast) or the exit of the basin (to the northwest). The overall behaviour of the flow depends critically upon these key spots, and so current meters placed in these locations would reveal much about the actual flow of the current.

We introduced baroclinicity in the form of two dynamically active layers in Chap-

ter 4. First, we derived the propagation speed of a relatively dense mass of fluid with compact support (i.e. an eddy), under the assumptions that the propagation speed is steady in time, the bottom topography has a constant slope, and the f -plane approximation may be applied. Our contribution here was the inclusion of frictional effects in addition to the effects of a dynamic upper layer pressure. The result is a generalization of the Nof (1983) and the Swaters and Flierl (1991) results. Friction was shown to introduce a down-slope component to the flow. However, the effects of upper-layer pressure may, in principle, restore the possibility of up-slope motion in the model.

A two-layer model was then derived that, while predicting geostrophically balanced flow away from the equator, allows $O(1)$ variations in the Coriolis parameter f , and indeed, predicts well-defined flow at the equator. In this model, the lower layer reduces to either the inviscid, inertial shallow-water equations, or to the frictional geostrophic model investigated in Chapter 3. The upper layer uses a generalization to geostrophy similar to the Charney balance equations. This model was shown to simplify, in the f -plane limit, to the Swaters and Flierl (1991) model, which was demonstrated by Karsten and Swaters (1999) to be the appropriate geostrophically-balanced model when the lower layer is relatively thin and the bottom topography dynamically important. This model was therefore referred to as the Equatorial Swaters-Flierl (or ESF) model.

After considering models that arise from equatorial scalings, a meta-model was

presented that simplifies, at leading order, to the ESF model, and by rewriting into equatorial scalings, simplifies to the equatorial models. Thus, this meta-model is valid both at the mid-latitude limit and at the equatorial limit.

5.2 Future directions

We have left for future research the study of abyssal flows in the other ocean basins, extending the research to multi-layer models (or even continuously-stratified models), and applying the model derived here to global-scale flows.

It is also left for future work to derive a simple model for the lower layer that, while describing simple or “slow” dynamics, retains more realistic dynamics than the Rayleigh damped models employed here, if that is indeed possible. The work of Warn, Bokhove, Shepherd, and Vallis (1995) may be helpful in this regard.

Adding extra dynamical layers (or developing a continuously-stratified model, which would also add the possibility of including internal gravity wave dynamics) would be interesting from the point of view of investigating the interaction and the time variability of the transport of the Antarctic Bottom Water and the southward-flowing North Atlantic Deep Water through the equatorial channel. Hall *et al.* (1997) found that the currents each had a strong annual variation, and were not separated by much distance in the vertical direction. Dynamical coupling between these currents almost certainly affects their time evolution.

References

- Arakawa, A., and Hsu, Y.-J. G. 1990. Energy conserving and potential-*enstrophy* dissipating schemes for the shallow water equations. *Mon. Wea. Rev.*, **118**, 1960–1969.
- Arakawa, A., and Lamb, V. R. 1981. A potential *enstrophy*- and energy-conserving scheme for the shallow water equations. *Mon. Wea. Rev.*, **109**, 18–36.
- Borisov, S., and Nof, D. 1998. Deep, cross-equatorial eddies. *Geophys. Astrophys. Fluid Dyn.*, **87**, 273–310.
- Butkov, E. 1968. *Mathematical physics*. Reading, Massachusetts: Addison-Wesley.
- Cushman-Roisin, B. 1994. *Introduction to geophysical fluid dynamics*. New Jersey: Prentice Hall.
- de Verdière, A. C., and Schopp, R. 1994. Flows in a rotating spherical shell: The equatorial case. *J. Fluid Mech.*, **276**, 233–260.

- DeMadron, X. D., and Weatherly, G. 1994. Circulation, transport and bottom boundary layers of the deep currents in the Brazil Basin. *J. Mar. Res.*, **52**, 583-638.
- Edwards, C. A., and Pedlosky, J. 1998a. Dynamics of nonlinear cross-equatorial flow. Part I: Potential vorticity transformation. *J. Phys. Oceanogr.*, **28**, 2382-2406.
- Edwards, C. A., and Pedlosky, J. 1998b. Dynamics of nonlinear cross-equatorial flow. Part II: The tropically enhanced instability of the western boundary current. *J. Phys. Oceanogr.*, **28**, 2407-2417.
- Edwards, N. R., Willmott, A. J., and Killworth, P. D. 1998. On the role of topography and wind stress on the stability of the thermohaline circulation. *J. Phys. Oceanogr.*, **28**, 756-778.
- Friedrichs, M. A. M., and Hall, M. M. 1993. Deep circulation in the tropical North Atlantic. *J. Mar. Res.*, **51**, 697-736.
- Gent, P. R., and McWilliams, J. C. 1983. Consistent balanced models in bounded and periodic domains. *Dyn. Atmos. Oceans*, **7**, 67-93.
- Hall, M. M., McCartney, M., and Whitehead, J. A. 1997. Antarctic Bottom Water flux in the equatorial western Atlantic. *J. Phys. Oceanogr.*, **27**, 1903-1926.
- Hogg, N. G., Siedler, G., and Zenk, W. 1999. Circulation and variability in the southern boundary of the Brazil Basin. *J. Phys. Oceanogr.*, **29**, 145-157.

- Holton, J. R. 1992. *An introduction to dynamic meteorology* (3rd ed.). San Diego: Academic Press.
- Hsu, Y.-J. G., and Arakawa. A. 1990. Numerical modeling of the atmosphere with an isentropic vertical coordinate. *Mon. Wea. Rev.*, **118**, 1933–1959.
- Johnson, G. 1993. A deep inertial jet on a sloping bottom near the equator. *Deep-Sea Res.*, **40**, 1781–1792.
- Karsten. R. H., and Swaters. G. E. 1999. A unified asymptotic derivation of two-layer frontal geostrophic models including planetary sphericity and variable topography. *Phys. Fluids*, **11**, 2583–2597.
- Kawase. M., Rothstein. L. M., and Springer. S. R. 1992. Encounter of a Deep Western Boundary Current with the Equator: a numerical spin-up experiment. *J. Geophys. Res.*, **97**, 5447–5463.
- Kawase. M., and Straub. D. 1991. Spinup of source-driven circulation in an abyssal basin in the presence of bottom topography. *J. Phys. Oceanogr.*, **21**, 1501–1514.
- Ledwell. J. R., Montgomery. E. T., Polzin. K. L., St. Laurent. L. C., Schmitt. R. W., and Toole. J. M. 2000. Evidence for enhanced mixing over rough topography in the abyssal ocean. *Nature*, **403**, 179–182.

- Matsuno, T. 1966a. A finite difference scheme for time integrations of oscillatory equations with second order accuracy and sharp cut-off for high frequencies. *J. Meteor. Soc. Japan*, **44**, 85–88.
- Matsuno, T. 1966b. Quasi-geostrophic motions in the equatorial area. *J. Meteor. Soc. Japan*, **44**, 25–42.
- McCartney, M. S., and Curry, R. A. 1993. Transequatorial flow of Antarctic Bottom Water in the Western Atlantic Ocean: Abyssal geostrophy at the equator. *J. Phys. Oceanogr.*, **23**, 1264–1276.
- McPhaden, M. J., and Ripa, P. 1990. Wave-mean flow interactions in the equatorial ocean. *Ann. Rev. Fluid Mech.*, **22**, 167–205.
- Mercier, H., and Speer, K. G. 1998. Transport of bottom water in the Romanche Fracture Zone and the Chain Fracture Zone. *J. Phys. Oceanogr.*, **28**, 779–790.
- Neelin, J. D., Latif, M., and Jin, F.-F. 1994. Dynamics of coupled ocean-atmosphere models: The tropical problem. *Ann. Rev. Fl. Mech.*, **26**, 617–659.
- Nof, D. 1983. The translation of isolated cold eddies on a sloping bottom. *Deep-Sea Res.*, **30**, 171–182.
- Nof, D., and Borisov, S. 1998. Inter-hemispheric oceanic exchange. *Q. J. R. Meteorol. Soc.*, **124**, 2829–2866.

- Nof, D., and Olson, D. B. 1993. How do western abyssal currents cross the equator? *Deep-Sea Res.*, **40**, 235–255.
- Pedlosky, J. 1987. *Geophysical fluid dynamics* (2nd ed.). New York: Springer Verlag.
- Pedlosky, J. 1996. *Ocean circulation theory*. Berlin: Springer-Verlag.
- Ren, S., and Shepherd, T. G. 1997. Lateral boundary contributions to wave-activity invariants and nonlinear stability theorems for balanced dynamics. *J. Fluid Mech.*, **345**, 287–305.
- Rhein, M., Stramma, L., and Send, U. 1995. The Atlantic Deep Western Boundary Current: Water masses and transports near the equator. *J. Geophys. Res.*, **100**, 2441–2457.
- Rodwell, M. J., and Hoskins, B. J. 2001. Subtropical anticyclones and summer monsoons. *J. Climate*, **14**, 3192–3211.
- Samelson, R. M. 1998. Large-scale circulation with locally enhanced vertical mixing. *J. Phys. Oceanogr.*, **28**, 712–726.
- Samelson, R. M., and Vallis, G. K. 1997. A simple friction and diffusion scheme for planetary geostrophic basin models. *J. Phys. Oceanogr.*, **27**, 186–194.
- Sandoval, F. J., and Weatherly, G. L. 2001. Evolution of the deep western boundary current of Antarctic Bottom Water in the Brazil Basin. *J. Phys. Oceanogr.*, **31**, 1440–1460.

- Speer, K., and Zenk, W. 1993. The flow of bottom water into the Brazil Basin. *J. Phys. Oceanogr.*, **23**, 2667–2682.
- Stephens, J. C., and Marshall, D. P. 2000. Dynamical pathways of Antarctic Bottom Water in the Atlantic. *J. Phys. Oceanogr.*, **30**, 622–640.
- Sun, S., Bleck, R., and Chassignet, E. P. 1993. Layer outcropping in numerical models of stratified flows. *J. Phys. Oceanogr.*, **23**, 1877–1884.
- Swaters, G. E. 1991. On the baroclinic instability of cold-core coupled density fronts on a sloping continental shelf. *J. Fluid Mech.*, **224**, 361–382.
- Swaters, G. E. 1998. Numerical simulations of the baroclinic dynamics of density-driven coupled fronts and eddies on a sloping bottom. *J. Geophys. Res.*, **103**, 2945–2961.
- Swaters, G. E., and Flierl, G. R. 1991. Dynamics of ventilated coherent cold eddies on a sloping bottom. *J. Fluid Mech.*, **223**, 565–587.
- Trenberth, K. E., and Caron, J. M. 2001. Estimates of meridional atmosphere and ocean heat transports. *J. Climate*, **14**, 3433–3443.
- Warn, T., Bokhove, O., Shepherd, T. G., and Vallis, G. K. 1995. Rossby number expansions, slaving principles, and balance dynamics. *Q. J. R. Meteorol. Soc.*, **121**, 723–739.

Yavneh, I., and McWilliams, J. C. 1994. Breakdown of the slow manifold in the shallow-water equations. *Geophys. Astrophys. Fluid Dyn.*, **75**, 131–161.